



**NANOBIOENGINEERED PLATFORMS FOR PHOTOELECTROCHEMICAL
DETECTION OF C-REACTIVE PROTEIN**

Yeison Esteban Monsalve García

Master's thesis submitted for the degree of Master in Materials Engineering

Advisors

Jahir Orozco Holguín, PhD

Co-advisor

Andrés Felipe Cruz Pacheco, PhD

University of Antioquia
Faculty of Engineering
Master's Degree in Materials Engineering
Medellín, Antioquia, Colombia

2024

Citation	Yeison Monsalve, Andrés F Cruz-Pacheco, Jahir Orozco [1]
Reference	[1] Yeison Monsalve, Andrés F Cruz-Pacheco, Jahir Orozco, “Nanobioengineered platforms for photoelectrochemical detection of C-reactive protein”, Master’s thesis, Master’s degree in Materials Engineering, University of Antioquia, Medellin, Antioquia, Colombia, 2024.
Style IEEE (2020)	



Master in Materials Engineering

Max Planck Tandem Group in Nanobioengineering



Centro de Documentación de Ingeniería (CENDOI)

Repositorio Institucional: <http://bibliotecadigital.udea.edu.co>

Universidad de Antioquia - www.udea.edu.co

This work's content corresponds to the authors' right of expression and does not compromise the institutional thinking of the Universidad de Antioquia, nor does it release its responsibility before third parties. The authors assume responsibility for copyright and related rights.

Dedication

I dedicate this master's thesis to my family—my parents, Noe Monsalve and Cecilia García, and especially my sister, Geraldine Monsalve—whose unwavering support has been fundamental to my personal and professional growth. I am deeply grateful to Dr. Jahir Orozco Holguín and Dr.

Andrés Felipe Cruz Pacheco for their invaluable guidance and support in developing this research. This accomplishment stands as a testament to their mentorship and dedication and the strength and encouragement of those who believed in me every step of the way. My passion for scientific research, which has driven me throughout my career as a materials engineer, has also guided my decisions and helped me shape a path toward achieving my research goals.

TABLE OF CONTENT

Academic production	11
ABSTRACT	12
CHAPTER I: Introduction, statement of the problem, justification, and objectives	13
INTRODUCTION	13
PROBLEM STATEMENT	15
JUSTIFICATION	17
OBJECTIVES	19
CHAPTER II: Theoretical framework and state of the art	20
Adapted from: Monsalve, Y., Cruz-Pacheco, A.F. & Orozco, J. Red and near-infrared light-activated photoelectrochemical nanobiosensors for biomedical target detection. <i>Microchim Acta</i> 191, 535 (2024). https://doi.org/10.1007/s00604-024-06592-x	20
Abstract	20
1. Introduction	20
2. Technical characteristics of photoelectrochemical biosensors	23
2.1. Photoactive nanomaterials	24
2.2. Physicochemical considerations	25
2.3. Sources of signals and excitation	25
2.4. (Bio)sensing formats and signaling strategies	26
3. Classification of photoactive nanomaterials	27
3.1. Metals and metal oxides	29
3.2. Carbon nitrides	33
3.3. Quantum dots (QDs)	35
3.4. Transition metal chalcogenides (TMCs)	39
4. Red light and NIR excited PEC biosensors	43

5. Photoelectrochemical detection of C-reactive protein	49
6. Characterization of PEC biosensors.....	53
7. Concluding remarks and perspectives	55
CHAPTER III: Assembly, analytical characterization, and	59
performance of the PEC nano-immunosensor	59
Abstract	59
1. Introduction	59
2. Experimental section.....	62
2.1. Reagents and solutions	62
2.2. Equipment	63
2.3. Synthesis of 4-MBA-coated gold nanostars (AuNS@4-MBA).....	64
2.4. Nano-immunosensor architecture	64
2.5. Electrochemical measurements	65
2.6. Photoelectrochemical measurements	66
2.7. Specificity and selectivity studies.....	66
2.8. Human serum samples analysis.....	66
2.9. Statistical analysis	67
3. Results and discussions	67
4. Conclusions	82
5. Acknowledgments.....	82
CHAPTER IV: Conclusions and Perspectives	83
REFERENCES	86
ANNEX 1	119
SUPPLEMENTARY INFORMATION CHAPTER III	119

LIST OF TABLES

Table 1. <i>Classification of photoactive nanomaterials in UV- and visible-light-activated PEC biosensors.</i>	28
Table 2. <i>PEC biosensors activated by red light and NIR</i>	43
Table 3. <i>(Photo)electrochemical biosensors for C-reactive protein detection</i>	51
Table 4. <i>Characterization techniques of PEC biosensing interfaces</i>	55
Table S1. <i>Theoretical data of the crystalline properties in gold nanomaterials.</i>	119
Table S2. <i>Data from the electrochemical characterization of the SPCEs with pretreatment oxSPCE, AuNSs/oxSPCE, anti-CRP/AuNSs/oxSPCE, BSA/anti-CRP/AuNSs/oxSPCE, Nafion/BSA/anti-CRP/AuNSs/oxSPCE, and CRP/Nafion/BSA/anti-CRP/AuNSs/oxSPCE interfaces by CV and EIS (n = 5). Electroactive surface area at the different steps of the modification of the SPCE, calculated from the CV scans performed in 5 mM [Fe(CN)₆]^{4-/3-} equimolar redox probe in 1X PBS solution at a scan rate of 50 mV/s: anodic electroactive area (A_a), cathodic electroactive area (A_c), average electroactive area (A_e) and anodic and cathodic peak separation (ΔE_p). Data from EIS experiments: Charge-transfer resistance (R_{ct}), electrolytic solution resistance (R_s), the Warburg impedance (Z_w), constant phase element (CPE) with pre-exponential factor (P), and exponent (n).</i>	125
Table S3. <i>(Photo)electrochemical biosensors for the detection of CRP</i>	128
Table S4. <i>Dilution factor used to detect CRP in the samples on the immunosensor and CRP quantification by the conventional Luminex method.</i>	130

LIST OF FIGURES

- Figure 1.** Schematic representation of PEC assays utilizing miniaturized electrochemical cells, external excitation sources, and specific interactions in immunosensing, genosensing, enzymatic, and cytosensing assays. Charge generation and transduction occur at the electrode surface through photoactive nanomaterials promoted by the alignment of conduction (CB) and valence bands (VB) in materials with varying band gaps.24
- Figure 2.** A) Au/ZnO hybrid interface for PEC detection of GSSG, reproduced with permission from Ref. [115]. B) PEC genosensor system based on $d\text{TiO}_{2-x}\text{-AuNPs}$ interaction for tDNA detection, reproduced with permission from Ref. [117]. C) Fabrication of a PEC enzymatic sensor for elucidating the activity of AChE, reproduced with permission from Ref. [116].32
- Figure 3.** A) GCE/g- $\text{C}_3\text{N}_4/\text{Ag}/\text{AgI}$ assembly for the PEC detection of S^{2-} mean the Ag_2S formation, reproduced with permission from Ref. [153]. B) g- $\text{C}_3\text{N}_4/\alpha\text{-Fe}_2\text{O}_3/\text{ITO}$ heterojunction for the PEC detection of glucose, reproduced with permission from Ref. [155]. C) PEC aptasensor assembly based on $\text{CoO}/\text{Au}/\text{g-}\text{C}_3\text{N}_4$ heterojunction for the MC-LR detection, reproduced with permission from Ref. [121].35
- Figure 4.** A) $\text{WS}_2/\beta\text{-CD}@/\text{CdS}$ assembly for the PEC detection of miR-21, reproduced with permission from Ref [129]. B) PEC immunosensor based on $\text{ITO}/\text{CdS}/\text{g-}\text{C}_3\text{N}_4/\text{CuS}$ heterojunction for the PSA detection, reproduced with permission from Ref [125]. C) $\text{FTO}/\text{CdS}/\text{h-BN}/\text{AuNPs}$ heterojunction platform for the PEC detection of miRNA-141, reproduced with permission from Ref [128].39
- Figure 5.** A) PEC aptasensor based on $\text{ITO}/\text{NGH}/\text{MoS}_2$ for CAP detection, reproduced with permission from Ref. [167]. B) $\text{MoS}_2/\text{NGQDs}$ modified platform for PEC aptasensing of acetamiprid, reproduced with permission from Ref. [126]. C) PEC immnosensing assembly for insulin detection based on $\text{ITO}/\text{BiOBr}/\text{Ag}_2\text{S}$ heterojunction, reproduced with permission from Ref. [172]. D) $\text{WS}_2/\text{MoS}_2/\text{Fe}_3\text{O}_4/\beta\text{-TiO}_2$ platform for PEC detection of 5fC, reproduced with permission from Ref. [133].42
- Figure 6.** A) WS_2/AuNPs modified platform for PEC cytosensing of MCF-7, reproduced with permission from Ref [186]. B) PEC cytosensing of MCF-7 based on $\text{ITO}/\text{Ag}_2\text{S}/\text{Au}$ heterojunction, reproduced with permission from Ref. [187]. C) $\text{FTO}/\text{NaYF}_4:\text{Yb,Tm}@/\text{TiO}_2$ platform for PEC detection of CEA, reproduced with permission from Ref. [188]. D) PEC detection of variable

concentrations of AA based on GC/AuNS heterojunction, reproduced with permission from Ref. [189]......49

Figure 7. Schematic representation of the modification of SPCE with the Nafion/BSA/anti-CRP/AuNS/oxSPCE nanobiocomposite for CRP detection using photoelectrochemical techniques in a 1X phosphate buffered saline (PBS) solution containing AA as the electron donor in plasmonic-based detection.68

Figure 8. (a) PEC performance of the modified AuNS/oxSPCE electrode in a 1X PBS (pH 7.4) solution containing 0.01M AA as an electron donor. (b) Raman spectra of the modified AuNS/oxSPCE electrode. (c) Energy relation of the oxSPCE by the UV-vis spectrum and (d) AuNSs by UV-vis spectroscopy. (e) Band diagram at the oxSPCE-AuNSs interface with valence and conduction band energy levels for oxSPCE and AuNSs.74

Figure 9. (a) CV of the modified AuNSs/oxSPCE electrode in a 1X PBS (pH 7.4) solution containing 5 mM $[Fe(CN)_6]^{4-/3-}$ as the redox mediator at 0.05 V/s, and (b) EIS from 50000 to 0.05 Hz, at the formal potential of 0.125 V, and amplitude 0.01 V. (c) FE-SEM images of the oxSPCE, and (d) AuNSs/oxSPCE electrodes, respectively.76

Figure 10. (a) Step-by-step PEC response of the nano-immunosensor architecture in a 1X PBS (pH 7.4) solution containing 0.01 M AA as the electron donor. (b) Amperometric signals were acquired at 0 V from the label-free PEC nano-immunosensor at varying CRP concentrations. (c) Linear regression curve of Δ Charge against different CRP concentrations ($n = 3$). (d) Specificity and selectivity test of the nano-immunosensor with 400 pg/mL of interfering biomolecules without and with two concentrations of CRP (1: 400 and 2: 25 pg/mL). *Indicates significant differences with $p < 0.05$ for all interferences and the negative control. (e) Time stability study of the nano-immunosensor for detecting 400 pg/mL CRP. (f) Time-based PEC responses of the biosensor stability test over 10 on and off light cycles.79

Figure 11. (a) PEC response of the nano-immunosensor in a 1X PBS (pH 7.4) solution containing 0.01 M AA as the electron donor across various serum samples from patients with different levels of inflammation. (b) Comparison between the results obtained from the PEC nano-immunosensor and standard Human Luminex[®] Discovery Assay for CRP detection in serum samples from patients with different levels of inflammation. Error bars represent three times the standard deviation ($n = 3$).81

- Figure S1.** (a) Au-seeds, and (b) AuNSs TEM images. (c) DLS, (d) ELS, (e) UV-vis absorption, and (f) XRD pattern with a theoretical gold insert of Au-seeds and AuNSs, respectively. 119
- Figure S2.** HRTEM images of (a) Au-seeds and (b) one tip in the AuNSs where the d-spacing was measured. 120
- Figure S3.** (a) Electrochemical pretreatment of the SPCE surface in 0.1 M H₂SO₄ by CV at + 1.6 – 0.0 V and scan rate of 0.1 V/s. (b) Electrochemical deposition (ED) of synthesized AuNSs by CV at 0.0 to 1.0 V, a scan rate of 0.05 V/s, during 15 cycles. (c) Optimization of the AuNSs ED process based on the number of cycles and the charge achieved during the PEC process in a 1X PBS (pH 7.4) solution containing 0.01 M AA as an electron donor. 120
- Figure S4.** Optimization of AA concentration in AuNSs/oxSPCE nanocomposite in PEC process in a 1X PBS (pH 7.4) solution containing 0.01M AA as an electron donor. 121
- Figure S5.** PEC performance of each AuNSs/oxSPCE nanocomposite step over 15 repetitions of on/off light in a 1X PBS (pH 7.4) solution containing 0.01M AA. 121
- Figure S6.** (a) UV-vis-DRS and (b) Tauc plot of the oxSPCE electrochemical pretreated surface. 122
- Figure S7.** (a) UV-vis absorption spectrum of Au-seeds, several synthesis batches of AuNSs, and (b) the respective PEC performance of AuNSs/oxSPCE nanocomposites. 122
- Figure S8.** AFM of the (a-b, e-f, i-j) oxSPCE and (c-d, g-h, k-l) AuNSs/oxSPCE nanocomposite in (a-d) height, (e-h) phase, and (i-l) potential mode. 123
- Figure S9.** PEC behavior of the Nafion membrane in the (a) bare SPCE, the (b) bare oxSPCE surface, the (c) bare AuNSs/oxSPCE surface, and (d) the nano-immunosensor assembly. 124
- Figure S10.** (a) CV at 0.05 V/s, and (b) EIS from 50000 to 0.05 Hz, at the formal potential of 0.125 V, and amplitude 0.01 V of the nano-immunosensor assembly in a 1X PBS (pH 7.4) solution containing 5 mM [Fe(CN)₆]⁴⁻³⁻. A: AuNSs/oxSPCE, B: 50 μg/mL of anti-CRP, C: 1% BSA, D: 1 % Nafion, and E: 0.8 ng/mL CRP. 125
- Figure S11.** (a) Nafion/BSA/Anti-CRP/AuNSs/oxSPCE nanobiocomposite and (b) the detection of CRP (0.8 ng/mL) using EIS fitting in the EISpectrum analyzer software in a 1X PBS (pH 7.4) solution containing 5 mM K₃[Fe(CN)₆]/K₄[Fe(CN)₆]. 126
- Figure S12.** Cyclic voltammetry curves in a 1X PBS (pH 7.4) solution containing 5 mM K₃[Fe(CN)₆]/K₄[Fe(CN)₆] measured at different scan rates (0.025-0.250 V/s) and peak currents

vs square root of scan rates for bare (a) SPCE, (b) oxSPCE, (c) AuNSs/oxSPCE, and (d) Nafion/BSA/anti-CRP/AuNSs/oxSPCE nano-immunosensor. 128

Figure S13. *(a-b) The optimal concentration of anti-CRP antibodies on the AuNSs/oxSPCE interface with 0.8 ng/mL of CRP. (c-d) Comparison of the signal-time relationship across several interaction times on the AuNSs/oxSPCE incubated with 0.8 ng/mL of CRP. (e-f) Specific interaction time of the Nafion resin on the nano-immunosensor assembly. (g-h) Optimal nano-immunosensor and interaction time of 0.8 ng/mL of CRP on the nano-immunosensor for 30, 60, and 45 min. In graphs (a, c, e, and f), black is the nano-immunosensor, red is 0.8 ng/mL CRP, and in graphs (b, d, f, and h), n=3. 128*

Figure S14. *Detection reproducibility assay with ten different immunosensor assemblies. 129*

Figure S15. *Bland-Altman plot between the results obtained from the PEC nano-immunosensor and standard Human Luminex[®] Discovery Assay for CRP detection in serum samples from patients with different levels of inflammation. 130*

Academic production

Published articles

1. Yeison Monsalve, Andrés F. Cruz-Pacheco, Jahir Orozco, “Plasmonic graphene-gold nanostar heterojunction for red-light photoelectrochemical immunosensing of C-reactive protein,” *ACS Sensors*, 2025.
2. Y. Monsalve, A. F. Cruz, and P. Jahir, “Red and near-infrared light-activated photoelectrochemical nanobiosensors for biomedical target detection,” *Microchimica Acta*, 2024, doi: 10.1007/s00604-024-06592-x.

Other published articles

A. F. Cruz-Pacheco, Y. Monsalve, Y. Serrano-Rivero, J. Salazar-Uribe, E. Moreno, and J. Orozco, “Engineered synthetic nanobody-based biosensors for electrochemical detection of epidermal growth factor receptor,” *Chemical Engineering Journal*, vol. 465, no. March, 2023, doi: 10.1016/j.cej.2023.142941.

Research internships

Abel Tasman Talent Program (ATTP) Summer of Research 2024. Groningen, Netherlands.

Conferences participation

1. Primer encuentro académico científico de la Red Nacional de Investigación en cáncer 2023. Instituto Nacional de Cancerología. Poster presentation. Bogotá D.C, Colombia. August 03 to 04, 2023.
2. 13^{er} Congreso Iberoamericano de Sensores – Ibersensor 2024. Oral presentation. Buenos Aires, Argentina. October 21 to 24, 2024.
3. VI congreso Colombiano de Electroquímica. Oral presentation. Bogotá, november 20 to 22, 2024.
4. 31st International Student Congress Of (bio)Medical Sciences (ISCOMS) 2024. Participant. Groningen, the Netherlands. June 3 to 6, 2024.

ABSTRACT

Photoelectrochemical (PEC) biosensors are an emerging field of analytical devices designed to detect and quantify (bio)analytes in clinical samples. These biosensors utilize light and photoactive nanomaterials to generate charge carriers and promote redox reactions on the electrode surface, with changes in electric current or potential correlated with the concentration of the (bio)analyte. However, challenges in advancing PEC biosensors are the instability of biomolecules caused by exposure to high-energy ultraviolet radiation and high-background noise. These drawbacks have been addressed by integrating red-light-activated plasmonic photoactive nanomaterials, which minimize photodamage to biomolecules while reducing background noise in (bio)detection processes. Likewise, energy conversion and charge transfer in PEC detection methods have accelerated with photoactive materials' efficient heterojunction. Additionally, incorporating miniaturized electrodes into PEC systems leads to portable and compact devices, making them ideal for point-of-care and on-site diagnostics. Thus, this work is a red-light PEC platform based on disposable electrodes decorated with plasmonic graphene and gold nanostars (AuNSs) to amplify photocurrent signals in the immunosensing of C-reactive protein (CRP), a crucial biomarker for monitoring inflammation. Anti-CRP antibodies as molecular recognition elements were immobilized by soft bioconjugation strategies on the nanostructured interface. CRP was selectively detected using chronoamperometry under irradiation with a 765 nm wavelength source. The physicochemical, PEC, and morphological properties of the (bio)interface were characterized by PEC, spectroscopic, and microscopic analyses. The analytical and clinical applicability of the PEC nanobiosensor was demonstrated by detecting CRP in serum samples with different levels of inflammatory response. Overall, incorporating plasmonic nanomaterials into miniaturized devices demonstrated the robustness of the red-light PEC system for the sensitive and specific detection of (bio)analytes of biomedical interest, such as CRP. The PEC nanobiosensors are versatile tools for detecting a wide range of biomolecules and offer new low-cost and fast-readout analytical solutions in clinical diagnostics.

Keywords — (Photo)electrochemical detection, plasmonic nanomaterials, C-reactive protein, inflammation biomarker, analytical performance.

CHAPTER I: Introduction, statement of the problem, justification, and objectives

INTRODUCTION

Developing affordable and portable biosensors for point-of-care (POC) testing has gained significant attention in recent years due to the growing demand for rapid and reliable detection of disease biomarkers [1]. Among the various biosensor types, PEC biosensors have emerged as a promising solution for detecting and quantifying (bio)analytes, owing to their unique ability to combine photochemical and electrochemical processes. PEC biosensors utilize light-activated materials to generate electron-hole pairs, subsequently participating in redox reactions at the electrode surface [2]. The generated photocurrent or change in potential directly correlates with the concentration of the target analyte, enabling highly sensitive detection with minimal background noise. However, a key challenge limiting the widespread application of PEC biosensors is the photodamage to biomolecules caused by exposure to high-energy ultraviolet (UV) radiation. UV light can disrupt chemical bonds and ionize molecules, leading to the degradation of biological recognition elements, such as enzymes, antibodies, or nucleic acids, used in PEC platforms. To address this issue, recent advances have focused on integrating plasmonic nanomaterials—such as gold and silver nanoparticles—into PEC systems [3]. These materials can be excited by near-infrared (NIR) radiation, which has lower photon energy than UV light, thereby minimizing damage to sensitive biomolecules while enhancing the overall performance of the biosensor. The unique optical properties of plasmonic nanomaterials, which stem from the collective oscillation of surface electrons, allow them to amplify electromagnetic signals in the visible and NIR spectra. This enhancement has proven effective in improving charge transfer, energy conversion efficiency, and overall signal amplification in PEC detection. Incorporating plasmonic nanomaterials has revolutionized PEC biosensors, significantly improving sensitivity, stability, and reproducibility. These systems can operate with minimal photodamage to biomolecules by harnessing NIR radiation, ensuring prolonged stability and high analytical performance [4]. This approach is particularly relevant for clinical diagnostics, where reliable, rapid, and specific detection of biomarkers is critical. One such biomarker is CRP, a pentameric protein produced by the liver in response to inflammation, infection, injury, or tissue damage. CRP levels are widely used in clinical

practice as a reliable indicator of inflammatory processes, providing crucial insights into various health conditions, including infections and cardiovascular diseases [5].

This study introduced a novel PEC biosensor platform based on disposable electrodes functionalized with nanostructured plasmonic materials, specifically interfacial graphene and gold nanostars (AuNSs), for the sensitive and specific detection of CRP. AuNSs were chosen for their exceptional plasmonic properties, facilitating efficient light absorption and scattering and enhancing photocurrent generation. The AuNSs were deposited on electrogenerated graphene edge planes over graphitic carbon electrodes. Anti-CRP antibodies (Abs) as molecular recognition elements for CRP-specific detection were immobilized on AuNSs/graphene nanocomposites. These components were assembled using soft bioconjugation strategies, such as electrostatic interactions, to ensure specific and efficient binding of anti-CRP Ab. Selective CRP detection was achieved using chronoamperometry, which measures current changes in response to applied potential over time, offering high sensitivity and specificity. The proposed PEC platform was further characterized to assess its chemical, PEC, morphological, and structural properties, along with the analytical performance of the detection assay. Integrating plasmonic nanomaterials on miniaturized electrodes promoted the development of robust, versatile, and energy-efficient PEC biosensors capable of detecting various biomarkers. Ultimately, this research contributed to creating low-cost, point-of-care devices tailored for specific bioanalytical applications, enabling early disease detection, real-time monitoring, and improved patient care.

PROBLEM STATEMENT

Low-cost nanobiosensors for POC testing approaches are being developed as a current trend in disease biomarker detection [6]. Nanobiosensors are simple and affordable devices that incorporate specific bioreceptors coupled with nanomaterials to produce a rapid, sensitive, and easily interpretable signal, even for users with minimal training and no need for sophisticated equipment [7]. The conversion of highly specific biochemical interactions between bioreceptors and targets can be quantified through [8] electrochemical, optical, photochemical, and PEC transducer platforms, among others [9]. Among them, PEC biosensors stand out for combining the principles of photochemistry and electrochemistry to detect and quantify analytes with high sensitivity and a low background signal [10]. PEC biosensors typically consist of a biomolecule serving as a bioreceptor (e.g., enzymes, antibodies, peptides, glycoproteins, nucleic acids, etc) linked to a photoactive material, e.g., semiconductor nanoparticle-decorated electrode [11]. When the target molecule interacts with the bioreceptor on the electrode surface, a (bio)chemical reaction or a change in the photoactive material is induced that can be used to identify and quantify the target analyte. The sensor surface is irradiated with photons of a specific wavelength to generate electron-hole pairs in the photoactive material, inducing a photocurrent or voltage response whose magnitude is target concentration-dependent [12].

Plasmonic nanomaterials with high surface area are being incorporated into transducer platforms, improving the analytical performance of detection devices [13]. These nanomaterials can increase energy transfer processes and amplify transduction signals to achieve highly sensitive, stable, and reproducible devices [14]. The collective oscillations of free electrons on the surface of plasmonic nanoparticles lead to the absorption, scattering, and amplification of electromagnetic signals in the spectrum's visible and near-infrared (NIR) regions. This effect is particularly pronounced in noble metal nanoparticles such as gold and silver of various sizes and morphologies [15]. The advantage of NIR radiation in stimulating plasmonic nanoparticles in PEC biosensing is highly relevant in avoiding significant damage to biomolecules such as proteins [16]. NIR photons have lower energy levels than ultraviolet (UV) radiation, which can potentially disrupt chemical bonds and ionize molecules [17]. In this way, NIR-excited plasmonic PEC systems present the synergy needed to limit photodamage to biointerfaces and prolong the stability of sensor platforms without compromising the expected analytical performance [18].

CRP is a pentameric protein produced by the liver but found in blood plasma, whose circulating concentrations rise in response to inflammation, infection, injury, or tissue damage. Therefore, detecting CRP as an inflammation biomarker is paramount in clinical practice as a reliable indicator of abnormal issues in the immune system [19]. CRP levels between 1 and 3 mg/L can provide crucial insights into various medical conditions, including infections and cardiovascular disease. Given its responsiveness to inflammatory processes, CRP plays a pivotal role in the timely detection and monitoring of immune system-related abnormalities, making it an invaluable tool for healthcare professionals in diagnosing and managing various health conditions. Therefore, using plasmon nanomaterials-based PEC biosensors for detecting C-reactive protein could aid in the early detection and monitoring of diseases, treatment evaluation, and improvement of overall patient care, potentially reducing treatment costs and the need for extensive medical attention.

Hypothesis

Developing photoelectrochemical platforms that rely on nanostructured bio interfaces enhances the analytical performance of a C-reactive protein detection device.

JUSTIFICATION

In the coming years, PEC immunosensors are anticipated to evolve into highly versatile, specific, and sensitive devices capable of detecting a wide range of biomarkers. By integrating advanced photoactive materials, these innovative sensors aim to address the limitations of current diagnostic methodologies, such as low sensitivity, specificity, and scalability. A novel approach in this context has incorporated photoactive nanomaterials into PEC immunosensors for detecting CRP, a key biomarker of inflammation. This approach employs a monochromatic near-infrared (NIR) light source alongside amperometric techniques, offering significant potential for developing rapid, cost-effective, and user-friendly diagnostic devices [20]. Furthermore, photo-responsive nanostructured materials as signal enhancers align with emerging trends in engineering advanced, tailored sensing platforms with exceptional analytical performance. This work analytically validated the red-light PEC immunosensor with real clinical samples, demonstrating its utility for precise CRP quantification across varying inflammation levels. Such advancements underscore the critical role of nanobioengineered PEC immunosensors in facilitating early detection, personalized diagnosis, and continuous monitoring of infectious and inflammatory diseases through sensitive and accurate biomarker identification [21].

From a materials engineering perspective, this research contributed to the implementation of synthesis and characterization strategies for photoactive materials and the assembly of plasmonic PEC immunosensors. Additionally, this work fostered a new line of research within the research group, positioning the team as national pioneers in the field. The knowledge and skills acquired benefited both the student, who developed expertise in nanoengineering and PEC technologies, and the research group, which expanded its capabilities in biosensor development. Developing affordable, sensitive, and selective diagnostic systems for common diseases offers significant benefits to the scientific community and society by providing robust detection capabilities. In the long term, this research may have a profound impact on public health by establishing standardized and accessible detection methods that reduce the need for complex and expensive tests, which ultimately may reduce mortality rates associated with various diseases [22].

The technological advances achieved through this work may have important social implications. The dissemination of knowledge was promoted through multimedia and informational resources that explain disease detection and highlight the potential of PEC immunosensing as a cutting-edge

diagnostic tool. Furthermore, the publication of the results of this research, including a comprehensive review of red-light and NIR PEC biosensors, contributed significantly to the scientific community by summarizing the historical, current, and future landscape of PEC biosensors, their applications in disease diagnosis, and their potential for disease prevention.

OBJECTIVES

A. General objective

To develop a miniaturized device based on a nanostructured bio-heterojunction interface for the photoelectrochemical detection of C-reactive protein with superior analytical performance.

B. Specific objectives

- To design a methodologic route to produce anisotropic gold nanoparticles with modulated surface plasmon bands using the seed-assisted growth method.
- To develop a nanobioengineered platform based on anisotropic gold nanoparticles for PEC detection of CRP as an inflammation biomarker.
- To evaluate the analytical performance of the developed platform in terms of dynamic linear range, sensitivity, the limit of detection, specificity, selectivity, reproducibility, and stability.

CHAPTER II: Theoretical framework and state of the art

Adapted from: Monsalve, Y., Cruz-Pacheco, A.F. & Orozco, J. Red and near-infrared light-activated photoelectrochemical nanobiosensors for biomedical target detection. *Microchim Acta* 191, 535 (2024). <https://doi.org/10.1007/s00604-024-06592-x>

Abstract

PEC nanobiosensors integrate molecular (bio)recognition elements with semiconductor/plasmonic photoactive nanomaterials to produce measurable signals after light-induced reactions. Recent advancements in PEC nanobiosensors, using light-matter interactions, have significantly improved sensitivity, specificity, and signal-to-noise ratio in detecting (bio)analytes. Tunable nanomaterials activated by a wide spectral radiation window coupled to electrochemical transduction platforms have further improved detection by stabilizing and amplifying electrical signals. This chapter reviews PEC biosensors based on nanomaterials like metal oxides, carbon nitrides, quantum dots, and transition metal chalcogenides (TMCs), showing their superior optoelectronic properties and analytical performance for the detection of clinically relevant biomarkers. Furthermore, it highlights the innovative role of red light and NIR-activated PEC nanobiosensors in enhancing charge transfer processes, protecting them from biomolecule photodamage in vitro and in vivo applications. Overall, advances in PEC detection systems have the potential to revolutionize rapid and accurate measurements in clinical diagnostic applications. Their integration into miniaturized devices also supports the development of portable, easy-to-use diagnostic tools, facilitating point-of-care (POC) testing solutions and real-time monitoring.

Keywords - Photoelectrochemical nanobiosensor, photoactive nanomaterial, red light, near-infrared (NIR), analytical performance

1. Introduction

PEC nanobiosensors use nanoscale components and light-matter interaction to provide specific quantitative or semiquantitative analytical information about a (bio)analyte. They convert biological signals into electrical signals under the influence of light. PEC nanobiosensors consist of nanostructured components linked to a molecular recognition element or bioreceptor that

specifically binds to the analyte and a transducer that converts this interaction into a measurable electrical signal [6], [23]. Rather than referring to the nanometric size of the entire device, the term nanobiosensor herein refers to a system with at least one nanostructure within its components [24], whose enhanced properties from the nanoscale dimension give place to new, improved features and functionalities when assembled into biosensing devices [25]. PEC nanobiosensors utilize the interaction of light with photoactive materials to follow electrochemical reactions, benefiting from enhanced electron-hole separation and signal amplification [11]. They typically integrate molecular recognition elements and/or (bio)receptors (e.g., enzymes, antibodies, nanobodies, peptides, cellular receptors, nucleic acids, glycans, aptamers, among others) with photoactive nanomaterials (e.g., semiconductor and plasmonic materials) [7], [26], [27], [28]. Characterized by their high sensitivity and specificity, PEC nanobiosensors offer significant advantages such as signal amplification, minimal background noise, and reduced photodamage. These sensors feature tunable optical properties, photostability, durability, and amenability for surface functionalization. By leveraging PEC approaches, these biosensors provide rapid response times, versatility, and multifunctionality [29]. The current or voltage response under irradiation with light of different wavelengths in PEC biosensors changes when a recognition event occurs on the transducer surface or electrode [12]. It allows for highly specific and sensitive detection of various analytes, making PEC biosensors a promising tool for diverse applications in medical diagnostics [30]. Additionally, PEC nanobiosensors can be manufactured rapidly and cost-effectively for single-use devices, enabling efficient measurement collection using disposable electrodes, simplifying sensor handling, reducing contamination risks, and eliminating laborious cleaning or maintenance steps [31]. This combination of high sensitivity, miniaturization, and disposable amenability makes PEC biosensors well-suited for rapid, cost-effective, and user-friendly bioanalytical applications [32]. Incorporating high-surface-area photostimulable nanomaterials onto transducer platforms has further enhanced the performance of PEC sensing devices [13]. These nanomaterials can improve energy transfer processes, amplifying transduction signals to achieve highly sensitive, stable, and reproducible devices [14]. Plasmonic nanoparticles, such as noble metals like gold (Au) and silver (Ag), exhibit collective oscillations of free electrons on their surface. This phenomenon leads to the absorption, scattering, and amplification of electromagnetic signals in the visible and NIR regions of the spectrum [15]. Utilizing this spectral radiation range to stimulate plasmonic nanoparticles in PEC biosensing is advantageous, as it minimizes potential photodamage to

biomolecules compared to ultraviolet (UV) radiation [16], [17]. By harnessing these advancements, plasmon nanoparticle-based PEC biosensors offer improved stability and analytical performance without compromising biointerface integrity, thereby facilitating sensitive analyte detection [18]. In PEC detection, light is crucial in exciting the photoactive species, generating an electrical signal for transduction, and facilitating the detection process [33]. Separating the excitation source from the detection system endows this technique with potentially higher sensitivity. This heightened sensitivity is specifically due to the ability to automate the system's excitation source, allowing it to be turned on and off in a specific time window. This automation enables a precise response to the detection of the target analyte, effectively eliminating background noise from secondary reactions that do not correspond to the PEC detection event of the system [34], [35]. Moreover, the ease of miniaturizing PEC biosensing systems renders them more effective than conventional optical and electrochemical methods [36], [37]. This efficacy is due to the favorable photogenerated charge transfer reactions at the modified electrode surface [38]. When the analyte is present in the sample, the resultant specific recognition events can directly or indirectly induce alterations in the PEC signal, used to monitor the analyte levels [39], [40].

The selection of the photoactive material stands out as one of the most critical steps in determining the analytical performance of PEC devices. This choice is vital for enhancing charge conversion at the photoactive surfaces [23]. In recent years, semiconductor nanomaterials have emerged as the most utilized photoactive materials for PEC biosensing applications [41]. Various factors influence the performance of PEC devices, including changes in the photon conversion properties of typical semiconductor materials employed in transducer platforms. These factors encompass temperature fluctuations, external light exposure, electric and magnetic fields, and alterations in their electronic states of valence and conduction bands [42], [43], [44], [45]. Such changes result in a sensitive response and impart unique properties in photoelectricity, photoluminescence, electroluminescence, electrochemiluminescence, and thermoelectric phenomena [46], [47], [48], [49], [50]. Semiconductor nanostructures exhibit a robust absorption capacity and an inherent electronic band structure [51]. Innovations in semiconductor morphology, structure, or elemental composition can bolster charge transport, facilitating high photoelectric conversion efficiency [52], [53].

Even though plenty of reviews have already been reported in the literature [33], [54], [55], [56], there is still a knowledge gap intended to fill in this topic. This chapter reviews the crucial role of

PEC nanobiosensors in detecting a wide spectral range of bio-analytes, discussing their impact on analytical performance. It compares PEC detection approaches stimulated by the spectrum's red light and NIR regions and thoroughly outlines the technical characteristics of these PEC assays, including their physicochemical properties, signal sources, sensing formats, and signaling strategies. Additionally, it explores various photoactive nanomaterials currently employed in PEC applications, examining their compositional and structural properties to enhance biosensing methodologies for various bio-analyte detection scenarios. Finally, it showcases the potential of red light and NIR region sources to improve PEC performance and finalizes with concluding remarks and perspectives to exploit PEC-based devices' transduction mode better.

2. Technical characteristics of photoelectrochemical biosensors

PEC explores the interaction between light and photoactive materials, resulting in the interconversion of photoelectric and chemical energy [57]. The physical interaction between the photoactive material and the electrode promotes the charge transfer generated by the photons absorbed from the material, producing electrons and holes. Sacrificial reagents or redox mediators in solution transfer electrons to the photogenerated holes to restrict charge recombination in the material. The charge transfer on the electrode is reflected in an increase in current or potential resulting from excitation with light [58]. PEC biosensors integrate photoactive materials and molecular biorecognition elements (bioreceptors) coupled to the electrode interface to detect various (bio)analytes [59]. The change of the PEC signal when the electrode is exposed to defined spectral ranges of light irradiation evidences the biorecognition event between the bioreceptor and the target (bio)analyte.

Conventional photodetection systems encompass four key components, as illustrated in *Figure 1*. First is the excitation source (light source), followed by the signal transduction platform, which consists of the electrode, photoactive material, and molecular recognition elements. The third component is related to the redox mediator dissolved in an electrolytic medium. Finally, the PEC signal-reading system [60]. Multiple interconnected physical and chemical processes are essential to generate the signal. Initially, photons are absorbed, initiating a charge separation process in the material. Subsequently, charges migrate and recombine at the interface between the photoactive material on the working electrode and the redox mediator [61].

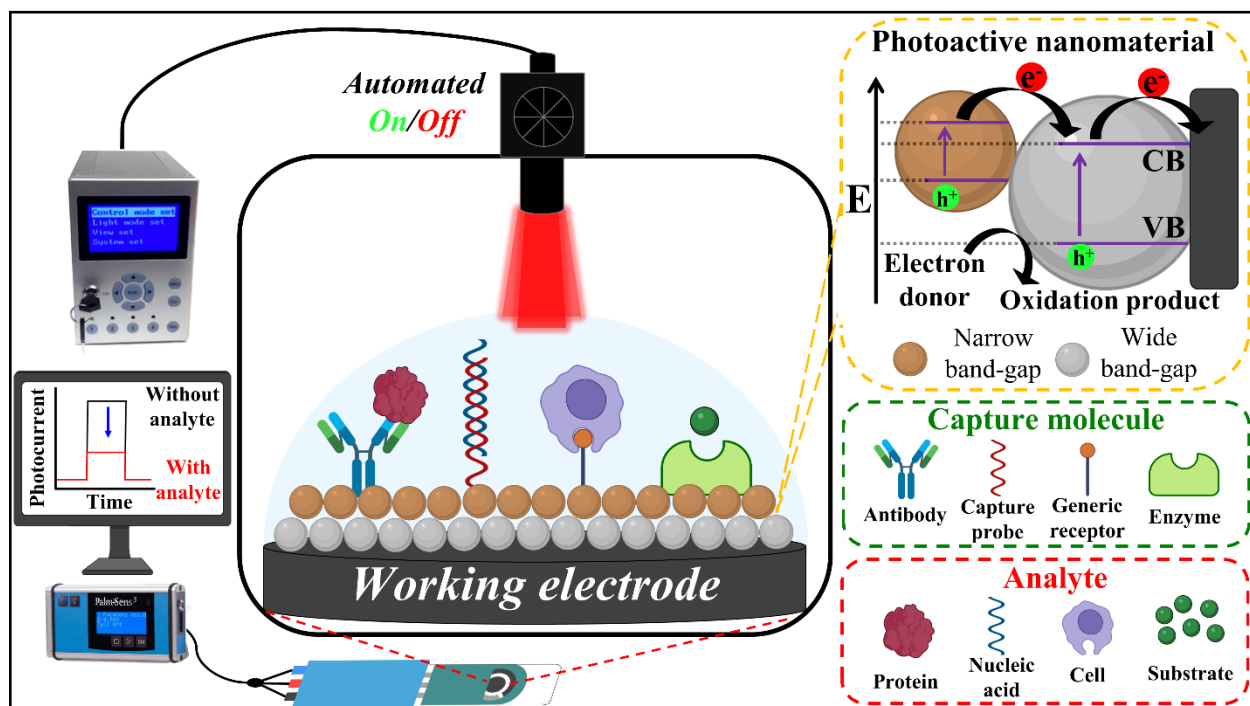


Figure 1. Schematic representation of PEC assays utilizing miniaturized electrochemical cells, external excitation sources, and specific interactions in immunosensing, gensensing, enzymatic, and cytosensing assays. Charge generation and transduction occur at the electrode surface through photoactive nanomaterials promoted by the alignment of conduction (CB) and valence bands (VB) in materials with varying band gaps.

Efficiently converting photons into electric charge is a crucial factor in PEC processes [62], [63]. PEC devices integrate light as an excitation source to generate an increased electrical signal, improving sensitivity compared to conventional electrochemical processes [64], [65].

2.1. Photoactive nanomaterials

A photoactive nanomaterial can generate chemical or physical changes when interacting with electromagnetic radiation, usually in detection systems in the ultraviolet-visible (UV-Vis) and NIR regions [66], [67]. The functionality of a photoactive material involves the absorption of light energy, the generation of electron-hole pairs, and a specific response that depends on its structural properties and the surrounding medium [68]. Integrating nanostructured materials into PEC biosensors offers advantages, including increased surface area, improved PEC features, bioconjugation, enhanced analytical properties, and the potential for miniaturization and amenability for portable sensing devices [69]. The light-sensitive nanostructured material interacts closely with the electrode and facilitates the transduction of the biochemical interaction into a

quantifiable electrochemical signal [70]. The choice of a photoactive nanomaterial depends on the requirements of the PEC sensing application, encompassing the target analyte, detection sensitivity, and operating conditions [71]. Consequently, research on new photoactive materials reinforces the versatility and functionality of PEC detection in bioanalytic applications [72], [73].

2.2. Physicochemical considerations

Specific physicochemical parameters play a pivotal role in comprehending the performance of photoactive nanomaterials [74]. To effectively absorb electromagnetic radiation and generate charge carriers leading to PEC detection, these materials must initially possess optical properties, including energy absorption and emission, as well as high quantum yield and extinction coefficient [75]. The morphology, atomic configurations and nanostructure's exposed surface area are related to the efficient transfer of charge carriers during reactions in electrolytic media [76].

Achieving proficient charge transfer and efficient electron flow within a PEC system hinges on the alignment of energy levels between photoactive nanomaterials and other components [77]. This alignment is crucial for effective charge injection, transport, and collection at the electrode. Equally important is selecting the appropriate excitation wavelength range and the energy level at which the nanomaterial is stimulated [78]. The range of wavelengths that photoactive nanomaterials absorb depends on their band gap [79]. The feasibility of designing and manipulating this band gap in PEC applications is demonstrated through doping, alloying, or quantum confinement effects. These methods allow absorption spectra adjustment and maximization of nanomaterial photoactivity [80].

2.3. Sources of signals and excitation

The photocurrent signals produced by PEC biosensors involve various kinetic and thermodynamic steps [81]. The performance of PEC biosensors is influenced by light excitation, photogenerated carrier transfer, and redox mechanisms [82], [83]. According to energy band theory, electrons are propelled from the valence band (VB) to the conduction band (CB) when photons with energy equal to or exceeding the band gap energy (E_g) of the photoactive nanomaterial irradiate them [84]. These photogenerated carriers are then transported to the electrode or electrolyte, but their effective utilization requires their migration to the surface from within the material [85]. Upon the creation of the electron-hole pair, a fraction of carriers promptly recombines, while others do so during their

journey to the surface (as illustrated in *Figure 1*). Carrier migration, a relatively slow process, introduces varying recombination pathways. Upon reaching the surface, carriers might engage in redox reactions with electroactive species in the electrolyte [86]. Nonetheless, many carriers recombine on the surface before completing these processes due to the time-consuming nature of electroactive species adsorption and medium-related redox reactions. The migration of carriers and the rates of reactions in photoactive materials are influenced by the VB/CB levels and the redox potential of electroactive species [87]. From a thermodynamic standpoint, oxidation/reduction reactions occur when the oxidizing species potential is more positive than the CB level, and the reducing species potential is more negative than the VB level [88].

2.4. (Bio)sensing formats and signaling strategies

Developing novel photoactive nanomaterials and searching for more sensitive, precise, and accurate signals in building PEC biosensing assays has proven challenging [89]. Highly specific and selective detection formats have achieved tests with minimal background noise compared to conventional methodologies [41]. The specificity and selectivity of the bioreceptor and the stable coupling with photoactive nanomaterials are paramount factors for direct detection of the molecular target [90], [91]. Consequently, PEC analysis's versatility and practical potential have found widespread applications in many scientific domains, particularly in identifying various (bio)analytes of biochemical and clinical interest [92]. These applications encompass nucleic acid analysis [56], immunoassays [93], [94], cell detection [95], [96], [97], enzyme and protein bio-detection [98], [99], [100], and monitoring of small (bio)molecules [101], [102].

Nevertheless, PEC detection poses a significant challenge in achieving the sensitive detection of various (bio)analytes, particularly those present at exceedingly low concentrations, such as biomolecules during the early stages of diseases. These concentration levels typically range from femtomolar (fM) to attomolar (aM), highlighting the critical need for highly sensitive methodologies to enable early and accurate disease diagnosis. This reality places heightened demands on PEC sensors' sensitivity and detection range [103]. Therefore, numerous signal amplification strategies have been introduced to enhance the practical utility of the devices. High analytical performance, self-powered functionality, and miniaturization significantly impact the overall effectiveness of PEC detection systems [104]. Likewise, detecting multiple analytes and analyzing big data are other progressive needs that require customization of detection systems

[105]. Consequently, the research on PEC biosensors has a noteworthy influence on endeavors to innovate and elevate the functionality of these devices [106], [107].

3. Classification of photoactive nanomaterials

Over the last decade, nanomaterials capable of interacting with electromagnetic radiation in the UV-visible and NIR ranges have been successfully coupled into PEC applications, generating photocurrent and photopotential signals [108], [109]. *Table 1* overviews the critical characteristics of various materials used in PEC detection processes. PEC systems generally require a redox probe to reveal the generated photocurrent and complete the charge transport cycles. Most semiconductor systems used in PEC systems have well-defined band gap values to determine the optimal excitation energy ranges. While band theory elucidates the general PEC principle, most PEC assays involve different optical and electrical phenomena depending on the nanomaterial and photoactive nanomaterials arranged on the transduction surface. In this context, molecular biorecognition events involve different PEC detection mechanisms. This chapter classifies PEC systems according to the photoactive nanomaterial type, including metals and metal oxides, carbon nitrides, quantum dots, semiconductors, and transition metal chalcogenides (TMCs).

Metallic nanostructures are highly valued in PEC systems for their surface plasmon resonance properties, which enhance light-particle interactions and improve photoelectric conversion efficiency [110]. However, their high cost and potential toxicity are significant drawbacks. In contrast, metal oxides are known for their strong light absorption, adjustable energy band gap, and exceptional chemical stability, making them suitable for harsh environments and effective at increasing photocurrent signals, although they may suffer from charge carrier recombination losses [111]. On the other hand, carbon nitrides (g-C₃N₄) offer high chemical stability and ease of functionalization due to their 2D structure and carbon-nitrogen conjugated bonds, but their relatively low conductivity can be a limitation [112]. Conversely, semiconductor quantum dots are appreciated for their quantum confinement effects, which enable size-tunable optoelectronic properties and efficient charge transfer [113]. However, they can encounter stability and toxicity issues. Finally, TMCs exhibit diverse optoelectronic properties and can function as metals and semiconductors, depending on their structure and conditions. They offer significant potential but face challenges with defect control and complex material synthesis [114].

Each type of nanomaterial has unique advantages and drawbacks, influencing its suitability for specific PEC applications. The properties of each photoactive nanomaterials play a crucial role, individually or as composite nanomaterials, in the assembly of biosensor platforms. These platforms leverage the unique virtues of each nanomaterial to enhance the detection device's analytical properties. The selection of the spectral range of radiation in the PEC process depends on the wavelength at which each photoactive material in the platform absorbs the radiation and uses it in the PEC detection process. The following section briefly reports the mechanisms explored for each family of materials.

Table 1. Classification of photoactive nanomaterials in UV- and visible-light-activated PEC biosensors.

PEC Materials	Platform structure	Electrolyte / Redox probe	λ_{exc} (nm)	Band gap (eV)	Detected biomarker	Linear range	LOD	Ref.
<i>Metals and metal oxides</i>	Au@ZnO/FTO nanorods	GSH/GSSG – PBS	1 sun	-	GSH	20-1000 μ M	3.29 μ M	[115]
	ZnONRs /TNs/TiO	(NH ₄) ₂ SO ₄	≥ 420	2.89	AChE	0.05-1000 μ M	0.023 μ M	[116]
	dTiO _{2-x} @Au	Exo III / PBS	585	2.52	DNA	1 pM – 10 nM	0.6 pM	[117]
	Au/GR-CdS	Na ₂ SO ₄	Xe Lamp	-	Diclofenac	1-150 nM	0.78 nM	[118]
	PdO/APFO-3: PCMB	NaHCO ₃ - PBS	1 sun	-	Oxygen	0.5 mg/L – 20 mg/L	0.034 mh/L	[119]
<i>Carbon nitrides</i>	g-C ₃ N ₄ /Co ₃ O ₄	Na ₂ HPO ₄ / NaH ₂ PO ₄	Xe Lamp	2.62 / 2.13	Oxytetracycline	0.01 – 500 nM	3.5 pM	[120]
	g-C ₃ N ₄ /AuNPs /CoO	Na ₂ SO ₄ / PBS	> 420	2.75 / 2.85	Microcystin - LR	0.1 pM – 10 nM	0.01 pM	[121]
	g-C ₃ N ₄ /BiVO ₄	PBS	> 420	2.70 / 2.40	Microcystin - LR	5 pg/L – 10 μ g/L	41.9 fg/L	[122]
	g-CNS3	AA / PBS	Xe Lamp	2.59	ALV-J	10 ^{2.14} -10 ^{3.35} TCID ₅₀ /mL	10 ^{2.08} TCID ₅₀ /mL	[123]
	g-C ₃ N ₄ /TiO ₂	AAP/PBS	> 460	2.69 / 3.21	Protein kinase A	0.05 – 100 U/mL	0.048 U/mL	[124]
g-C ₃ N ₄ /CdS QDs	AA/PBS	Xe Lamp	2.42	Prostatic antigen	0.01 – 50 ng/mL	4 pg/mL	[125]	

<i>Quantum dots</i>	g-C ₃ N ₄ /CdS QDs	AA/NaCl-KCl	Xe Lamp	2.42	MicroRNA-21	0.1 fM – 1 nM	0.05 fM	[126]
	rGO/CdS QDs	H ₂ O ₂ /PBS	> 450	-	2,3',5,5' Tetrachlorobiphenyl	10-1000 ng/mL	1 ng/mL	[127]
	h-BN/CdS QDs	AA / PBS	Xe Lamp	-	MicroRNA-141	0.001-100 nM	0.73 fM	[128]
	WS ₂ /β-CD@CdS nanorod	AA / PBS	1 sun	1.46/2.36	MicroRNA-21	0.1 fM – 10 pM	25.1 aM	[129]
<i>Transition metal chalcogenides</i>	Single-layer NanoMoS ₂	PBS	White LED	-	Dopamine	10 pM – 10 μM	2.3 pM	[130]
	SnS ₂ @Ti ₃ C ₂	Tris-HCl	Xe Lamp	1.86	5cadCTP	0.001 – 200 nM	260 fM	[131]
	MoS ₂ /NGQDs	PBS	Xe Lamp	-	Acetamiprid	0.05pM – 1nM	16.7 fM	[132]
	WS ₂ /MoS ₂ / β-TiO ₂	AA/PBS	> 420	1.37/1.57/2.38	5-Formylcytosine	0.01–200 nM	2.7 pM	[133]
	CdS/SnS ₂ /CNTs/GCE	PBS	Xe Lamp	2.12/1.92	Hydroquinone	0.2-100 μM	0.1 μM	[134]

5cadCTP: 5-carboxy-2'-deoxycytidine-5'-triphosphate, AA: ascorbic acid, AChE: acetylcholinesterase, Ag₂S: silver sulfide, AgI: silver iodide, ALV-J: J avian leukosis virus, APFO-3: ammonium pentadecafluorooctanoate, Au@ZnO/FTO: heteroconjunction of gold nanoparticles, zinc oxide and fluorine-doped tin oxide, Au/GR-CdS: heteroconjunction of gold nanoparticles, reduced graphene and cadmium sulfide, AuNPs: gold nanoparticles, BiOBr: bismuth oxybromide, BiVO₄: bismuth vanadate, BN: boron nitride, CdS QDs: cadmium sulfide quantum dots, CdS/SnS₂/CNTs/GCE: heteroconjunction of cadmium sulfide, tin disulfide, carbon nanotubes and glassy carbon electrode, CN: carbon nitride, CoO: cobalt(II) oxide, DNA: deoxyribonucleic acid, dTiO_{2-x}@Au: titanium dioxide and gold nanoparticles composite, Exo III: exonuclease III enzyme, [Fe(CN)₆]^{3-/4-}: hexacyanoferrate, GSH: glutathione, GSSG: oxidized glutathione, g-C₃N₄: graphitic carbon nitride, g-C₃N₄/Co₃O₄: heteroconjunction of graphitic carbon nitride and cobalt(II) oxide, g-CNS3: three-step thermal polycondensation of 2D g-C₃N₄ nanolayers, ITO: indium tin oxide, KCl: potassium chloride, LOD: limit of detection, MgCl₂: magnesium chloride, MCF-7: breast cancer cell line, MoS₂: molybdenum disulfide, Na₂SO₄: sodium sulfate, NaHCO₃: sodium hydrogen carbonate, (NH₄)₂SO₄: ammonium sulphate, NGQDs: nitrogen-doped graphene quantum dots, PBS: phosphate-buffered saline, PCMB: 4-chloromercuribenzoic acid, PdO: palladium oxide, RNA: ribonucleic acid, rGO: reduced graphene oxide, S: sulfur, SnS₂: tin(IV) sulfide, SnS₂@Ti₃C₂: heteroconjunction of tin (IV) sulfide and titanium carbide MXene, WS₂: tungsten disulfide, Xe: xenon, ZnONRs/TNs/TiO: heteroconjunction of zinc oxide nanorods and titanium dioxide, λ_{exc}: excitation wavelength.

3.1. Metals and metal oxides

The use of metallic nanostructures, such as those based on Au, Ag, and platinum (Pt), has been prompted in PEC systems due to their surface plasmon resonance properties [135]. Plasmons entail the collective oscillations of electrons on the surface of metallic nanoparticles. Electrons are excited when light interacts with these nanoparticles, generating plasmonic oscillations that produce a distinctive light-particle interaction [136]. This interaction leads to surface plasmon resonance, wherein light gets absorbed and scattered at wavelengths [137]. Plasmonic metal nanostructures can interact with light at frequencies aligned with the coherent oscillation of conduction electrons on the nanostructure's surface, thus generating resonant surface plasmons [138], [139], [140]. Excitation with wide energy ranges favors the injection of hot electrons into the conduction bands

of semiconductor materials through metal resonant plasmon energy transfer. The versatile optoelectronic attributes of plasmonic nanoparticles (narrow band gap) enable photoelectric conversion efficiency through intimate interaction with wide band gap semiconductors [141], [142].

Metal oxides constitute a class of nanomaterials with semiconducting characteristics ideal for applications in PEC devices. Metal oxides present strong light absorption, modifiable charge carriers (electrons and holes), and extensive surface area available for electrocatalytic reactions [143], [144]. Metal oxides have broad and tunable energy band gaps, which allow them to absorb radiation in a wide range of wavelengths, a fundamental characteristic for generating electrons and holes upon material illumination [145]. Likewise, metal oxides have exceptional chemical stability and are suitable for operating in corrosive or hostile environments, such as PEC cells [146], [147]. Many metal-oxide nanomaterials have catalytic properties, accelerating electrochemical reactions and increasing photocurrent signals [148].

Zhang et al [115] conducted a glutathione detection assay utilizing a "photo-anode" founded on zinc oxide (ZnO) nanorods decorated with Au nanoparticles. This plasmonic nanoparticle/semiconductor hybrid was employed as a comparative and competitive test to elucidate the role of metallic nanoparticles as charge transducers induced by the injection of hot electrons into the ZnO conduction band. Investigating the pathways of PEC signaling was based on water oxidation, the reaction's self-sustaining capability, and the detection of various glutathione concentrations. *Figure 2A* illustrates the detection mechanism of the Au/ZnO hybrid interface, where the surface plasmon resonance (SPR) of the Au nanoparticles enhances the absorption of visible plasmon-induced irradiation, generating energetic hot electrons. These electrons are then transferred to the conduction band of the metallic oxide material, facilitating charge transfer at the working electrode and enhancing charge carrier separation. Leveraging the surface sensitization provided by Au nanoparticles enables the creation of a glutathione disulfide (GSSG) detection assay with a linear range of 20-1000 μM , $R^2 = 0.996$, and a LOD of 3.29 μM across the entire spectral window, encompassing both visible and ultraviolet ranges.

Conversely, the utilization of titanium oxide (TiO_2) [29], [149] and its anatase phase ($\beta\text{-TiO}_2$) [117] (*Figure 2B*) has been explored for detecting specially designed DNA sequences within photoelectrode arrays. The plasmonic effect of an AuNP/tDNA nanobioconjugate on dTiO_{2-x} was employed for PEC detection of DNA. Likewise, exonuclease III (Exo III)-assisted target recycling

amplification was coupled to the detection system to amplify the number of rDNA segments labeled with AuNPs. The capture probe targeted DNA sequences related to the manganese superoxide dismutase gene (MnSOD gene), a regulator of cellular redox homeostasis. AuNP-tagged hairpin DNA probes were designed to recognize target DNA (tDNA) and undergo hybridization, activating Exo III and leading to the digestion of the probes into residual DNA (rDNA) segments containing AuNPs. These segments were then anchored to the electrode surface, facilitating DNA analysis. When plasmonic nanoparticles and TiO₂ converged within approximately 10 nm or less, a direct influence on the lifespan of charge carriers was observed. The generated hot electrons with a higher negative potential than that of the CB of dTiO_{2-x} could be injected smoothly into the CB, resulting in the enhancement of photocurrent. Moreover, the impact of the crystalline phase of TiO₂ was demonstrated with an LOD of 0.6 pM, a linear range between 1 pM and 10 nM, and a high linearity ($R^2 = 0.967$). This effect was rooted in the interplay between the nanomaterial structure of PEC processes and surface plasmons' resonance, together with the injection of hot electrons into the semiconductor's conduction band [150].

Zhang et al. [116] utilized a label-free PEC biosensing method to study acetylcholinesterase (AChE) activity using a nanocomposite made of zinc oxide nanorods (ZnONRs) within titanium dioxide nanotubes (TNs) on titanium foils (*Figure 2C*). The PEC nanocomposite was created by anodic oxidation of Ti foil to form TNs, followed by cathodic deposition of ZnONRs. AChE immobilized on this nanocomposite showed enhanced PEC responses under visible light. They observed that high concentrations of Cd²⁺ inhibited AChE activity, while low levels stimulated it. The PEC assay produced electron holes under light irradiation, which reacted with acetylthiocholine (ATCh) to generate thiocholine (TCh). It increased the photocurrent proportionally to the TCh concentration, reflecting AChE activity. The assay demonstrated high linearity in the 0.05-1000 μM range with a LOD of 0.023 μM. This method aided in understanding how metal ions affect enzyme activity and the pathogenesis of neurodegenerative disorders.

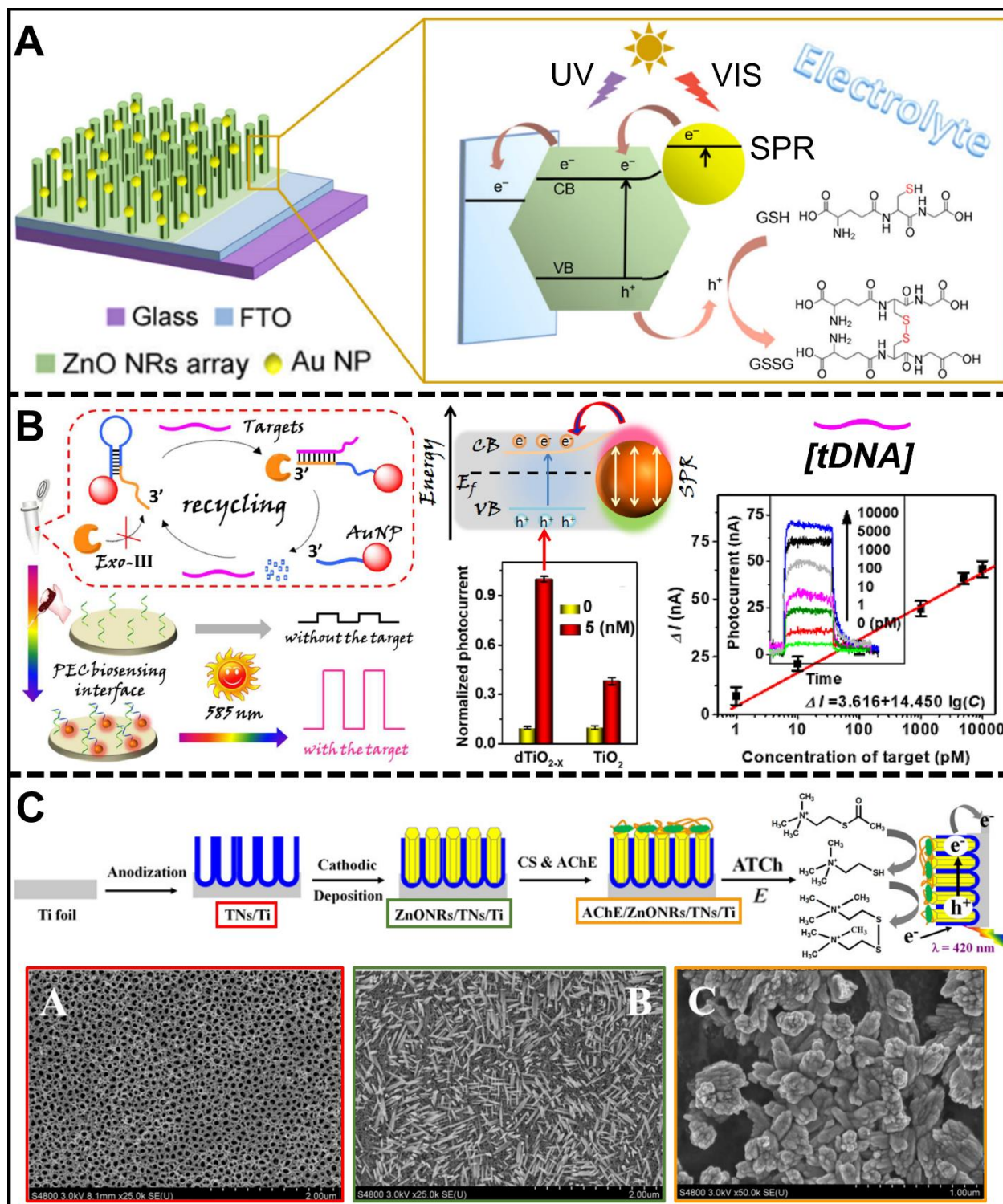


Figure 2. A) Au/ZnO hybrid interface for PEC detection of GSSG, reproduced with permission from Ref. [115]. B) PEC genosensor system based on $d\text{TiO}_{2-x}$ -AuNPs interaction for tDNA detection, reproduced with permission from Ref. [117]. C) Fabrication of a PEC enzymatic sensor for elucidating the activity of AChE, reproduced with permission from Ref. [116].

3.2. Carbon nitrides

Carbon nitrides are two-dimensional (2D) nanostructures, often called g-C₃N₄, bearing a graphitic-like framework constituted by carbon and nitrogen atoms intricately assembled within a singular crystal lattice [151]. Their layered, planar configuration facilitates the establishment of carbon-nitrogen conjugated bonds, fostering the generation of a continuous network of delocalized electrons traversing the 2D structure and conferring semiconductor attributes [152]. This distinctive feature was harnessed by Zeng et al. [153], who devised a photoelectrode based on graphitic carbon nitride, silver, and silver iodide (g-C₃N₄/Ag/AgI) heterojunction, as illustrated in *Figure 3A*. The integration of 2D g-C₃N₄ nanostructure with Ag as a plasmonic metal facilitated the design of a highly selective detection assay for hydrogen sulfide (H₂S). The interaction of band gap values, ranging between 2.7 eV (g-C₃N₄) and 2.8 eV (Ag/AgI), along with the strategic alignment of AgNPs, catalyzed electron transfer across metal/metal iodide and carbon nitride domains. The distribution of the three components on the platform formed a Z-scheme type system that reduced the recombination of photogenerated electron-hole pairs. The gradually increasing photocurrent showed that the Z-scheme pathway efficiently promoted the photoelectric conversion efficiency of g-C₃N₄. In the presence of the S²⁻ target, the AgI was transformed to Ag₂S, leading to the broken Z-scheme electron migration pathway and, thus, the decreased photocurrent. The authors established that a 402 nm monochromatic radiation source was optimal for inducing the generation of hot electrons in plasmonic metals, their subsequent transfer to the 2D structure, and the acceleration of delocalized electrons. The optimal Z-scheme junction led to a highly effective PEC detection assay, exhibiting linearity between 5-100 μM (R² = 0.998) and a LOD of 1.67 μM. This phenomenon stemmed from the judicious selection of the excitation range, a facet substantiated by spectroscopic analyses performed on the photoelectrode [154].

The research of Xu et al [155] also exploited the characteristics of a g-C₃N₄ interface and α-Fe₂O₃ (*Figure 3B*). This strategic pairing engendered a heterojunction for rapid migration of photogenerated carriers, thereby increasing the overall efficiency. The electrons within α-Fe₂O₃ could be effectively roused towards the conduction band, leveraging the influence of a 390 nm monochromatic radiation source to incite a gap formation within the valence band. Subsequently, the energized electron underwent a process of resonance energy transfer to the nanostructure of g-C₃N₄. The delocalized electrons gained momentum within this domain, participating in redox reactions in the medium. This assay highlighted the electron acceptor attributes inherent to

graphitic carbon nitride structures, demonstrating high linearity ($R^2 = 0.993$) in the range of 0.1-11.5 mg/L and a LOD of 0.03 mg/L. Combining g-C₃N₄ with other semiconducting or metallic materials produced exceptional photoactive nanocomposites ideal for supporting PEC detection assays [156].

Tan et al. [121] developed an aptamer-based PEC sensor (aptasensor) and a heterojunction composed of cobalt oxide (CoO), AuNPs, and g-C₃N₄ to detect microcystin-leucine arginine (MC-LR). The PEC platform, shown in *Figure 3C*, enhanced the separation of photo-induced electron-hole pairs, and AuNPs significantly increased the visible light absorption through SPR. The heterojunction structure benefited from the large surface area of g-C₃N₄ and the tailored band gap between g-C₃N₄ and CoO. AuNPs at the CoO-g-C₃N₄ interface enhanced light absorption and acted as electron mediators, forming a Z-scheme-type system that reduced charge carrier recombination. When MC-LR was captured on the PEC aptasensor, holes accumulated on the CoO VB, oxidizing MC-LR and further hindering electron-hole recombination, resulting in increased photocurrent. Visible light irradiation generated electrons on the CoO CB that flow to AuNPs, recombining with holes from the g-C₃N₄ VB, enhancing electron-hole pair separation and suppressing recombination. The SPR effect of AuNPs also produced hot electrons, contributing to increased photocurrent for MC-LR quantification, with a linear range of 0.1 pM to 10 nM, an $R^2 = 0.997$, and a low LOD of 0.01 pM.

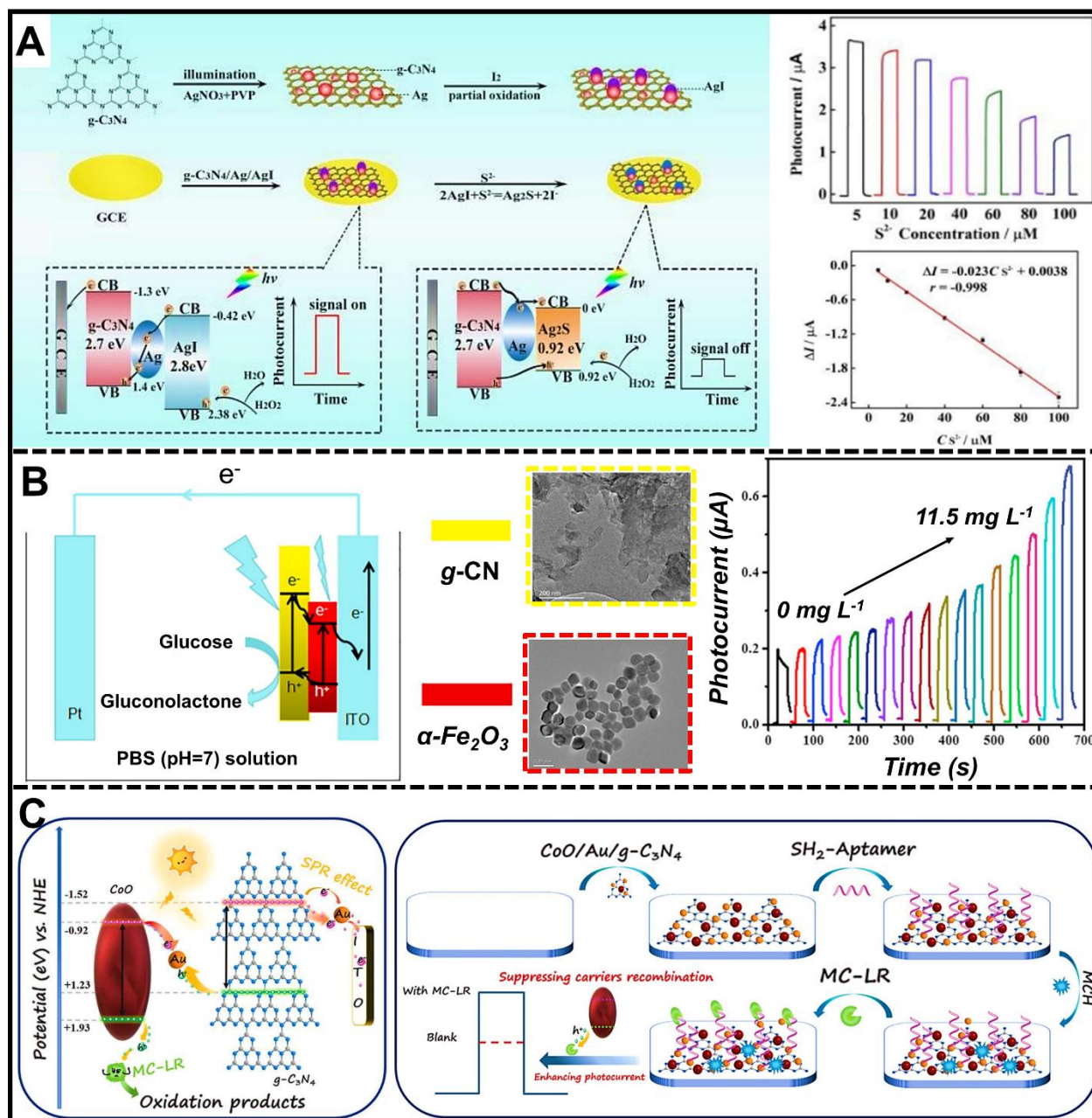


Figure 3. A) GCE/g-C₃N₄/Ag/AgI assembly for the PEC detection of S²⁻ mean the Ag₂S formation, reproduced with permission from Ref. [153]. B) g-C₃N₄/α-Fe₂O₃/ITO heterojunction for the PEC detection of glucose, reproduced with permission from Ref. [155]. C) PEC aptasensor assembly based on CoO/Au/g-C₃N₄ heterojunction for the MC-LR detection, reproduced with permission from Ref. [121].

3.3. Quantum dots (QDs)

Semiconductor QDs constitute a collection of nanoscale materials, typically encompassing 10²–10⁵ atoms, with dimensions not exceeding 10 nm [157], [158]. Their compactness engenders an

environment conducive to the quantum confinement of electrons and holes across all three spatial dimensions [159]. Consequently, QDs harbor a distinctive semiconductor property wherein the energies and wave functions of the constrained quantum states can be manipulated by adjusting the QDs' size, shape, and composition. This inherent confinement is pivotal for exceptionally efficient charge transfer [160], [161].

Xue et al. [129] demonstrated the PEC behavior of QDs using a photoelectrode composed of tungsten disulfide (WS_2), β -cyclodextrin (β -CD), and cadmium sulfide (CdS) heterostructure (*Figure 4A*). Incorporating CdS QDs increased the photocurrent due to their ability to generate holes and electrons, which were enhanced by quantum confinement effects and created a localized electric field for ascorbic acid (AA) oxidation. The experiment used a variable power radiation source covering the visible spectrum and specific ultraviolet frequencies, highlighting the narrow wavelength activation range of QDs. The nanostructured interface was utilized to construct an ultrasensitive PEC biosensor for detecting microRNA-21 (miR-21) using a cyclic strand displacement reaction (SDR)-mediated Cu^{2+} quenching mechanism. Adamantane (ADA)-labeled hairpin DNA1 (ADA-H1) was immobilized on the electrode via host-guest interaction with β -CD@CdS. When a mixture of target miR-21 and biotin-labeled hairpin DNA2 (Bio-H2) was added, ADA-H1 unfolded through hybridization. Bio-H2 then hybridized with ADA-H1, releasing miR-21 and triggering another SDR process. Avidin-labeled CuO nanoparticles attached to the duplex were dissolved, releasing Cu^{2+} , which reacted with CdS to form Cu_xS , reducing the photocurrent. This easy-to-assemble WS_2/β -CD@CdS heterojunction and the SDR-dependent Cu^{2+} quenching signal cascade enabled highly sensitive miR-21 detection, with a highly linear range of 0.1 fM to 10 pM ($R^2 = 0.997$) and a LOD of 25.1 aM.

In a similar vein, Liu et al. [125] developed a label-based PEC biosensing method for detecting prostate-specific antigen (PSA) using a CdS@g- C_3N_4 heterojunction and CuS-conjugated antibodies (Ab2-CuS) for signal amplification (*Figure 4B*). The PEC immunosensor was constructed by assembling CdS@g- C_3N_4 , chitosan (CS), AuNPs, and primary antibodies (Ab1) on dual electrodes, followed by blocking unbound sites with bovine serum albumin (BSA). Varying concentrations of PSA were added to one working electrode (WE1) and a fixed concentration to the other (WE2) before incubating Ab2-CuS on both. The specific binding of PSA to Ab2-CuS led to a weakened photocurrent response in a linear concentration range of 0.01-50 ng/mL and a LOD of 4 pg/mL. Spatial resolved radiometry was based on the photocurrent intensity ratio between

WE1 and WE2. With well-matched band energies, the photoactivity of the CdS core and g-C₃N₄ shell enabled effective light harvesting and electron-hole pair separation. Electrons migrated to the CdS CB while holes transferred to the g-C₃N₄ VB, enhancing photoactivity and stability. The Ab2-CuS conjugates acted as signal amplifiers by weakening the PEC intensity in the presence of PSA. This effect occurred due to photogenerated electrons transferring from g-C₃N₄ to CuS, reducing electron transfer to the electrode. The captured electrons formed O₂^{•-} with dissolved O₂, enabling ultrasensitive PSA detection through photocurrent generation.

QDs coupled to highly sensitive and label-free PEC biosensors were also studied by Yu et al. [128], as shown in *Figure 4C*. The PEC biosensor was based on CdS QDs sensitized porous hexagonal boron nitride (h-BN) nanosheets (NSs) and multiple-site tripodal DNA walkers (TDWs) formed through catalytic hairpin assembly (CHA). The porous h-BN NSs provided a large surface area and numerous active sites, making them ideal for photoelectric substrate materials. The h-BN/CdS QDs composite ensured the efficient transmission of photogenerated electrons and holes, resulting in high photoelectric conversion efficiency. CHA-formed TDWs triggered by miRNA-141 immobilized a significant amount of alkaline phosphatase (ALP) on the electrode surface, catalyzing ascorbic acid 2-phosphate (AAP) to produce AA as an electron donor. The h-BN/CdS QDs composite was coupled to a fluorine-doped tin oxide (FTO) electrode and modified with Hairpin4 (H4) DNA tracks. Upon miRNA-141 initiation, TDWs bound to H4 on the electrode surface and underwent strand displacement, exposing the toe region of H4. This region formed a double-stranded DNA structure with ALP-AuNPs-H5 through further strand displacement, continuing the walking process and anchoring more ALP on the electrode. Under visible light, h-BN NSs and CdS QDs photogenerated electrons and holes, moving electrons from the CB of h-BN to CdS QDs and then to the electrode, creating a stable photocurrent. It allowed for the sensitive detection of miRNA-141, achieving an excellent linear range from 1 fM to 100 nM ($R^2 = 0.997$) and a detection limit of 0.73 fM. This PEC biosensor provides a robust strategy for early clinical diagnosis and biomedical research.

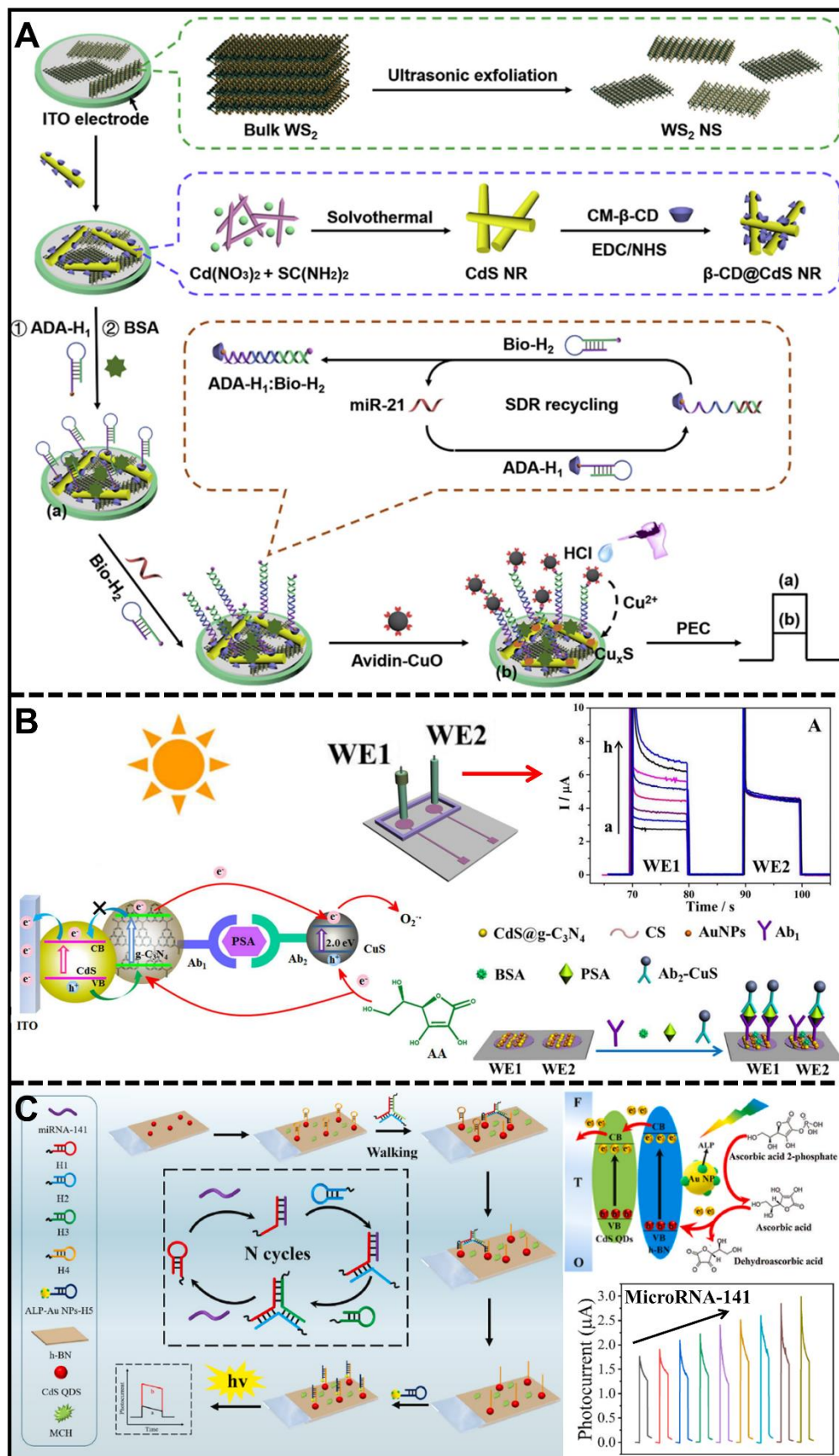


Figure 4. A) $WS_2/\beta\text{-CD}@CdS$ assembly for the PEC detection of miR-21, reproduced with permission from Ref [129]. B) PEC immunosensor based on ITO/CdS/g- C_3N_4 /CuS heterojunction for the PSA detection, reproduced with permission from Ref [125]. C) FTO/CdS/h-BN/AuNPs heterojunction platform for the PEC detection of miRNA-141, reproduced with permission from Ref [128].

3.4. Transition metal chalcogenides (TMCs)

TMC nanomaterials are composed of chalcogen atoms, commonly oxygen, sulfur, selenium, or tellurium, in conjunction with a transition metal [162], [163]. Extensive research has been conducted to explore the optoelectronic properties of TMCs, especially tungsten disulfide (WS_2) and MoS_2 . The molecular arrangement of TMCs involves positioning metal atoms surrounded by chalcogen atoms in an organized manner, forming 2D or 3D layers [164]. Due to the specific arrangement of atoms within the structure, they can exhibit conductive characteristics under certain conditions, such as nanometer-scale thinning or introducing defects [165], [166].

Wang et al. [167] and Dai et al. [132] reported improved performance of TMCs through the synergy of MoS_2 /N-graphene (*Figure 5A*) and MoS_2 /NGQDs (*Figure 5B*) nanostructures, respectively. Both studies utilized semiconductors to sensitize the TMCs and capture signals within narrow wavelength ranges of approximately 400 and 630 nm. Wang et al. employed MoS_2 /N-graphene (NGH) heterojunctions for PEC analysis of chloramphenicol (CAP) in food samples with the aid of a CAP aptamer. The MoS_2 /NGH composites displayed a reversed “V-shaped” p-n heterojunction curve, promoting efficient spatial charge separation and longer photocarrier lifetimes. The PEC sensor recognized CAP quickly, inhibiting electron-hole recombination and enhancing the photocurrent. The sensor showed excellent linearity from 32.3 ng/L to 96.9 $\mu\text{g/L}$ ($R^2 = 0.998$), with a detection limit of 3.23 ng/L. On the other hand, Dai et al. used nitrogen-doped graphene quantum dots (NGQDs) with ultrathin MoS_2 nanosheets ($NGQDs/MoS_2$) to create a high-performance photoactive material. The NGQDs extended the lifetimes of photogenerated charge carriers, leading to improved charge separation and substantial photocurrent signal amplification for acetamiprid detection. The photocurrent intensity decreased with increasing acetamiprid concentration, showing a linear range from 0.05 pM to 1 nM and a detection limit of 16.7 fM. These advancements highlight the benefits of TMCs in PEC detection, including chemical stability, efficient charge carrier separation, and transport, resulting in significantly improved detection performance.

One particular type of TMC is metal sulfides, a class of nanomaterials that manifest metallic and semiconductor properties ideal for electronic applications [168], [169]. The optoelectronic mechanism of these materials hinges on the role of metal cations as electron donors and sulfide anions as electron acceptors [170], resulting in a partially occupied VB and an unoccupied CB. This dynamic engenders a distinctive band gap contingent upon the structural attributes of the ionic arrangement within the crystal lattice [12], [171]. One clear example is given by Wei et al. [172]. They developed a highly sensitive insulin detection assay on bismuth oxybromide (BiOBr) and silver sulfide (Ag_2S) modified indium tin oxide (ITO) electrodes (*Figure 5C*). The photoelectrode was irradiated with 420 nm monochromatic light in a solution with AA as a redox probe and PBS as an electrolyte medium. The resonant energy levels of the BiOBr microspheres and Ag_2S nanoparticles enabled efficient electronic transition under visible light with high photocurrent signals compared to the individual systems. The photocurrent response in the PEC system decreased with a progressive increase in the insulin concentration on the electrode in a range between 0.001 ng/ml to 20 ng/ml, $R^2 = 0.993$, and a detection limit of 0.2 pg/ml. This method ensured measurement stability and robust PEC activity.

Likewise, ITO photoelectrodes were modified with a heterojunction of nanosheets of tungsten disulfide, molybdenum disulfide, and titanium dioxide ($\text{WS}_2/\text{MoS}_2/\beta\text{-TiO}_2$) to detect 5-formylcytosine (5fC), as shown in *Figure 5D* [133]. The nanostructured surface of TMCs was coated with $\text{Fe}_3\text{O}_4\text{-NH}_2$ covalently coupled to 4-amino-3-hydrazino-5-mercapto-1,2,4-triazole (AHMT) using a cross-linker of N-succinimidyl 4-(N-maleimidomethyl) cyclohexanecarboxylate (SMCC). The hydrazine of AHMT specifically captured 5fC by reaction with the aldehyde groups of the AHMT/ $\text{Fe}_3\text{O}_4/\text{WS}_2/\text{MoS}_2/\text{ITO}$ interface. AA was used as a redox probe for interference-free detection under white light. 2D metal sulfide-semiconductor heterojunctions demonstrated outstanding photoactive and analytical performance, with a linear range of 0.01-200 nM ($R^2 = 0.998$) and a LOD of 2.7 pM. It highlights the role of TMCs in PEC sensing applications, providing sensitive and time-stable responses.

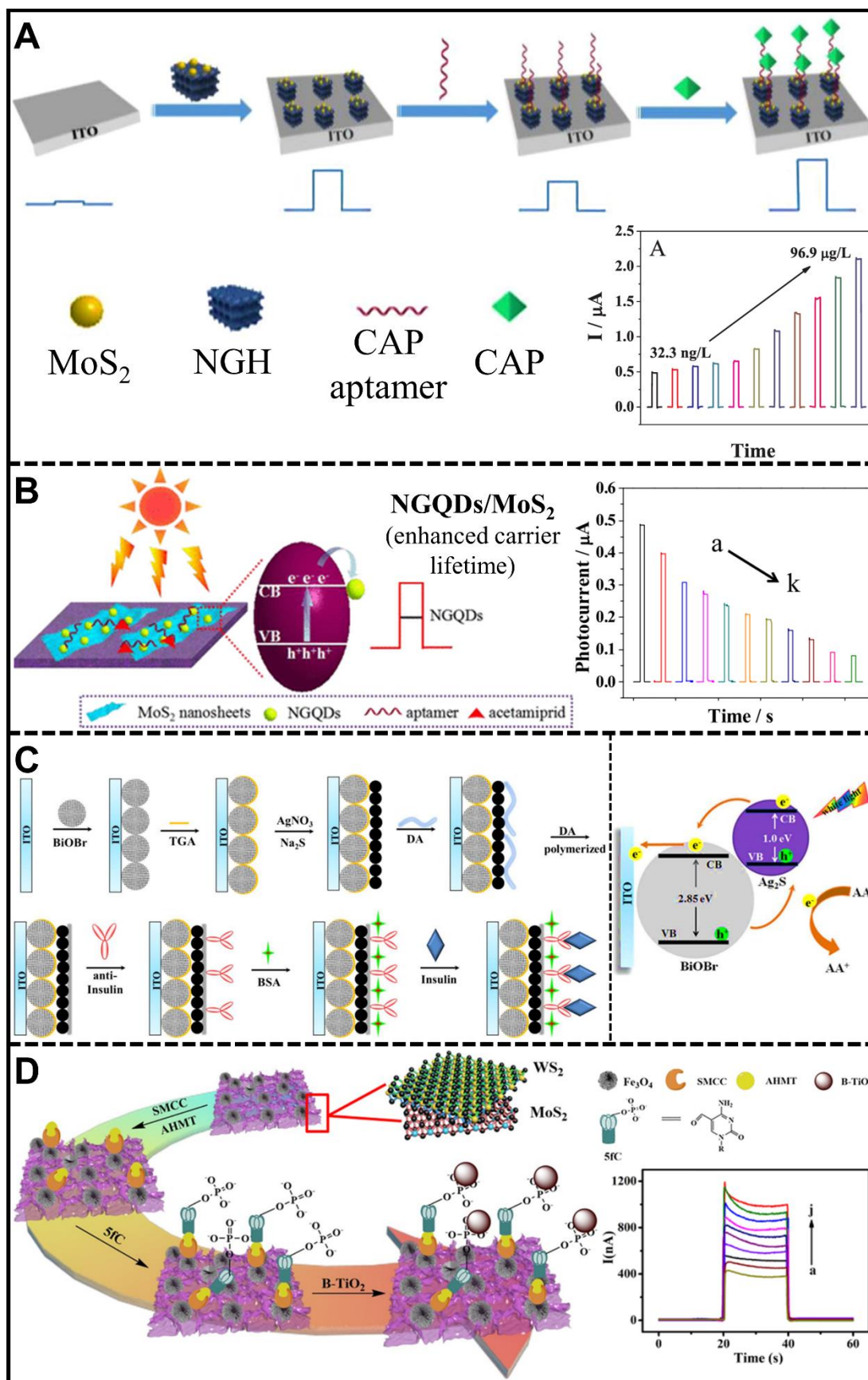


Figure 5. A) PEC aptasensor based on ITO/NGH/MoS₂ for CAP detection, reproduced with permission from Ref. [167]. B) MoS₂/NGQDs modified platform for PEC aptasensing of acetamiprid, reproduced with permission from Ref. [126]. C) PEC immnosensing assembly for insulin detection based on ITO/BiOBr/Ag₂S heterojunction, reproduced with permission from Ref. [172]. D) WS₂/MoS₂/Fe₃O₄/β-TiO₂ platform for PEC detection of 5fC, reproduced with permission from Ref. [133].

In the evolving field of PEC bioanalysis, significant progress has been made across various approaches and applications, each offering unique advantages and challenges. Zhao et al. [54] emphasized integrating PEC techniques with biomolecular detection, highlighting the development of bismuth-based photoelectrodes to address toxicity and low efficiency in conventional materials. This approach shows promise in enhancing PEC performance through improved charge separation and light absorption. On the other hand, Ai et al. [55] focused on applying electrochemical, electrochemiluminescent, and PEC techniques for detecting epigenetic modifications, underscoring the importance of these methods in diagnosing diseases and understanding biological functions. It emphasizes the need for ultra-sensitive and specific detection technologies in this context. Similarly, Chen et al. [56], [173] provided an extensive overview of PEC DNA biosensors, detailing the types of transducers and probe immobilization techniques used and various DNA interactions that can be monitored. Despite significant advancements, challenges such as stability and reproducibility remain, with future research directed to solve such issues, develop new photoactive materials, and integrate nanotechnology for clinical applications.

Liu et al. [174] explored the advancements in self-powered PEC sensors, which enhance portability and simplify operation by eliminating the need for external power sources. These sensors leverage solar energy to drive redox reactions, offering superior sensing performance and environmental benefits. In contrast, Pang et al [175] delved into semiconductor nanomaterial-based PEC biosensing, highlighting the role of materials such as metallic oxides, sulfides, and graphitic carbon nitride in constructing high-performance PEC sensors. It pointed out the challenges of improving photoconversion efficiency and addressing photobleaching. Finally, Tang et al [176] emphasized the impact of nanotechnology on PEC biosensing, focusing on advanced photoactive nanomaterials and their charge separation and transfer mechanisms. The biomedical applications of PEC biosensors and the potential of composite materials in overcoming limitations like high charge recombination rates and low photoelectric conversion efficiency. Overall, the promising future of PEC bioanalysis, driven by continuous innovations in material science and sensing mechanisms,

aims to enhance sensitivity, specificity, and practical applications in fields ranging from disease diagnosis to environmental monitoring.

4. Red light and NIR excited PEC biosensors

The evolution of diverse structural configurations integrating optical and electrochemical analyses sets the stage for the refinement of more accurate and efficient PEC assays to quantify a wide array of substances [177]. Within this framework, the adoption of red light and NIR excitation in PEC devices offset the limitations of existing sensors with UV light. Radiation in the UV range restricts the applications of PEC biosensors in areas of biodetection of clinically relevant biomarkers due to conformational damage and decreased biological activity of protein-type bioreceptors such as antibodies or enzymes [178], [179], [180]. NIR light, spanning wavelengths from over 650 up to 1700 nm, is gaining importance in biosensing and biomedicine due to its minimal spectral interference, ability to penetrate deep tissues, and limited harm to biological entities [181], [182]. Consequently, considerable efforts have been devoted to extending the excitation source into the visible spectrum by coupling small band gap semiconductors to augment light absorption efficiency and biosensor performance. Radiation in this range is less energetic, facilitating non-invasive or minimally invasive detection in biological samples such as blood or tissues [183], [184]. Red light and NIR PEC biosensors also exhibit reduced background interference (photobleaching), which improves signal quality, biosensor sensitivity, and probe stability over extended analysis periods [185]. *Table 2* reviews the most representative reports on nanobiosensors activated by red and NIR light.

Table 2. *PEC biosensors activated by red light and NIR*

Platform structure	Electrolyte / Redox probe	λ_{exc} (nm)	Detected biomarker	Linear range	LOD	Ref.
ITO/WS ₂ /AuNPs	PBS/AA	630	MCF-7 cell	10 ² - 5*10 ⁶ cells/mL	21 cells/mL	[186]
ITO/AgS ₂ /AuNPs	PBS/AA	810	MCF-7 cell	10 ² - 10 ⁷ cells/mL	100 cells/mL	[187]
FTO/NaYF ₄ :Yb,Tm@TiO ₂	G bases	980	CEA	0.01-40 pg/mL	3.6 pg/mL	[188]
GC/AuNSs	PBS	780	AA	0.1 - 11 mM	10 μ M	[189]
ITO/Bi ₂ O ₃ S/AuNPs	PBS/AA	808	MCF-7 cell	50 - 5 *10 ⁶ cells/mL	17 cells/mL	[190]
FTO/NaYF ₄ :Yb,Tm/ZnO/CdS	PBS/AA	980	AFP	0.01-200 ng/mL	5 pg/mL	[191]
FTO/CdS/NaYF ₄ :Yb,Tm@NaYF ₄	PBS	980	miRNA-21	0.05-100 nM	8 pM	[192]

FTO/Ag ₂ S/AuNP	PB	980	MC-LR	10 pg/L -10 μg/L	7 pg/L	[193]
ITO/AgInS ₂	Tris-HCl/AA- NaCl-KCl	630	CCRF-CEM cell	1.5*10 ² -3*10 ⁵ cells/mL	16 cells/mL	[194]
NaYF ₄ :Yb,Tm@ZnO	Na ₂ SO ₄	980	CEA	0.1-300 ng/mL	0.032 ng/mL	[195]
NaYF ₄ :Yb,Er/Ag ₂ S	Na ₂ SO ₄	980	CEA	0.005-5 ng/mL	1.9 pg/mL	[178]
TiO ₂ /AuNPs	PBS	760	TET	2-150 nM	0.6 nM	[196], [197]
ITO/CN/TsCuPc	PB/DA	>630	DA	0.05-50 μM	2 nM	[197]
FTO/ZnO/Ag/NaYF ₄ :Yb,Tm	PBS	980	AFP	0.05-100 ng/mL	0.04 ng/mL	[198]
NaYF ₄ :Yb,Er@CdTe	Na ₂ SO ₄	980	CEA	10 pg/mL - 5.0 ng mL	4.8 pg/mL	[199]
FTO/NaYF ₄ :Yb, Er@Au@CdS	Na ₂ SO ₄ / glucose-H ₂ O ₂	980	AFP	0.01-40 ng/mL	5.3 pg/mL	[200]

AFP: alpha-fetoprotein, AuNSs: gold nanostars, AA: ascorbic acid, AgInS₂: silver indium disulfide quantum dot, Ag₂S/AuNPs: heteroconjunction of silver sulfide quantum dot and gold nanoparticles, Bi₂O₃S/AuNPs: heteroconjunction of bismuth oxysulfide chalcogenide and gold nanoparticles, CEA: carcinoembryonic antigen, CN/TsCuPc: heteroconjunction of carbon nitride and copper phthalocyanine, DA: dopamine, FTO: fluorine-doped tin oxide, G: guanine, GC: glassy carbon, H₂O₂: hydrogen peroxide, ITO: indium tin oxide, KCl: potassium chloride, λ_{exc}: excitation wavelength, miRNA-21: microRNA 21, Na₂SO₄: sodium sulfate, NaCl: sodium chloride, NaYF₄, Er@CdTe: core-shell sodium yttrium tetrafluoride doped with ytterbium and erbium, coated with cadmium telluride upconversion nanoparticle, NaYF₄, Tm@TiO₂: core-shell sodium yttrium tetrafluoride doped with ytterbium and thulium, coated with titanium dioxide upconversion nanoparticle, NaYF₄, Tm/ZnO/CdS: heteroconjunction of sodium yttrium tetrafluoride doped with ytterbium and thulium upconversion nanoparticle, zinc oxide, and cadmium sulfide, PB: phosphate-buffered, PBS: phosphate-buffered saline, TET: tetracycline, Tris-HCl: Tris(hydroxymethyl)aminomethane hydrochloride, WS₂/AuNPs: heteroconjunction of tungsten disulfide and gold nanoparticles.

Red and NIR light have been explored to detect breast cancer cell lines (MCF-7) [186], [187]. Plasmonic nanoparticles were incorporated into ITO electrodes modified with multicomponent semiconductor nanomaterials to improve the photoelectric conversion efficiency. In the first study, TMC, WS₂, and AuNPs heterojunctions were assembled on ITO to detect MCF-7 cells non-invasively. A long excitation wavelength was employed in PEC bioanalysis to prevent cell damage or denaturation. WS₂ nanosheets exhibited low cytotoxicity and harvested red light to produce photoinduced electrons injected into the ITO electrode, with photogenerated holes and scavenged by AA. The AuNPs assembly on WS₂ nanosheets amplified the photocurrent by approximately 31 times due to the localized surface plasmon resonance (LSPR) effect of the AuNPs. The direct transfer of hot electrons from the plasmonic metal to the CB of the WS₂ nanosheet occurred by the induction of a collective oscillation of free electrons on the surface of the AuNPs under 630 nm irradiation (*Table 2*). A MUC1 aptamer immobilized to the nanostructured interface was used to capture MCF-7 cells as a model analyte specifically. Detection of MCF-7 cells was related to the decrease in photocurrent under irradiation with red light at a fixed voltage in amperometry at 0.1 V, showing a high linearity in a range of 10² - 5 × 10⁶ cells/mL (R² = 0.996), with a LOD 21 cells/mL. The efficiency of plasmon-enhanced photoelectric conversion highlighted the

effectiveness of PEC methods for sensitively detecting cancer-related biomarkers without collateral damage to the analyte biomolecules.

On the other hand, the ITO/Ag₂S/AuNPs heterojunction was used under 810 nm NIR light to quantify MCF-7 cells and dynamically evaluate cell surface glycan expression after sialidase (SA) stimulation, as shown in *Figure 6B* and *Table 2*. Ag₂S QDs showed excellent PEC properties in the NIR range, and adding AuNPs created a hybrid material with enhanced photoelectric conversion efficiency. AuNPs exhibited strong LSPR, leading to significant signal amplification. The biosensing platform featured a self-assembled monolayer (SAM) of thiol on the AuNPs, facilitating the assembly of 4-mercaptophenylboronic acid (MPBA) molecules. MPBA was a biorecognition element to capture MCF-7 cells through the reaction between SA on the cell membrane and boric acid in MPBA. This specific capture decreased photocurrent proportional to the MCF-7 concentration, with a linear range of 10² - 10⁷ cells/mL, an R² = 0.992, and a 10² cells/mL LOD. The LSPR effect enhanced the photoelectric conversion efficiency by increasing light scattering and promoting electron-hole pair generation in Ag₂S QDs. The platform effectively transferred plasmonic energy from AuNPs to Ag₂S QDs, improving light absorption and charge separation, which is crucial for sensitive MCF-7 detection.

The plasmon-enhanced direct electrocatalysis of gold nanostars (AuNSs) deposited on a glassy carbon (GC) substrate for PEC detection of AA is shown in *Figure 6D* [189]. The electrocatalytic performance of the AuNSs/GC system increased substantially under red light irradiation. This enhancement was attributed to the collective oscillations of conduction electrons in the light-excited AuNSs, also called LSPR. The study highlights the tunability of the LSPR of plasmonic nanostructures through parameters such as size, shape, interparticle distance, and surrounding medium properties. LSPR excitation drove electrons from the sharp tips (hot spots) of the AuNSs to higher energy levels, generating hot electrons. The anisotropic AuNSs hosted numerous “hot spots,” facilitating the efficient generation of hot carriers and a reduced activation energy barrier. Likewise, the photothermal effect of LSPR excitation further increased the electrocatalytic performance of the AuNSs. The measurement at open circuit potential (OCP) led the hot electrons to the external circuit, separating them from the holes and preventing recombination. The accumulation of hot holes on the surface of AuNSs enhanced the oxidation ability of AA, reducing the overpotential and activation energy for AA electrocatalysis in a linear range of 0.1 - 11 mM

with a LOD of 10 μM and a detection sensitivity of 190.9 $\mu\text{A}/\text{cm}^2\text{mM}$. The detailed description of plasmon-mediated electrocatalysis under NIR and red-light irradiation lays the foundation for the design of PEC (bio)sensors based on anisotropic plasmonic nanostructures.

Similarly, other studies have reported the use of the conjunction between AuNPs and TMC, QDs, carbon nitrides, or metallic oxides, activated with red or NIR radiation for the detection of various targets shown in *Table 2*: MCF-7 cells at 808 nm [190], MC-LR cells at 980 nm [193], CCRF-CEM cells at 630 nm [194], tetracycline at 760 nm [196], and dopamine at 630 nm [197]. These studies highlight the versatility of detection modalities achievable with different arrangements of photoactive nanomaterials using red and NIR radiation. Additionally, future research can focus on developing new NIR light-sensitive materials and miniaturized photoelectrodes, applying them further for in vivo and single-cell analysis due to the versatility of irradiating nanostructured surfaces based on these photoactive nanomaterial arrangements.

Lanthanide-doped up-conversion nanoparticles (UCNPs) represent another material-sensitive NIR radiation type. UCNPs convert low-energy excitation light into high-energy fluorescence emission, leveraging their exceptional chemical stability, resistance to photobleaching, low toxicity, and ability to convert NIR light into shortwave light in the UV-visible spectral range. UCNPs typically consist of a host material like NaYF_4 doped with lanthanide ions such as Er^{3+} , Yb^{3+} , and Tm^{3+} , which possess discrete energy levels. Upon NIR illumination, these lanthanide ions absorb low-energy photons through sequential multi-photon absorption or energy transfer processes. A common mechanism, energy transfer upconversion (ETU), involves an ion like Yb^{3+} absorbing a photon and transferring its energy to another ion like Er^{3+} , allowing the absorption of multiple low-energy photons. In a typical two-photon upconversion process, a lanthanide ion absorbs two photons sequentially, first exciting the ion from the ground to an intermediate state and then to a higher energy state. The absorbed energy is often transferred from a sensitizer ion (e.g., Yb^{3+}) to an activator ion (e.g., Er^{3+}), which emits a higher-energy photon. Once in the excited state, these ions can return to lower energy states by emitting photons (radiative relaxation), observed as upconversion luminescence, while minimizing non-radiative relaxation to maintain high upconversion efficiency. The application of PEC biosensors based on NIR radiation of UCNPs for detecting biomarkers in the clinical field has also been demonstrated. Tang et al. [188] presented a proof of concept of a PEC platform for the sensitive detection of carcinoembryonic antigen (CEA) under 980 nm NIR excitation, using core-shell $\text{NaYF}_4:\text{Yb},\text{Tm}@\text{TiO}_2$ UCNPs (*Figure 6C*). The

detection strategy was based on light conversion from NIR to UV and signal amplification by rolling circle amplification (RCA). The platform employed a sandwich assay with two CEA-targeting aptamers immobilized on biofunctional magnetic beads, activating RCA to produce a long guanine (G)-rich oligonucleotide strand. Enzymatic digestion released G bases by enhancing the photocurrent under NIR light excitation. This approach took advantage of the minimal photobleaching and low phototoxicity of NIR light by efficiently converting it to UV light to activate the TiO₂ layer and generate a photocurrent increase proportional to the CEA concentration. The device exhibited high sensitivity with an LOD of 3.6 pg/mL, in a linear range of 0.01-40 pg/mL ($R^2 = 0.994$), and successfully detected CEA in serum samples. This novel PEC biosensing system is promising for detecting low-abundance biomolecules in biological fluids using UCNPs.

Figure 6. A) $WS_2/AuNPs$ modified platform for PEC cytosensing of MCF-7, reproduced with permission from Ref [186]. B) PEC cytosensing of MCF-7 based on ITO/Ag₂S/Au heterojunction, reproduced with permission from Ref. [187]. C) FTO/NaYF₄:Yb,Tm@TiO₂ platform for PEC detection of CEA, reproduced with permission from Ref. [188]. D) PEC detection of variable concentrations of AA based on GC/AuNS heterojunction, reproduced with permission from Ref. [189].

UCNP-activated systems have been extensively used for PEC biosensing due to their ability to function as non-invasive sensitizer systems activated by 980 nm radiation, which in turn activates heterojunction systems between UCNP and metals, metal oxides, and QDs through visible radiation emitted via fluorescence processes. The detection of alpha-fetoprotein (AFP) has been achieved through the heterojunction between NaYF₄:Yb,Tm/ZnO/CdS [191] and NaYF₄:Yb,Er@Au@CdS [200], as shown *Table 2*. Additionally, the detection of carcinoembryonic antigen (CEA) has been conducted using UCNP heterojunctions based on NaYF₄:Yb,Tm@ZnO [195], NaYF₄:Yb,Er/Ag₂S [178], and NaYF₄:Yb,Er@CdTe [199]. These studies demonstrate the versatility of such systems for analyte detection based on the conjunction of different types of materials in hybrid systems, which enhance the detection performance of PEC systems and pave the way for ongoing research into nanostructured platforms based on UCNP.

5. Photoelectrochemical detection of C-reactive protein

Per the International Union of Pure and Applied Chemistry (IUPAC), a biomarker is an objectively measurable characteristic that indicates normal biological processes, pathogenic activities, or responses to therapeutic interventions [201]. Biomarkers encompass molecules, genes, proteins, or other cellular components [202], which are quantified to ascertain their biological significance in detecting various disease types and predicting disease progression and response to diverse treatments [203]. The identification of numerous established biomarkers has been extensively employed in studying treatment responses and evaluating therapeutic effects across a range of diseases, including cancer [204], diabetes [205], HIV [206], cardiovascular ailments [207], neurodegenerative conditions [208], and emerging infectious diseases [7]. They pose challenges requiring accurate development amidst ongoing technological and scientific advancements [209] and underscore the essential role of reliable biomarkers associated with highly sensitive and selective detection methods in laying the groundwork for advancing disease diagnosis biosensors [210].

Human CRP is a significant acute-phase reactant protein synthesized in the liver and found in blood plasma [211]. CRP is one of the most extensively employed clinical biomarkers for cardiovascular disorders, firmly entrenched in standard clinical practice [212]. Minute fluctuations in CRP values can be discerned using high-sensitivity CRP (hs-CRP) assays [213]. The risk associated with cardiovascular diseases varies based on CRP concentration, as researched by the American Heart Association and the Centers for Disease Control and Prevention [214]. CRP levels between 1 and 3 mg/L indicate intermediate vascular risk, levels exceeding 3 mg/L reflect elevated vascular risk, and levels below 1 mg/L indicate a low systemic inflammatory status deemed optimal [215]. Hs-CRP levels surpassing 10 mg/L signify the potential of an acute-phase reaction or a transient infectious ailment, requiring reevaluation within two to three weeks [216]. The sensitive measurement of CRP levels in biological samples requires swift, dependable, selective, and minimally invasive analytical techniques for hs-CRP quantification [217]. An ideal technology would be user-friendly, affordable, and widely applicable in clinical diagnostics, particularly for preempting severe inflammatory conditions [218]. Numerous methods, encompassing the enzyme-linked immunosorbent assay (ELISA), electrochemical-, surface plasmon resonance-, fluorescence-, and chemiluminescence- assays, have been harnessed for in vitro CRP detection [219]. These techniques must be adept at detecting CRP at concentrations below pg/mL for comprehensive CRP detection across populations. Among these methods, ELISA is predominantly used for in vitro CRP detection [220]. However, situations demanding higher sensitivity necessitate heightened CRP detection methods. Therefore, methods that enable swift and economical detection are desirable.

Table 3 provides a concise overview of PEC CRP detection, focusing on the analytical properties of devices using multiple photoactive nanomaterials across a broad spectral range. Typically, it is combined with electrochemical or PEC methodologies to discuss the analytical properties of the assay compared to the standard ELISA detection [221]. The PEC approaches presented in the table encompass a range of signaling strategies grounded in the properties of photoactive materials comprising the working electrode. Particular attention is given to the selection of redox media, which depends on the target analyte to detect. High CRP concentration levels indicating complications due to inflammatory processes are often much higher than the LOD achieved by the PEC devices outlined in the table. This fact can be justified by the exceptional sensitivity of PEC

devices and the potential use of these low LODs for collaborative diagnostics, enhancing the biomarker analysis for intelligent patient diagnosis [30].

Table 3. (Photo)electrochemical biosensors for C-reactive protein detection

Working electrode	Electrolyte / Redox probe	λ_{exc} (nm)	Technique	Linear range	LOD	Matrix	Refs
ITO/NiS/p-COF/Ag NPs	PBS 10X / H ₂ O ₂	414	Chrono-amperometry	0.5 – 100 ng/mL	0.1 ng/mL	Human serum	[222]
GCE/PCN-777/DepAu	PBS 10X / H ₂ O ₂	365	Chrono-amperometry	50 fM – 50 nM	16 fM	Synthetic serum	[223]
GCE/PTB7-Th/DepAu	PBS 10X / H ₂ O ₂	365	Chrono-amperometry	1 pM – 1000 nM	0.33 pM	Human serum	[224]
GCE/TiO ₂ /PTCDA/depAu	PBS 10X / H ₂ O ₂	365-370	Chrono-amperometry	10 pg/mL – 10 μ g/mL	3.33 pg/mL	Synthetic serum	[225]
CMF/TiO ₂ /Au NCs/AuNPs	Tris-HCl / TEOA	425	Chrono-amperometry	1 pg/mL – 200 ng/mL	1 pg/mL	Human serum	[226]
CdS/TiO ₂ NTs	PBS 10X / AChE	410	Chrono-amperometry	50 ng/mL-50 μ g/mL	50 ng/mL	Synthetic serum	[227]
GCE/PEI-Fc	PBS 1X / K ₂ SO ₄	-	DPV	1 - 5·10 ⁴ ng/mL	0.5 ng/mL	Human blood	[228]
Au/MB	PBS 1X / Ru(NH ₃) ₆ ³⁺	-	SWV	1-100 pM	1 pM	Human serum	[229]
AuNPs@BP@ PDA	PBS 1X / [Fe(CN) ₆] ^{3-/4-}	-	SWV	0–0.036 μ g/mL	0.7 ng/mL	Human plasma	[230]
oxSPCE/ AuNSs	PBS 1X/AA	765	Chrono-amperometry	0.025-0.8 ng/mL	13.3 pg/mL	Human serum	Chapter III

AChE: acetylthiocholine, Ag: silver, ALP: alkaline phosphatase enzyme, BP: black phosphorus, CdS: cadmium sulfide, CMF: 3D carbon fiber matrix, DepAu: electrodeposited gold nanoparticles, DPV: differential pulse voltammetry, GCE: glassy carbon electrode, ITO: indium tin oxide, LOD: limit of detection, MB: methylene blue, NCs: nanocubes, NiS: nickel sulfide, NTs: nanotubes, p-COF: covalent organic frameworks, PCN-777: zirconium-based metal-organic framework, PDA: polydopamine, PEI-Fc: ferrocene-functionalized polyethylenimine, PTCDA: 3,4,9,10-perylene tetracarboxylic dianhydride, PTB7-Th: poly{4,8-bis[5-(2-ethylhexyl)thio-phen-2-yl]benzo[1,2-b:4,5-b']dithiophene-2,6-diyl-alt-3-fluoro-2-[(2-ethylhexyl)carbonyl] thieno[3,4-b]-thiophene-4,6-diyl}, Ru(NH₃)₆³⁺: ruthenium hexamine, SWV: square-wave voltammetry, TEOA: triethanolamine, Th-T: thioflavin, TiO₂: titanium dioxide, and λ_{exc} : excitation wavelength.

Hu et al [222] presented a clear example of showcasing the CRP detection approach using the PEC technique. They performed a label-free assay on an ITO platform modified with nickel sulfide (NiS) QDs and Ag nanoparticles. These nanoparticles acted as anchor points for a 2D metal-organic framework and, in the process, altered the electrical properties of the surface, leading to the

modulation of the decay terms in the photocurrent response in target detection. Enhanced efficiency in converting photocurrent and increased photocurrent intensity were additionally boosted by active molecules like H_2O_2 , which served as electron donors for the heterostructure composed of ITO/NiS/p-COF/Ag NPs. CRP detection was conducted using an aptamer that specifically recognized CRP, hindering the platform's electron transfer and decreasing the photocurrent response. This response reduction was employed for the analytical detection of CRP. This work was one of the first to achieve CRP detection at low concentrations (0.5–100 ng/mL) and opened the door to research methodologies that enable specific and selective CRP detection using PEC techniques.

Chai *et al.* [223], [224] developed two approaches to CRP detection using different PEC strategies based on glassy carbon electrodes (GCE). They initially developed an assay based on the GCE/PCN-777/DepAu heterostructure and a thioflavin (Th-T) sensitizer. Consequently, the PEC signal in this study experienced significant enhancement, primarily due to Th-T's highly effective sensitization effect toward PCN-777, enabling sensitive monitoring of CRP. The emergence of Th-T as a byproduct of the specific biomolecular amplification process effectively sensitized PCN-777, resulting in a significantly enhanced PEC response for achieving ultrasensitive quantitative CRP detection in the range of 50 fM–50 nM with a LOD of 16 fM. This study pioneered an ultrasensitive technique like PEC for CRP detection in H_2O_2 as a redox medium, facilitating the quantification of the generated photocurrent signal. On the other hand, the authors developed a label-free PEC aptasensor based on a conjugated polymer and H_2O_2 system for easy, rapid, and sensitive detection of CRP. The authors coated the electrode interface with PTB7-Th, generating a strong initial PEC signal in the H_2O_2 system. Subsequently, they applied a gold layer (DepAu) to the surface. They then utilized an aptamer, which served as the receptor layer for detecting the CRP target through specific aptamer-CRP recognition. The aptamer-CRP complex formed impeded electron transfer, leading to a substantial reduction in the PEC signal, thereby enabling the precise quantification of CRP. This research not only showcased the unanticipated photoelectric behavior of the PTB7-Th/ H_2O_2 system but also introduced a novel approach for detecting CRP with high sensitivity, covering a concentration range from 1 pM to 1000 nM, and achieving a remarkable LOD of 0.33 pM, which holds promise for early disease diagnosis.

Another example was conducted by Xia *et al.* [225]. They sensitized a TiO_2 -coated GCE surface with 3,4,9,10-perylene tetracarboxylic dianhydride (PTCDA), generating a robust PEC signal.

Gold nanoparticles (AuNPs) were electroplated onto the PTCDA/TiO₂/GCE surface to couple an aptamer as biorecognition elements. The detection process generated CRP-aptamer complexes, causing steric hindrance that obstructed electron transfer, consequently leading to a diminished PEC signal. The experimental conditions utilized in this research enabled the development of an innovative PEC aptasensor utilizing the AuNPs/PTCDA/TiO₂-sensitized structure to detect CRP within a concentration range spanning from 10 pg/mL to 10 µg/mL, with an impressive LOD of 3.33 pg/mL.

Finally, a CMF/TiO₂/AuNCs/AuNPs organic electrochemical transistor (OECT) platform with an ALP-biocatalytic label was developed to detect CRP, as demonstrated Zhao *et al.* [226]. A sandwich immunoassay involving a primary antibody and an ALP-conjugated secondary antibody was employed. In this process, the biocatalytic transition of gold nanocages (AuNCs) into AuNPs was facilitated by reducing Au³⁺ using AA. This transition significantly altered the absorption characteristics of the photoelectrodes, switching from the semiconductor-based behavior of AuNCs to the plasmonic response of AuNPs. This unique conversion impacted the light-induced response in PEC detection of CRP. The assay successfully detected CRP within a 1 pg/mL concentration range to 200 ng/mL with a 1 pg/mL LOD.

6. Characterization of PEC biosensors

The accurate and rigorous characterization of PEC interfaces is crucial in developing reproducible and trustworthy detection assays. The most widely used techniques for characterizing PEC biosensing are listed in *Table 4*. Typically, the most relevant parameters of PEC platform surfaces are characterized by surface chemistry, morphology, and PEC performance. Energy-dispersive X-ray spectroscopy (EDS) is a powerful analytical technique for characterizing PEC biosensors. It provides valuable information about the elemental composition, material characterization, surface modification verification, quality control, material degradation studies, and correlation with materials within the PEC system [107]. Furthermore, Fourier-transformed infrared spectroscopy (FT-IR or Raman) and X-ray photoelectron spectroscopy (XPS) are versatile analytical techniques that can be used in PEC biosensors characterization to provide insights into molecular composition, chemical bonds, surface functionalization, and the monitoring of chemical changes. FT-IR and XPS enhance the understanding of PEC biosensor behavior by offering information about the chemical nature of the sensor's surface and the biomolecule-analyte interactions [231], [232].

Alternatively, ultraviolet-visible diffuse reflectance spectroscopy (UV-Vis DRS) is a valuable analytical technique employed in PEC biosensors to investigate the optical properties of materials, specifically their absorption and reflectance of ultraviolet and visible light. This technique is essential for band gap determination, quantification of photogenerated carriers, monitoring chemical changes, studying the kinetics of PEC reactions, and characterizing the performance of functionalized surfaces [233]. Photoluminescence (PL) can be utilized in PEC biosensors to investigate the emission of light, usually fluorescence, from materials exposed to photons, typically from a light source. PL is commonly used for characterizing fluorescent labels, enhancing sensitivity, monitoring redox reactions, conducting kinetic studies, enabling multiplexed detection, and facilitating real-time monitoring of PEC surfaces [234].

Scanning electron microscopy (SEM), field emission scanning electron microscopy (FESEM) [235], and atomic force microscopy (AFM) [133] are powerful surface analytical techniques that can be used in PEC biosensors to study the surface morphology, structure, and composition of materials. Together, they provide comprehensive analyses of morphology, nanostructuring, chemical composition, real-time monitoring, and interaction analysis during the immobilization of biomolecules. Electrochemical techniques, including cyclic voltammetry (CV), electrochemical impedance spectroscopy (EIS), and chronoamperometry, play crucial roles in developing and characterizing PEC biosensors. CV is relevant for determining redox properties, measuring band gaps and energy levels, kinetic studies, and assessing sensitivity in PEC devices [236]. On the other hand, EIS is used to characterize interfacial properties, monitor charge transfer resistance, and understand charge transfer rates and diffusion processes [237]. Chronoamperometry is commonly used for real-time monitoring and steady-state current measurements [238].

The surface chemistry, morphology, and structural properties of nanostructured materials that alter the interfaces in PEC biosensors are meticulously characterized to optimize the analytical performance of these devices. Transmission electron microscopy (TEM) is a powerful technique used to investigate nanoscale structures and compositions, offering exceptional resolution and the ability to observe internal structures [239]. X-ray diffraction (XRD) is a fundamental tool in materials research and crystallography, providing detailed information about atomic arrangements in crystals, which is essential for understanding material properties at the atomic scale [240]. Dynamic light scattering (DLS) and electrophoretic light scattering (ELS) are typically employed to study size and surface charge [241] for characterizing colloidal systems.

Table 4. *Characterization techniques of PEC biosensing interfaces*

Properties	Characterization technique	Use in PEC systems	Ref
<i>Surface chemistry</i>	EDX	Backscattered electrons in electron microscopy are employed to obtain elemental mapping of the composition of the PEC interface.	[107]
	FTIR – Raman	The functional groups available for anchoring photoactive nanomaterials and biological recognition elements are characterized by measuring the different vibrational modes determined by the bonds of atoms from these groups.	[231]
	XPS	XPS offers the ability to characterize the PEC interface's chemical composition accurately. It is also helpful in monitoring the biosensor assembly based on the types of bonds formed.	[232]
	UV-vis DRS	This technique leads to the characterization of solid interfaces by dispersing a fraction of the incident UV-Vis radiation on its surface, as seen in PEC systems with photoactive nanomaterials.	[233]
	PL	The photoactivity of materials nanostructured on the PEC biosensing interface is characterized by photoluminescence (PL), which involves the spontaneous emission of light from a material under optical excitation.	[234]
<i>Morphology</i>	SEM - FESEM	The modification of PEC interfaces with nanostructured photoactive materials can be characterized using SEM by scanning with secondary and backscattered electrons. Furthermore, SEM with field emission (FESEM) can be used to attain higher resolution, improving the observation of nanoscale details.	[235]
	AFM	Critical morphological properties, such as surface topography, interaction forces, mechanical properties, electrical properties, and biomolecular interactions, can be measured at PEC sensing interfaces.	[133]
	XRD	XRD enables the analysis of critical structural properties, such as crystallographic structure, phase identification, lattice parameters, crystal orientation, and strain in materials at PEC sensing interfaces.	[240]
<i>Electrochemistry</i>	CV	CV can be used to investigate redox reactions in the PEC biosensor and to measure the photocurrent generated when light activates the photoactive material in the presence of the analyte. This technique measures the photocurrent response across a range of potentials, enabling the determination of redox potentials and reaction kinetics.	[236]
	EIS	EIS is employed to analyze the electrical impedance of the PEC system over a range of frequencies. It can provide insights into charge transfer resistance, adsorption processes, and other electrochemical properties relevant to PEC biosensing.	[237]
	Chronoamperometry	This technique involves measuring the photocurrent at a fixed potential over a specific period. By monitoring changes in photocurrent over time, chronoamperometry can provide kinetic information about the interaction between the analyte and the bioactive elements on the sensor surface.	[238]

7. Concluding remarks and perspectives

PEC analysis and ongoing research in photoactive materials as transduction platforms have garnered extensive attention to enhance these devices' analytical performance. It is achieved by addressing PEC detection systems' inherent challenges, acquiring new nanomaterials, and designing novel detection strategies. For example, nanomaterials capable of facilitating energy

interconversion processes with superior efficiency have boosted the ultrasensitive, reproducible, and stable detection of various bio-analytes. Optoelectronic properties of nanomaterials exhibiting semiconductor behavior, including various metal oxides, carbon nitrides, QDs, and TMCs, have been extensively exploited for this purpose. However, challenges still must be tackled fully by a broader range of excitation sources covering more portions of the visible and NIR spectral range. Therefore, detection strategies aimed at enhancing the PEC behavior of devices have shifted towards sensitizing the materials with counterparts excitable at longer wavelengths and lower energy levels. Adopting red light and NIR excitation in PEC devices may overcome the limitations of existing (bio)sensors primarily reliant on UV-vis light that restricts their potential applications, particularly *in vivo*, due to its shallow tissue penetration. NIR light, spanning wavelengths greater than 650 nm, enjoys minimal spectral interference, deep tissue penetration, and limited damage to biological entities.

The possibility of miniaturizing detection assays is another strength of PEC devices, enhancing electrode design versatility without compromising performance metrics like electron transport and stability. Miniaturization enables multi-analyte detection in single measurements, essential for POC devices that improve disease diagnosis and intervention. Leveraging patient-specific biology, physiology, and genetic precision medicine promises to revolutionize healthcare by predicting disease risks and treatment responses. In this context, transformative diagnostics incorporate smart, innovative devices and informatic approaches using big data analytics, the Internet of Things (IoT), machine learning, blockchain, artificial intelligence (AI), augmented reality, system integration, cloud and fog computing, and smartphones, offering advanced healthcare solutions through cutting-edge converging technologies. Integrating PEC devices with these advanced systems enhances their capability to deliver precise and rapid multi-analyte detection in real-time, which is crucial for effectively implementing precision medicine. However, most research involving PEC devices for biosensing assays employs spectral ranges in the tail of the UV region, the near-UV-visible region, or a combination of the entire visible region, overlooking the significant advantages of red light and the NIR range. Integrating these underutilized spectral ranges could further enhance the sensitivity and effectiveness of PEC devices in advanced smart diagnostic applications.

The advantages of using metal oxides and carbon nitrides in PEC biosensors are substantial. As described by conventional band theory, metal oxides offer wide-space ionic structures with minimal curvatures in their electronic bands, resulting in smaller effective masses and enhanced

carrier mobility. Conversely, carbon nitrides provide an adjustable band gap for tunable electrical conductivity, light response, and high transparency across a broad spectrum of wavelengths, making them ideal for PEC detection devices. These properties make metal oxides and carbon nitrides valuable in advancing PEC biosensors, enhancing their performance, and expanding their applications in various fields. Their high carrier charge mobility holds promise for high-speed electronic devices like thin film transistors and photovoltaic devices. Furthermore, their photoluminescent properties facilitate light emission upon electromagnetic radiation excitation, proving useful in (bio)sensors and lighting devices. Their high mechanical strength makes them ideal for optical and electronic devices requiring robust and durable materials.

Semiconductor QDs activated by UV radiation offer optoelectronic properties such as tunable size, high photoluminescence quantum yield, quantum confinement effect, and strong absorption coefficients. Their high excitation efficiency enables effective absorption and conversion of UV light into visible emission, making them ideal for light-emitting devices. The adjustable emission spectrum of QDs, achieved by varying their size, is valuable for biosensors, displays, and as marks of biomolecules. Their stability and durability ensure consistent performance over time under various conditions, and their compatibility with flexible substrates allows for use in flexible electronic and optoelectronic devices like wearable displays and (bio)sensors. TMCs with high excitation efficiency also convert UV light into visible light, which is helpful for light emission devices. Their wide adjustable band gap range enhances versatility, and their stability and good light dispersion improve the uniformity and quality of emitted light in lighting and display applications.

Exploiting the benefits of PEC systems activated at wavelengths exceeding 650 nm is worth mentioning. Their profound tissue penetration, cellular safety, and detector stability capabilities enable the detection of biomolecules within dense samples, including tissues and bodily fluids, rendering them promising for biomedical and diagnostic applications. Additionally, they effectively mitigate autofluorescence, thereby increasing sensitivity and selectivity by minimizing interference from biological components. Moreover, these systems inflict minimal damage to cells and tissues, facilitating real-time measurements under physiological conditions without adverse effects. For example, notable optoelectronic properties of plasmonic nanoparticles enhance light capture and conversion efficiency through plasmonic coupling, thereby increasing detection sensitivity and enabling the detection of biomolecules at low concentrations. Energy UCNPs can

convert infrared light into visible or ultraviolet light, allowing biosensors to be excited with shorter wavelengths and enhancing detection efficiency by reducing the autofluorescence of biological components. NIR-activated QD, which absorb NIR light and emit visible light, are helpful for exciting PEC biosensors, thereby improving the sensitivity and selectivity of biomolecule detection. Photonic crystals manipulate and control light propagation at specific wavelengths, improving light capture efficiency and detection sensitivity.

Furthermore, PEC systems feature photodetectors characterized by enhanced stability, ensuring precise and reproducible measurements over extended periods. Their integration with biosensing approaches, such as optical coherence tomography and in vivo fluorescence imaging, paves the way for further positioning these devices into imaging systems tailored for biomedical applications. These technologies promise to develop more sensitive, selective, and efficient PEC biosensors for biomedical, food safety, and environmental applications, thus revolutionizing clinical diagnostics, pathogen detection, and environmental monitoring, ultimately improving society's health and well-being.

CHAPTER III: Assembly, analytical characterization, and performance of the PEC nano-immunosensor

Adapted from: Monsalve, Y., Cruz-Pacheco, A.F. & Orozco, J. Plasmonic graphene-gold nanostar heterojunction for red-light photoelectrochemical immunosensing of C-reactive protein. ACS Sensor. 2024. *Submitted article.*

Abstract

The development of red-light photoelectrochemical (PEC) nano-immunosensors offers new avenues for detecting clinically relevant biomarkers with high sensitivity and specificity. Herein, the first PEC nano-immunosensor based on a plasmonic graphene and gold nanostars (AuNSs) heterojunction excited with 765 nm red light is presented for label-free detection of C-reactive protein (CRP), a key biomarker of inflammation. This platform leverages the unique localized surface plasmon resonance effect of AuNSs in combination with in-situ generated graphene to enhance photoelectrical conversion efficiency under 765 nm monochromatic light. This wavelength minimizes photodamage and interference from biological samples. By optimizing the nano-architecture and utilizing a bifunctional photoactive transduction platform, a linear detection range of 25–800 pg/mL is achieved, with a limit of detection as low as 13.3 pg/mL. The low-energy red-light activation, effective electron-hole pair separation, and signal amplification allow CRP's rapid, selective, and sensitive detection in real clinical samples from patients with low-grade chronic inflammation. The nano-immunosensor demonstrated consistent analytical performance across multiple samples, showing potential for accurate biomarker monitoring in inflammatory disorders. This work highlights plasmonic nanomaterials to develop robust PEC immunosensors that provide scalable, noninvasive, automated, low-background noise as a highly sensitive alternative for clinical diagnostics.

1. Introduction

PEC nano-immunosensors have emerged as promising tools in bioanalysis because they provide specific quantitative or semiquantitative data about (bio)analytes by detecting photocurrent variations resulting from biological recognition events [11], [23] These sensors harness nanoscale components and light-matter interactions to transform biological signals into electrical outputs,

benefiting from improved electron-hole pair separation and signal enhancement [173]. The construction of PEC nano-immunosensors involves nanostructured materials conjugated with an antibody serving as a bioreceptor, which selectively binds to the target analyte, coupled with a transducer that translates this binding event into a detectable electrical signal [12]. The PEC technique effectively minimizes background noise by isolating the light source for excitation from the resulting detection signal, thereby providing higher sensitivity than conventional methods [41]. Additionally, long-wavelength, low-energy excitation—up to 620 nm in the red and near-infrared (NIR) range—proves advantageous for noninvasive monitoring of biological samples, reducing photodamage and avoiding interference caused by absorption or scattering of shorter wavelengths [3]. PEC nano-immunosensors offer adaptable optical properties, photostability, robustness, and compatibility with various surface nanostructures from their exceptional sensitivity, specificity, quick response, and flexibility, [242], [243], [244], [245]. A novel strategy for label-free detection under 765 nm excitation has been developed to maximize these characteristics, advancing the application of these biosensors in clinical diagnostics and biomarker analysis. Incorporating high-surface-area photostimulable nanomaterials onto transducer platforms has markedly improved the performance of PEC devices by facilitating more efficient energy transfer and enhancing signal transduction, resulting in devices that exhibit superior sensitivity, stability, and reproducibility [174]. A plasmon is a collective oscillation of free electrons within a metal or semiconductor material, triggered when the material is exposed to light, creating an electromagnetic field that resonates at a specific frequency, which can lead to intense localized electric fields and enhanced absorption or light scattering [246]. The creation of heterojunctions by pairing plasmonic nanostructures with semiconductors substantially increases photocatalytic activity by transferring plasmonic energy from the metal nanostructure to the semiconductor. Localized surface plasmon resonance (LSPR) occurs on the surfaces of metal nanostructures—such as gold, silver, copper, and aluminum—when illuminated. Plasmonic nanostructures are especially influential in broadening the light absorption range of semiconductors, acting as adjustable light sources across the entire visible spectrum [247], [248].

Graphene has garnered significant interest across various fields due to its exceptional electrical conductivity, mechanical strength, large surface area, remarkable carrier mobility, unique optical properties, and ease of functionalization. It is a versatile material for applications in electronics [249], energy storage [250], and sensing technologies [251]. Plasmons in graphene are collective

oscillations of electrons confined to its two-dimensional structure. Unlike conventional metals, graphene plasmons can be precisely controlled by external factors like electrical gating, chemical doping, or the formation of heterojunctions with other plasmon-active nanomaterials, allowing modulation of their frequency and amplitude [252]. These properties make graphene an excellent candidate for plasmonics applications, including light manipulation, energy transfer, and optical communications [253]. Due to graphene's distinctive electronic properties, such as its linear energy-momentum relationship and Dirac fermion behavior, graphene exhibits high energy confinement, tunability via carrier density control, and low energy losses when excited by visible red light. These characteristics enable efficient light-matter interactions, enhancing energy transfer processes, particularly when coupled with semiconductors [254]. To further promote graphene's photoelectric conversion efficiency and produce enhanced photocurrent, LSPR elements must be introduced. AuNSs, branched nanoparticles with sharp tips and complex morphologies, possess tunable optical properties and are widely used in sensing, imaging, and photothermal therapy [255]. These nanostructures exhibit a unique LSPR effect due to the collective oscillation of conduction electrons on their surface when exposed to light. The sharp tips of AuNSs intensify the LSPR effect, generating highly localized electromagnetic fields. This phenomenon is highly sensitive to changes in the size, shape, and dielectric environment surrounding the nanostars [256]. Typically, the LSPR in AuNSs shifts towards the NIR region, facilitating applications in bioimaging and therapeutic processes. Theoretical studies of LSPR in AuNSs have demonstrated that their branched morphology, tip curvature, and material composition enhance their optical response, providing strong tunability and high sensitivity to molecular binding events [257]. Thus, coupling plasmonic graphene with plasmonic AuNSs can take advantage of high carrier mobility, low energy loss, branched morphologies with enhancement of electromagnetic fields, and low-energy red light interaction capability compared to conventional high-energy UV-visible PEC sensing formats [118], [258], [259].

CRP is an acute-phase protein the liver produces in response to inflammation, regulated by cytokines such as interleukin-6 (IL-6) and tumor necrosis factor-alpha (TNF- α) [260]. CRP plays a crucial role in the immune response by tagging pathogens and damaged cells for clearance. It is a biomarker of systemic inflammation frequently used to assess cardiovascular disease risk [5]. Obesity is characterized by chronic low-grade inflammation, partly due to adipose tissue accumulation. Adipocytes and infiltrating immune cells in fat tissue secrete pro-inflammatory

cytokines, including IL-6 and TNF- α , which stimulate CRP production in the liver [261]. Elevated CRP levels in obese individuals are associated with increased cardiovascular risk, insulin resistance, and metabolic syndrome. Chronic inflammation in obesity may worsen metabolic disorders, and the strong correlation between body mass index (BMI) and CRP suggests a direct link between excess adiposity and increased inflammatory responses. Developing CRP detection assays is essential for the early identification of obesity-related conditions, enabling timely intervention for cardiovascular risks and metabolic disorders linked to chronic inflammation [262]. In this work, a heterojunction of electrogenerated graphene edge planes on screen-printed carbon electrodes (SPCE) and electroplated gold nanostars (AuNSs) was coupled for the first time for label-free red-light PEC immunosensing of CRP in serum samples from patients with different levels of inflammation. The in-situ generation of graphene with plasmonic activity, enhanced by the LSPR effect of specifically designed AuNSs, enabled efficient harvesting of 765 nm red light to produce photoinduced electrons directly injected into the electrochemical cell. Using a low-energy radiation source with bifunctional photoactive nanomaterials as a transduction platform may prevent damage or denaturation of biomolecules involved in the detection architecture. The photogenerated holes produced by the heterojunction photoactive materials were scavenged by ascorbic acid (AA) for photocurrent generation. The label-free architecture was effectively used for the sensitive, selective, specific, rapid, and automated detection of CRP, a clinically relevant biomarker in disorders associated with low-grade chronic inflammation. The PEC nano-immunosensor was validated using ten real samples with different CRP levels, indicating the severity of the inflammatory state in these individuals.

2. Experimental section

2.1. Reagents and solutions

Potassium ferricyanide (III) ($K_3[Fe(CN)_6]$), potassium hexacyanoferrate (II) trihydrate ($K_4[Fe(CN)_6] \cdot 3H_2O$), and sodium chloride (NaCl) were purchased from Merck Millipore. Disodium hydrogen phosphate (Na_2HPO_4) and ascorbic acid (AA) were sourced from PanReac AppliChem, while potassium dihydrogen phosphate (KH_2PO_4) and potassium chloride (KCl) were acquired from J.T. Baker[®]. Bovine serum albumin (BSA), glucose, Nafion[™] perfluorinated resin solution, gold (III) chloride trihydrate ($HAuCl_4 \cdot 3H_2O$), sodium dodecyl sulfate (SDS), silver nitrate ($AgNO_3$), sodium citrate tribasic dihydrate ($Na_3C_6H_5O_7 \cdot 2H_2O$), human serum, and 4-

mercaptobenzoic acid (4-MBA) were all procured from Sigma-Aldrich. Sulfuric acid (H_2SO_4) and hydrochloric acid (HCl) were acquired from Honeywell-Fluka. Human C-Reactive Protein (CRP) DIY ELISA Kit (MBS2088838) was obtained from MyBioSource. Procalcitonin (PCT) DIY ELISA Kit (ab222276) was obtained from Abcam. Tumor necrosis factor alpha ($\text{TNF-}\alpha$) DIY ELISA Kit (DY210-05), interleukin- 1β (IL- 1β) DIY ELISA Kit (DY201-05), interleukin-6 (IL-6) DIY ELISA Kit (DY206-05), interleukin-8 (IL-8) DIY ELISA Kit (DY208-05), interleukin-10 (IL-10) DIY ELISA Kit (DY217B-05), interleukin-18 (IL-18) DIY ELISA Kit (DY318-05) were acquired from R&D Systems. All reagents were used as received, and solutions were prepared using deionized water ($18.2 \text{ M}\Omega\cdot\text{cm}$) from a Thermo Scientific Barnstead GenPure ultrapure water purification system. Phosphate-buffered saline (PBS 1X) contained 0.01 M phosphate buffer, 0.138 M NaCl, and 0.0027 M KCl, with the pH adjusted to 7.4. All protein and cell solutions were diluted in PBS 1X, pH 7.4.

2.2. Equipment

The morphology and particle size of the AuNSs were analyzed using HR-TEM with a Tecnai F20 Super Twin TMP microscope, operating at an accelerating voltage of 200 keV. Particle size and crystalline parameters were analyzed using ImageJ [263] and DigitalMicrograph [264] software, respectively. Additionally, the structural properties of the synthesized AuNSs were further examined through XRD using a Malvern PANalytical Empyrean diffractometer equipped with a PIXcel3D solid-state detector. The analysis was conducted with $\text{CuK}\alpha$ radiation ($\lambda = 1.5418 \text{ \AA}$) over a 2θ range from 20° to 90° . The measurements were carried out at an accelerating voltage of 45 kV and a current of 40 mA. The diffraction pattern was obtained in reflection geometry, with a step size of 0.05° and a counting time of 54 s per step. Surface charge and particle size distribution were determined using ELS and DLS, respectively, with a Malvern particle size analyzer (Zetasizer Pro Blue Label, Malvern Instruments). The Au-seeds' UV-vis absorption properties and stabilized AuNSs were measured using a Thermo Scientific Microplate Spectrophotometer (VARIOSKAN LUX).

PEC experiments were performed using a UV LED Spot Curing System and a PalmSens³ potentiostat/galvanostat with PSTrace 5.1 software. Electrochemical measurements utilized Metrohm DropSens screen-printed carbon electrodes (SPCEs, ref. DRP-110/Oviedo-Spain). The morphology and chemical composition of modified SPCEs were analyzed by uncoated FE-SEM.

AFM images were captured in tapping mode using an Asylum Research MFP-3D Infinity microscope and analyzed with Gwyddion software. Raman spectra were obtained with a Horiba Jobin Yvon confocal Raman spectrometer featuring a He/Ne laser (633 nm) and a CCD detector (1024 x 256 pixels) to measure Raman intensity. UV-vis diffuse reflectance absorption properties of AuNS-modified SPCEs were evaluated using a CARY 100 Conc UV-vis spectrometer (UV 1104M284).

2.3. Synthesis of 4-MBA-coated gold nanostars (AuNS@4-MBA)

Firstly, AuNPs@SC were synthesized utilizing sodium citrate (SC) as the reducing and stabilizing agent [265]. 100 mL of 0.001 M $\text{HAuCl}_4 \cdot 3\text{H}_2\text{O}$ was placed in a 250 mL three-necked flask until boiling. 15 mL of a 0.5 M SC solution was added to the gold solution, followed by vigorous stirring for 15 min. The solution changed color from pale yellow to ruby red, indicating the formation of AuNPs@SC. The solution changed color from pale yellow to ruby red, indicating the formation of AuNPs@SC. The flask was cooled in an ice bath and stirred for an additional 30 min. AuNPs@SC were centrifuged 3 times at 15000 rpm for 20 min and redispersed in deionized water. AuNPs@SC were stored at 4 °C to maintain stability and prevent aggregation. AuNSs@SDS were prepared by mixing 1 mL of AuNPs@SC dispersion with 100 mL of 0.25 mM $\text{HAuCl}_4 \cdot 3\text{H}_2\text{O}$ and 100 μL of 1 M HCl. 200 μL of 0.01 M AgNO_3 , 500 μL of 0.1 M AA and 100 μL 0.1 M SDS were sequentially added to the initial solution at room temperature [264]. The final solution was stirred at 1000 rpm for 30 s until the color changed from ruby red to dark bluish. The mixture was centrifuged at 10000 rpm for 5 min at 4 °C, and the AuNSs@SDS were redispersed in 50 mL of water. The surface ligand of AuNSs@SDS was exchanged for 4-MBA by adding 15 mL of the previously synthesized AuNSs@SDS with 150 μL of 20 mM 4-MBA (ethanol stock, 200 mM). The mixture was stirred at room temperature overnight at 300 rpm. The AuNSs@4-MBA were centrifuged at 1000 rpm for 5 min at room temperature and redispersed in water. The AuNSs@4-MBA were stored in the dark at 4 °C for future use. Characterizations of the AuNS were performed after the ligand exchange process with 4-MBA.

2.4. Nano-immunosensor architecture

The SPCE was exfoliated in 0.1 M H_2SO_4 by electrochemical oxidation using CV over a potential range of +1.6 to 0 V and a scan rate of 0.1 V/s, until a current of 0.3 mA was reached. AuNSs@4-

MBA were electrochemically deposited on the electrode surface by CV in a potential range of 0 to 1 V at a scan rate of 0.05 V/s for 15 cycles. The nano-immunosensor architecture was designed for the specific detection of CRP using anti-CRP Ab as the biological recognition element. 6 μL of anti-CRP Ab (50 $\mu\text{g}/\text{mL}$) was incubated on AuNSs/*ox*SPCE in a humid chamber at 4 °C overnight. Non-specific adsorption sites on the surface were blocked with 1% BSA on the working electrode for 30 min at room temperature in a humidified chamber. The BSA/anti-CRP/AuNS/*ox*SPCE nanobiocomposite was coated with 6 μL of 1% Nafion™ perfluorinated resin solution for 1 h in a humid chamber at room temperature to improve the platform's stability. After each modification, the electrodes were cleaned with ultrapure water and air-dried at room temperature. 6 μL of known CRP concentrations were incubated on the nano-immunosensor for 1 h in the humid chamber. Before the PEC measurement, the electrode was washed with 1X PBS (pH 7.4) and air-dried at room temperature.

2.5. Electrochemical measurements

The electrochemical characterization of each step in the nano-immunosensor assembly was performed using CV and EIS. The electrode was measured in a 50 μL of 1X PBS (pH 7.4) containing 5 mM $\text{K}_3[\text{Fe}(\text{CN})_6]/\text{K}_4[\text{Fe}(\text{CN})_6]$. CV was initially recorded in a potential range of 0.6 to -0.3 V at a scan rate of 0.05 V/s. The oxidation and reduction properties of the system were utilized to calculate the electroactive area (A_e) using the Randles-Sevcik equation [266]:

$$i_p = 0.4463 nFA_e C \sqrt{\frac{nFvD}{RT}} \quad (\text{Eq. 1})$$

Where i_p is the peak current (A), n is the number of electrons, F is the Faraday's constant (C/mol), A_e is the electroactive area (cm^2), C is the redox probe concentration (mol/cm^3), v is the scan rate (V/s), D is the diffusion coefficient (cm^2/s), R is the gas constant (J/K mol), and T is the temperature (K).

EIS was conducted at 0.125 V of potential with a sinusoidal voltage perturbation of 0.01 V, scanning from 50000 to 0.05 Hz. Impedance spectra were analyzed by fitting equivalent electrical circuits with the software EIS Spectrum Analyzer using the Levenberg-Marquardt algorithm. The surface modification of each step in the nano-immunosensor architecture was estimated by following the change in EIS charge transfer resistance (R_{ct}) according to the equivalent circuit insert in *Figures S10b* and *S11*.

2.6. Photoelectrochemical measurements

The setup for PEC measurements on SPCE couples a PalmSens³ potentiostat and a UV LED Spot Curing System. The photoelectrode surface was illuminated with 765 nm monochromatic light at 48 W/cm². A 1X PBS (pH 7.4) solution containing 0.01 M AA was used as the supporting electrolyte and redox probe. Chronoamperometry was measured for 300 s at a fixed potential of 0 V. Irradiation was turned on after 150 s and left on for 50 s. The area under the curve of the photocurrent signals in the illumination periods was reported as charge. The charge difference of the specific interaction between the Nafion/BSA/anti-CRP/AuNS/*ox*SPCE nano-immunosensor and CRP was used as a parameter for optimizing and evaluating the analytical performance of the device. 6 μ L of the diluted serum sample were incubated on the nano-immunosensor for 1 h in a humid chamber. The CRP concentration was estimated based on the charge difference obtained in the above PEC measurements. All PEC measurements were conducted at room temperature.

2.7. Specificity and selectivity studies

PBS buffer was spiked with CRP at two concentration levels (400 or 25 pg/mL CRP), and several inflammatory biomarkers, including 400 pg/mL PCT, TNF- α , IL-1 β , IL-6, IL-8, IL-10, IL-18, and 100 μ g/mL glucose to study the interferences that can potentially be in real samples. Interferents were individually tested to assess the specificity of the nano-immunosensor, and mixtures of these biomolecules, without and with CRP at the two concentrations, were also analyzed to determine selectivity. As albumin is a major component in blood, the PEC response of the biosensing platform was also interrogated in the presence of a 1:2000 serum, the minimum dilution factor tested with the real samples.

2.8. Human serum samples analysis

The serum samples from subjects with different degrees of inflammation were obtained in a previous study approved by the Ethical Committee of CES University (Medellín, Colombia) (Act 227, 19/07/2023) and - donated by Vidarium, Nutrition, Health, and Wellness Research Center (Medellín, Colombia). In these samples, CRP was quantified using the Human Luminex[®] Discovery Assay (LXSAHM) from R&D Systems in a Luminex MAGPIX CCD imager, as shown *Table S4* and *Figure 11b*. The Ethical Committee of the Sede de Investigación Universitaria from the University of Antioquia (UdeA) approved this project and the use of these samples in Act

number 264 (19/06/2024). The serum samples were diluted at varying factors depending on their CRP concentration, as determined by the Luminex test. The dilution factors used (1:2000, 1:4000, 1:6000, and 1:9000) are detailed in *Table S4*. This approach allowed for matching the concentration levels detected by the nano-immunosensor platform and facilitated the subtraction of the PEC signal associated with these dilutions.

2.9. Statistical analysis

The statistical analysis was conducted using R Studio software to optimize the PEC platform's analytical performance, specificity, selectivity, stability, and signal reproducibility. The data were analyzed using ANOVA (Analysis of Variance), and comparisons between samples were made using the least significant difference (LSD) test with a 95% confidence level. Patient sample evaluation with the Bland-Altman method was used to compare results from the PEC nano-immunosensor and the standard Human Luminex[®] Discovery Assay. This analysis involved plotting the differences between methods (y-axis) against the mean values of the methods (x-axis). The method also defines the limits of agreement, calculated as the mean difference ± 1.96 times the standard deviation, indicating the range within which most differences should fall if no significant bias is present.

3. Results and discussions

In this study, a plasmonic AuNSs/graphene heterojunction was coupled to a red-light PEC system for specific detection of CRP in human serum samples, as shown in *Figure 7*.

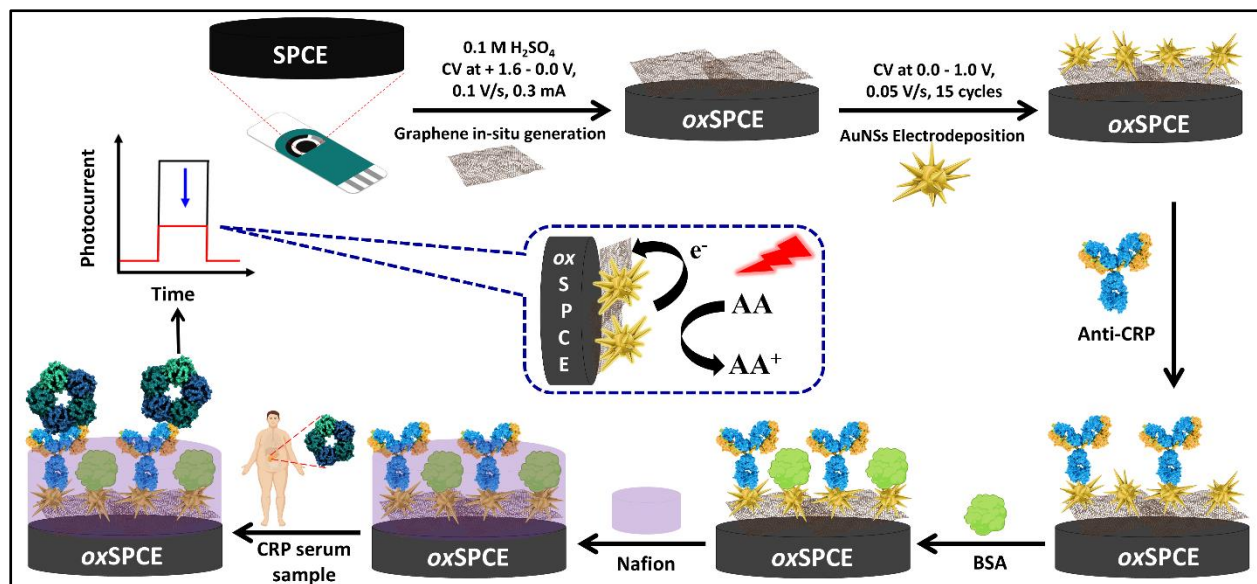


Figure 7. Schematic representation of the modification of SPCE with the Nafion/BSA/anti-CRP/AuNS/oxSPCE nanobiocomposite for CRP detection using photoelectrochemical techniques in a 1X phosphate buffered saline (PBS) solution containing AA as the electron donor in plasmonic-based detection.

Firstly, AuNSs were synthesized using the seed-mediated growth method. Spherical AuNPs were synthesized using the Turkevich method, with sodium citrate (SC) as a reducing and stabilizing agent [265]. The presynthesized Au seeds acted as nucleation points, where sharp tips or branches grew along specific crystallographic directions. The anisotropic growth process involved the reduction of chloroauric acid (HAuCl₄) with AA in the presence of silver ions (Ag⁺) and the surfactant sodium dodecyl sulfate (SDS). In this method, SDS and Ag⁺ are selectively adsorbed on certain facets of the Au seeds, promoting branching with multiple AuNSs' single crystal tips. A key factor in the synthesis included the rapid addition of AA, since slow addition leads to spherical particles [267]. Furthermore, the presence of HCl in the medium facilitated smooth growth within the particle. The AuNSs were surface-modified with 4-mercaptobenzoic acid (4-MBA) to enhance water dispersion stability through an overnight ligand exchange process. This modification serves as a stabilizing agent for plasmonic hotspots while also modulating the LSPR wavelength and intensity [268].

Figures S1a and S1b show the transmission electron microscopy (TEM) images and size distribution histograms for the Au-seeds and AuNSs, respectively. The Au-seeds showed a particle size of 15.4 ± 3.5 nm ($n = 200$), and the resulting soft growth produced AuNSs with a size of 75.7

± 18.9 nm ($n = 200$). The standard deviation of the AuNSs reflected the anisotropy of the nanostructure, as previously reported [269]. Particle size distribution (PSD) for Au-seeds and AuNSs was obtained using dynamic light scattering (DLS), as shown in *Figure S1c*. The Au-seeds (black) display a hydrodynamic size of 38.7 ± 1.3 nm, and the AuNSs (blue) exhibit a size of 155.9 ± 2.4 nm. These sizes reflect the hydrodynamic diameter, which includes the particle core, the solvent layer, and any coating or ligand adsorbed on the nanoparticle surface. The hydrodynamic size may appear larger for non-spherical particles like AuNSs with spikes due to their anisotropic shape, which scatters light differently than spherical particles, potentially altering the measurement [270]. The ζ -potential (*Figure S1d*) for Au-seeds and AuNSs was also measured at -38.7 ± 0.5 mV and -41.3 ± 0.4 mV (pH 6.8), respectively. The negative surface charge of both nanoparticles was attributed to the carboxylate groups of SC and 4-MBA on the Au-seeds and AuNSs, respectively [271]. *Figure S1e* shows the UV-vis absorption spectra of Au-seeds (black) and AuNSs (blue). Au-seeds exhibit a narrow absorption band centered around 520 nm assigned to the surface plasmon resonance of the AuNPs. In contrast, AuNSs exhibit a broad absorption band centered around 765 nm, associated with the surface plasmon resonance of the spherical core with multiple sharp tips of AuNSs [272].

Figure S1f shows the X-ray diffraction (XRD) patterns of the Au-seeds (red), AuNSs (blue), and the theoretical XRD pattern of Au (black) (JCPDS Card No. 04-0784). Crystallographic analysis shows a single phase of the Au nanostructures, consistent with cubic structure with space group $Fm-3m$ (225) and a cell parameter of $a = 4.07 \pm 0.01$ Å [273]. The broadening of the diffraction peaks was attributed to the small crystallite size, while the noise of the XRD patterns was related to the glass substrate in the sample preparation [274]. *Figure S2* shows the high-resolution (HR)-TEM analysis of the Au-seeds and sharp AuNSs tip. The interplanar distance between adjacent Au seed stripes was measured using DigitalMicrograph software, revealing the presence of (111), (200), and (220) planes, consistent with the XRD pattern and theoretical data shown in *Table S1*. D-spacing measured at the AuNS tip was 2.297 ± 0.008 Å, corresponding to the (111) plane. The single-direction crystallization and the absence of crystal defects at the AuNSs tips highlight the plasmonic energy and high light absorption at 765 nm for the generation of photoinduced electrons [275], [276], [277].

The SPCE surface was electrochemically treated in an acidic medium by CV until a maximum current of 0.3 mA was achieved, as shown in *Figure S3a*. *Figure 8a* shows PEC measurements of

oxidized SPCE (*oxSPCE*) by chronoamperometry at 0 V using AA as a redox probe. The photogenerated current was measured by turning on the 765 nm wavelength lamp after 150 s and leaving it on for 50 s. The integration of the area under the photocurrent signal curve during illumination is shown in terms of the electric charge. The initial response's minimal light-off background noise was attributed to thermal effects induced by generating "hot" carriers via LSPR. Bare SPCE and *oxSPCE* exhibited charges of $1.97 \pm 0.38 \mu\text{C}$ and $32.26 \pm 3.23 \mu\text{C}$, respectively. The increased charge of *oxSPCE* compared to bare SPCE confirmed the plasmonic-catalytic effect of edge planes at the graphitic interface and enhanced electron transfer (ET) kinetics. The graphitic interface of the SPCE consists of basal planes parallel to the graphene planes and more active edge planes perpendicular to the surface. These edge-located atoms exhibit higher surface energy due to lower bond coordination. Electrochemical oxidation above +1.0 V in the presence of H_2SO_4 introduced more sp^3 sites, defects, and carbonyl, quinoid, and carboxyl functional groups at the edges of the SPCE planes, as previously reported [278], [279]. The plane edges of the interfacial graphene in *oxSPCE* host confined plasmons with light-matter interactions at a metal-like wavelength of 765 nm [280]. These induced impurities, defects, and grain boundaries in the graphitic edge structure result in enhanced PEC response of *oxSPCEs* by increasing the density of states (DOS) near the Fermi level and ET kinetics in the Faradaic processes [281]. The edge sites on the *oxSPCE* promoted the deposition of presynthesized AuNSs to enhance the PEC response of the interface further. AuNSs were directly electrodeposited onto *oxSPCE* by CV, as shown in *Figure S3b* [282]. The AuNSs/*oxSPCE* nanocomposite charge increased to $56.81 \pm 2.54 \mu\text{C}$ compared to *oxSPCE* ($32.26 \pm 3.23 \mu\text{C}$) due to the plasmonic enhancement of the AuNSs tips. The number of AuNSs electrodeposition scans was optimized by following the charge of photocurrent responses after turning on the red-light irradiation. The highest charge value was achieved after electrodepositing AuNSs on *oxSPCE* for 15 scans, and this charge did not show significant differences with 30 scans (*Figure S3c*). Therefore, 15 scans cover the *oxSPCE* surface with an optimal density of AuNSs on all electrodes used. *Figure S4* shows the optimization of AA concentration to achieve superior PEC performance. The ideal concentration to achieve the highest loading value in PEC measurements for the AuNSs/*oxSPCE* nanocomposite was 0.01 M AA. The platform was tested with on and off red light for 15 consecutive cycles to verify the robustness and stability of the obtained PEC signals, as shown in *Figure S5*. The PEC signal of the AuNSs/*oxSPCE* nanocomposite was stable for up to 10 cycles, with minor variations in the following tests.

Figure 8b shows the characterization of the AuNSs-modified *oxSPCE* by Raman spectroscopy. Two peaks at 1328 cm^{-1} (peak D) and 1567 cm^{-1} (peak G) in the bare *oxSPCE* were associated with edge planes and basal graphene, respectively [283]. G peak was related to the vibration of carbon atoms in an ordered structure with sp^2 hybridization, and the D peak was associated with the presence of defects or impurities in the graphene. Electrochemical exfoliation in an acidic medium enhanced the intensity of the D and G peaks in *oxSPCE*, highlighting the generation of more edge planes in the interfacial graphene. The formation of more reactive sites for ET on the graphene surface of *oxSPCE* was correlated with the increase in the red-light PEC response mentioned above. Furthermore, the electrodeposition of AuNSs was favored by the combination of structural defects, functional groups, high surface energy, and higher DOS at the graphene edge planes in *oxSPCE*. The intensity of the D and G peaks decreased after the electrochemical deposition of AuNSs due to graphene blocking, consequently increasing the PEC response and confirming the successful formation of the photoactive nanocomposite.

Figures 8c and *S6a* show the UV-vis diffuse reflectance spectroscopy (DRS) characterization in terms of the photon energy of the *oxSPCE* to measure the light reflected and scattered from the electrode surface. The reflected light contains information about the optical properties of the material, such as the wide and narrow band gaps, calculated using a Tauc diagram (*Figure S6b*) [284], [285]. The electrochemically generated graphene plane edges at the electrode exhibited light absorption properties over a wide spectral range from UV to infrared regions. The absorption band above 700 nm with a narrow band gap value of 1.52 eV (inset in *Figure 8c*) was attributed to the linear energy dispersion of Dirac fermions from the interfacial graphene. Efficient interactions between red light and graphene were associated with collective oscillations of localized surface plasmons, providing strong light confinement and long lifetimes [254]. These plasmonic properties of interfacial graphene in *oxSPCE* afforded a robust platform for photogenerated charge transfer with low-energy visible light [286]. AuNSs with maximum absorption bands at 765 nm were electrodeposited on *oxSPCE* to maximize the plasmonic properties of the interface. The anisotropic morphology with a central core and multiple sharp tips of the AuNSs generated a strong LSPR with a transition energy of 1.62 eV (*Figure 8d*), consistent with the narrow band gap of graphene in *oxSPCE* [287]. The AuNSs tips with high DOS produced an intense electromagnetic field

enhancement of the "hot spots" [256]. Thus, the AuNSs/graphene heterojunction synergy increased the charge carriers by exciting the system with a 765 nm monochromatic radiation source.

Figure S7a presents the UV-vis spectra of AuNSs with different surface plasmon bands related to increased nanostructure size. The tunable growth of the different AuNSs was obtained by varying the Ag^+ concentration, demonstrating the versatility of the proposed system in absorbing radiation across a wide range of wavelengths [255]. PEC tests on *ox*SPCE modified with AuNSs of different sizes shown in *Figure S7b* confirmed the photocurrent enhancement with AuNSs absorbing at the wavelength (765 nm) like the lamp used as proof of concept in this work. The electron-hole pairs were generated by the oscillating electric fields in the AuNSs/graphene heterojunction under 765 nm red-light irradiation, as illustrated in *Figure 8e*. The LSPR excites oscillations of conduction electrons, generating "hot" electrons injected into the conduction band (CB) of graphene and producing holes in the valence band (VB) due to the favorable band alignment. Plasmonic graphene, with its high electrical conductivity, transports these electrons efficiently to the electrode, while holes generated in the AuNSs are scavenged by ascorbic acid (AA), maintaining charge balance and completing the photocurrent cycle. This AuNS-graphene synergistic plasmonic properties and graphene electron transport capabilities amplify charge separation, minimize recombination, and significantly enhance the PEC signal under red-light irradiation.

The electrochemical performance of the AuNSs/graphene nanocomposite was evaluated by CV monitoring the high current quasi-reversible peaks and changes of the electroactive area (A_e), calculated with the Randles-Sevcik equation (Eq. 1), as shown in *Figure 9a* and summarized in *Table S2* [266]. A reduction in A_e was observed for the *ox*SPCE (11.6 mm^2) compared to 14.5 mm^2 for the bare SPCE, attributed to the formation of graphene edge planes with terminal carboxylic acid groups, as described in the PEC and Raman characterization. The negative charges of these groups, in the presence of the $[\text{Fe}(\text{CN})_6]^{4-/3-}$ redox mediator, cause charge repulsion, reducing the faradaic currents and decreasing the A_e . The increased A_e (15.9 mm^2) of the AuNSs/graphene composite was attributed to the enhanced ET kinetics and higher electrocatalytic activity associated with the large surface area of AuNSs [288].

Figure 9b displays Nyquist plots from the electrochemical impedance spectroscopy (EIS) characterization, where the imaginary part of the impedance ($-Z''$ (Ω)) is plotted against the real part (Z' (Ω)). The impedance spectra were fitted using the Randles equivalent circuit (inset in

Figure 9b). This circuit consists of a solution resistance (R_s) and a charge transfer resistance (R_{ct}) located at the electrode-electrolyte interface. The constant phase element (CPE) modeled a pseudo interfacial double-layer capacitance, representing surface heterogeneities of the electrode, roughness, and adsorption effects. The linear portion at low frequencies corresponded to the Warburg impedance, which described the diffusion of electroactive species toward the electrode [289]. *Table S2* summarizes the data derived from the EIS analysis. The R_{ct} increased from $562.7 \pm 33.9 \Omega$ for SPCE to $753.5 \pm 2.9 \Omega$ for *ox*SPCE due to the hindering of redox probe diffusion caused by the negative charge of the terminal groups at the *ox*SPCE interface. After the electrodeposition of AuNSs, the enhanced ET kinetics decreased the R_{ct} to $299.3 \pm 19.1 \Omega$, consistent with the increase in A_e observed by CV.

by UV-vis spectroscopy. (e) Band diagram at the oxSPCE-AuNSs interface with valence and conduction band energy levels for oxSPCE and AuNSs.

The field-emission scanning electron microscopy (FE-SEM) image of the oxSPCE in *Figure 9c* reveals the typical graphitic carbon morphology of an SPCE electrochemically exfoliated in an acidic medium [266]. *Figure 9d* shows the FE-SEM image of the anisotropic AuNSs deposited on the edge planes of the interfacial graphene, confirming the uniform integration of the PEC system's plasmonic AuNSs/graphene heterojunction [288]. Atomic force microscopy (AFM) images characterized the surface and 3D topography maps of the oxSPCE and AuNSs/oxSPCE nanocomposite, as shown in *Figure S8a–d*. The topography details of the oxSPCE interface were analyzed with the root-mean-square (RMS) value to relate the roughness as a function of height variation across the entire surface [290]. *Figures S8a* and *S8b* showed a homogeneous surface with RMS value of 100.4 ± 5.2 nm. This result is consistent with the FE-SEM images, which reveal holey morphology at the graphitic interface of oxSPCE—including AuNSs on the oxSPCE surface improved the surface homogeneity, as seen in *Figures S8c* and *S8d*. AuNSs formed a dense layer on the interfacial graphene with RMS value of 79.9 ± 4.6 nm, consistent with the Raman and UV-vis spectroscopy, CV, EIS, and FE-SEM analyses. Phase-mode AFM analysis provided additional information about the mechanical properties of the surface. *Figures S8e* and *S8g* show the phase images of the oxSPCE and AuNSs/oxSPCE, along with the cross-sections of the three-dimensional representations of each step. The decrease in RMS value from $2.21 \pm 0.34^\circ$ for oxSPCE to $0.67 \pm 0.07^\circ$ for AuNSs/graphene indirectly indicated the nanostructuring of the interface due to changes in the oscillation frequency of the cantilever [291]. Similarly, the surface potential of oxSPCE and AuNSs/oxSPCE was evaluated via Kelvin probe force microscopy (KPFM), as shown in *Figures S8i–l* [292]. In KPFM, the contact potential difference (CPD) between the AFM tip and the sample surface was measured by applying a compensation voltage [293]. The potential map obtained by KPFM showed a decrease in CPD in oxSPCE (1.46 ± 0.26 mV) compared to the AuNSs/oxSPCE nanocomposite with a CPD of 0.75 ± 0.13 mV. The reduction of CPD was attributed to the homogeneous deposition of small-sized AuNSs on oxSPCE and the strong electronic interactions between the AuNSs and interfacial graphene [294], [295].

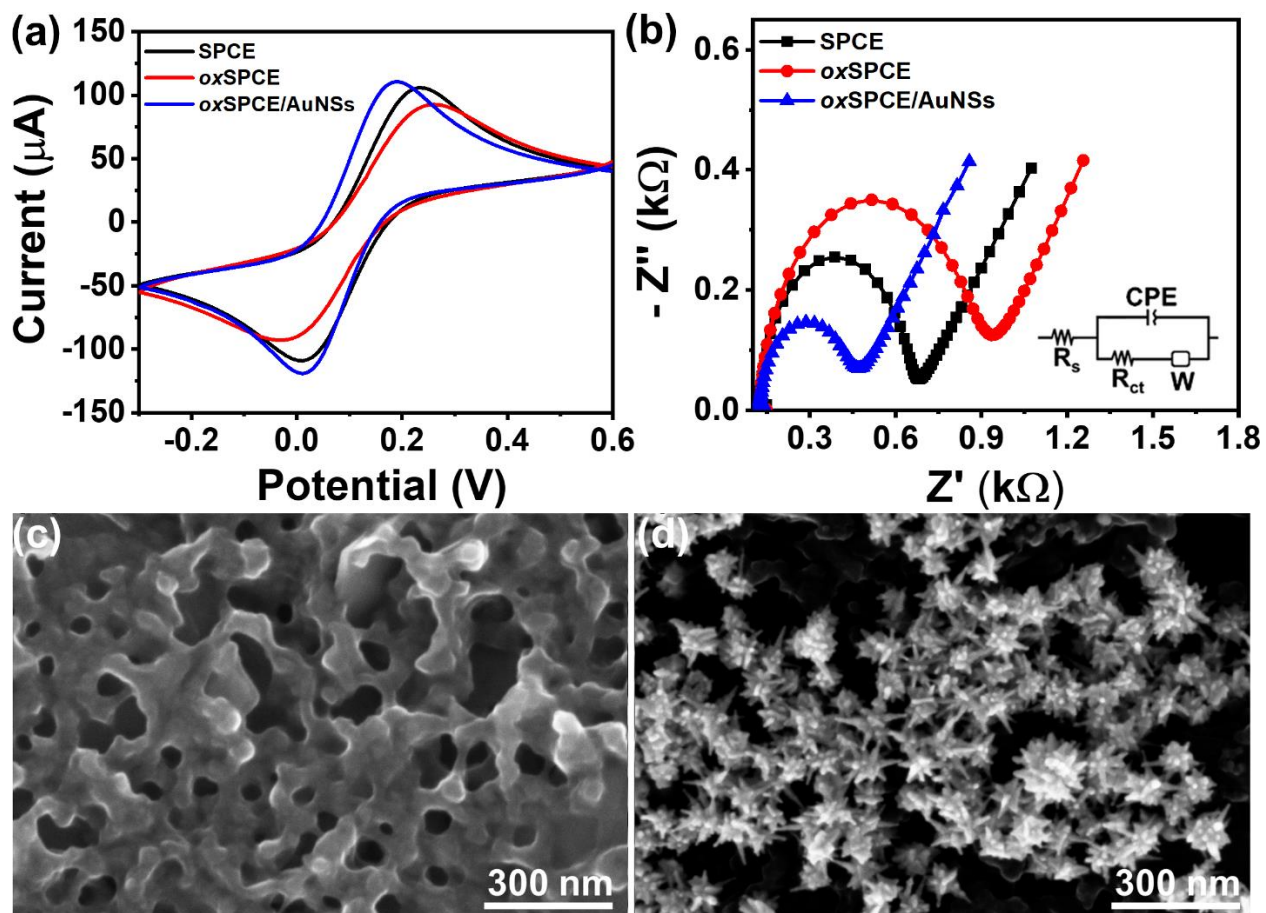


Figure 9. (a) CV of the modified AuNSs/oxSPCE electrode in a 1X PBS (pH 7.4) solution containing 5 mM $[\text{Fe}(\text{CN})_6]^{4-/3-}$ as the redox mediator at 0.05 V/s, and (b) EIS from 50000 to 0.05 Hz, at the formal potential of 0.125 V, and amplitude 0.01 V. (c) FE-SEM images of the oxSPCE, and (d) AuNSs/oxSPCE electrodes, respectively.

PEC, CV, and EIS confirmed the effective assembly of the nano-immunosensor and the detection of CRP. The PEC responses regarding the step-by-step charge of the nano-immunosensor assembly are presented in Figure 10a. The charge of the system in the red-light irradiation region was decreased from $56.81 \pm 2.54 \mu\text{C}$ for the AuNSs/oxSPCE nanocomposite to $19.52 \pm 1.33 \mu\text{C}$ after electrostatic immobilization of the anti-CRP antibody (Ab) overnight. The charge decreased to $4.52 \pm 0.34 \mu\text{C}$ by blocking the non-specific absorption sites with bovine serum albumin (BSA). The charge reduction was attributed to the steric effects of biomolecules on the electrode surface, which impeded the diffusion of the electron donor to the electrode [4]. The BSA/Anti-CRP/AuNSs/oxSPCE bio-interface was coated with Nafion to improve the stability and PEC performance of the nano-immunosensor. The diffusion of the electroactive species at the interface

was amplified by the excellent ionic conductivity of Nafion, increasing the charge up to $145.36 \pm 2.54 \mu\text{C}$. *Figure S9* demonstrates the synergy of Nafion to the PEC response of the plasmonic platform. The ionic conduction properties of Nafion combined with the high ET of the BSA/Anti-CRP/AuNSs/oxSPCE nanobiocomposite under irradiation at 765 nm accelerated the AA oxidation kinetics. The PEC response of the Nafion-modified SPCE without the nanobiocomposite, as shown in *Figure S9a*, exhibited a charge of $32.5 \pm 1.27 \mu\text{C}$, highlighting the individual contributions of the system's components. Similarly, *Figure S9b* demonstrates the combined activity of graphene edge planes and the Nafion membrane, with a charge of $57.7 \pm 3.63 \mu\text{C}$. Furthermore, *Figure S9c* shows that the fully assembled AuNS/graphene nanocomposite charge reached $182.35 \pm 6.33 \mu\text{C}$, contrasting with the fully assembled nano-immunosensor in *Figure S9d*. Plasmonic heterojunction and Nafion membrane in PEC systems enhance charge transfer and ion diffusion at the interface by facilitating the movement of positively charged species through their cation-permeable channels [296]. In addition, Nafion stabilizes photoactive components, maintains the integrity of the electrochemical assembly, and optimizes system performance by preventing signal loss [297]. The decrease of the charge to $34.31 \pm 2.47 \mu\text{C}$ was correlated with the PEC detection of 0.8 ng/mL of CRP on the nano-immunosensor. The transfer of photoinduced electrons to the electrode surface was hindered by the steric effect of the pentameric CRP coupled to the anti-CRP Abs of the nano-immunosensor.

The complete assembly of nano-immunosensor was confirmed by CV and EIS analysis, as shown in *Figures S10a* and *S10b* and summarized in *Table S2*. *Figure S10a* shows the decrease in A_e of the AuNSs/oxSPCE nanocomposite (15.9 mm^2) to 13.4 mm^2 after adsorption of anti-CRP Ab due to the impeded ET in the electrode-electrolyte interface. The free sites of the interface not coated with anti-CRP Ab were blocked with BSA, and the A_e was reduced to 11.1 mm^2 . However, when the Nafion membrane coated the platform, the A_e was increased to 13.6 mm^2 due to improved ionic conductivity. The 0.8 ng/mL CRP detection on the plasmonic nano-immunosensor decreased A_e to 11.8 mm^2 , contrasting PEC detection with red light. The EIS characterization by evaluating the equivalent circuits derived from Nyquist plots of the CRP nano-immunosensor is shown in *Figure S10b*. The R_{ct} value was increased to $723.9 \pm 24.3 \Omega$ and $1039.3 \pm 25.2 \Omega$ with the successive electrostatic immobilization of anti-CRP Ab and BSA on the AuNSs/oxSPCE nanocomposite, respectively, consistent with the PEC and CV results. The addition of the Nafion membrane resolved two additional components of R_{ct} and CPE in the EIS spectra associated with the

BSA/Anti-CRP/AuNSs/oxSPCE bio-interface and Nafion film (*Figures S11a*). Nafion provided redox probe mobility and improved electrochemical equilibrium by decreasing the R_{ct} to $417.6 \pm 12.2 \Omega$. The increase in R_{ct} up to $512.6 \pm 5.8 \Omega$ was correlated with the antigen-antibody biochemical interaction of CRP detection (0.8 ng/mL), which limited the efficiency of oxidation-reduction reactions between the mediator and the interface (*Figure S11b*) [266]. *Figure S12* shows CVs at different scan rates (0.025-0.25 V/s) to elucidate the electron transfer mechanism of the redox probe $[\text{Fe}(\text{CN})_6]^{3-/4-}$ at the modified SPCE interfaces. The maximum redox currents (I_p) exhibited a linear increase with the scan rate, and the ratio between anodic and cathodic currents (I_{pa}/I_{pc}) was 0.99, 1.00, 0.96, and 1.00 for bare SPCE, oxSPCE, AuNSs/oxSPCE, and Nafion/BSA/Anti-CRP/AuNSs/oxSPCE nano-immunosensor, respectively. The CV results suggested a quasi-reversible behavior of the electrochemical reactions at all electrode surfaces [298]. The linear relationship between peak currents and the square root of the scan rate, with regression coefficients (R^2) above 0.98, confirmed that the redox processes are diffusion-controlled at all interfaces.

The experimental conditions of nano-immunosensor assembly were optimized to detect 0.8 ng/mL of CRP with the highest PEC performance. The highest ΔCharge ($113.45 \pm 1.95 \mu\text{C}$) was achieved with a concentration of $50 \mu\text{g/mL}$ of anti-CRP Ab, as shown in *Figures S13a* and *S13b*. Similarly, incubation of the anti-CRP Ab overnight (12 h) showed the most significant ΔCharge detection with optimal coating of the AuNSs/oxSPCE surface (*Figures S13c* and *S13d*). The nano-immunosensor revealed a higher PEC response by adding 1% Nafion solution (*Figures S13e* and *S13f*). Finally, *Figures S13g* and *S13h* showed optimal CRP detection in only 60 min.

The optimized PEC nano-immunosensor was CRP concentration-dependent. A decrease in photocurrent intensity was related to the progressive increase in CRP concentration attributed to the large size of the pentameric protein that blocked photoinduced ET. The time-photocurrent curves for different CRP concentrations are represented in the 3D plot of *Figure 10b*. The photocurrent signal was inversely correlated with CRP concentration from 0.025 to 0.8 ng/mL. The calibration curve shown in *Figure 10c* describes the ΔCharge versus CRP concentration with a linear regression equation of $\Delta\text{Charge} (\mu\text{C}) = 111.4 \mu\text{C mL ng}^{-1} [\text{CRP}] + 29.6 \mu\text{C}$, an $R^2 = 0.996$. The limit of detection (LOD) and the limit of quantification (LOQ) were 13.3 pg/mL and 44.3 pg/mL, respectively. *Table S3* compares the analytical performance of nanostructured platforms based on PEC biosensors for CRP detection with the methodology implemented in this study.

While the LODs obtained in the current work are slightly higher than those reported by other authors, red-light radiation at 765 nm offers distinct advantages over platforms utilizing shorter wavelengths. For example, Hu et al [222] employed 414 nm light, achieving an LOD of 0.1 ng/mL, while Xia et al [225] used 365-370 nm light and reached an LOD of 3.33 pg/mL. In contrast, the platform developed in this work achieved an LOD of 13.3 pg/mL but with red-light radiation. This longer wavelength is expected to reduce photodamage and enhance charge transfer efficiency, critical for improving PEC signal response in biological systems. Furthermore, red or near-infrared light allows for noninvasive detection, making it more suitable for clinical applications, particularly when compared to UV-visible wavelengths prone to inducing biomolecular degradation. Therefore, the red-light platform presents significant benefits in terms of safety and long-term stability, demonstrating its potential for use in clinical settings.

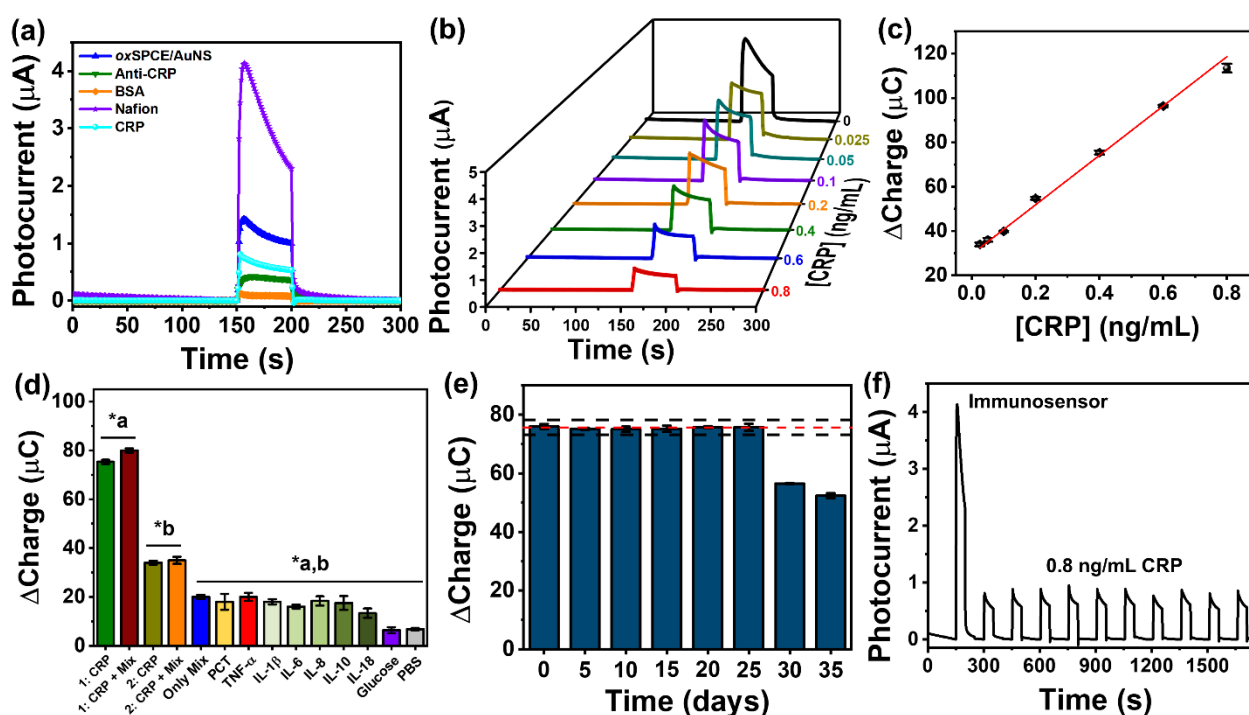


Figure 10. (a) Step-by-step PEC response of the nano-immunosensor architecture in a 1X PBS (pH 7.4) solution containing 0.01 MAA as the electron donor. (b) Amperometric signals were acquired at 0 V from the label-free PEC nano-immunosensor at varying CRP concentrations. (c) Linear regression curve of ΔCharge against different CRP concentrations ($n = 3$). (d) Specificity and selectivity test of the nano-immunosensor with 400 pg/mL of interfering biomolecules without and with two concentrations of CRP (1: 400 and 2: 25 pg/mL). *Indicates significant differences with $p < 0.05$ for all interferents and the negative control. (e) Time stability study of the nano-immunosensor for detecting 400 pg/mL CRP. (f) Time-based PEC responses of the biosensor stability test over 10 on and off light cycles.

Several inflammatory biomarkers, including procalcitonin (PCT), tumor necrosis factor- α (TNF- α), interleukin-1 β (IL-1 β), interleukin-6 (IL-6), interleukin-8 (IL-8), interleukin-10 (IL-10), interleukin-18 (IL-18); and glucose (100 μ g/mL), were individually tested at 400 pg/mL to assess the specificity of the CRP nano-immunosensor. Mixtures of these biomolecules, without and with CRP at two concentrations (400 and 25 pg/mL), were also analyzed to determine selectivity (*Figure 10d*). The PEC response of the biosensing platform was also interrogated in the presence of a 1:2000 serum, the minimum dilution factor tested with the real samples showing no cross-reactivity. The nano-immunosensor showed a higher Δ Charge for CRP detection than interferents, with statistically significant differences ($p < 0.05$). The presence of interfering molecules did not affect the nano-immunosensor's response, demonstrating high selectivity and specificity for CRP detection.

As shown in *Figure 10e*, the stability of the CRP detection platform was monitored by comparing triplicate measurements of 400 pg/mL CRP over time, using the first day's measurement ($75.65 \pm 0.85 \mu$ C) as a reference. Stability was assessed with control limits three times the baseline standard deviation (3 SD) [299]. After 25 days, a significant decline in the detection signal was observed, likely due to degradation of the anti-CRP Ab bioconjugate. Before this period, signals remained stable within the statistically defined range. Photocurrent response tests in *Figure 10f* confirmed constant signal output with an RSD of 3.54 % with periodic light switching over ten cycles. Additionally, tests on ten different nano-immunosensing interfaces yielded an RSD of 3.1 %, indicating consistent inter-platform performance (*Figure S14*).

PEC nano-immunosensors based on AuNSs/oxSPCE with an enhanced LSPR effect were evaluated for accuracy and stability using serum samples from patients with different levels of inflammation. CRP quantification is critical for these patients because it is an inflammatory biomarker linked to cardiovascular diseases and metabolic complications. Elevated CRP levels reflect chronic low-grade inflammation related to a persistent state of inflammation without noticeable symptoms, which increases the risk of atherosclerosis, hypertension, type 2 diabetes, and cardiovascular events [300], [301]. For experimental analysis, ten clinical test samples were compared with diluted human serum, following the dilution factor shown in *Figure 11a*. Accuracy and stability were assessed using the same PEC nano-immunosensor strategy. Sample sets were categorized by CRP concentration into low (S.1 and S.2), medium (S.3 to S.6), and high (S.7 to S.10) levels. CRP concentration was calculated based on the " Δ charge" obtained during assembly and measurement,

using the linear equation: $[\text{sample}] = (\Delta\text{charge} - 29.6) / 111.4 \mu\text{C}$. Relative errors in CRP quantification decreased as the CRP concentration increased, likely due to the matrix effect and the presence of other proteins in the serum. Interfering proteins and instability of biological reagents were identified as factors affecting the precision of PEC nano-immunosensor. The results of the PEC nano-immunosensor were correlated with those obtained from the standard Human Luminex[®] Discovery Assay for CRP quantification, as shown in *Figure 11b*. A paired *t*-test with a 95% confidence level (p -value = 0.32) revealed no statistically significant difference between the two methods, and a value of $R^2 = 0.995$ showed a high linearity and a strong correlation between the two methodologies.

Additionally, the high reliability and performance of the PEC nano-immunosensor for determining CRP in real samples was confirmed by Bland-Altman analysis (*Figure S15*). A high level of agreement between the methods was observed, without systematic bias, as the average differences did not deviate significantly from zero and were within the “limits of agreement” [302]. The quantification of CRP, a key biomarker in a clinically relevant infectious biomarker panel, using nano-immunosensing methodologies with disposable electrochemical cells and plasmonic nanomaterials in PEC assays activated by noninvasive red radiation, highlights a promising strategy for personalized medicine. This approach enables more accurate diagnosis, treatment selection, and disease monitoring based on individual patient characteristics.

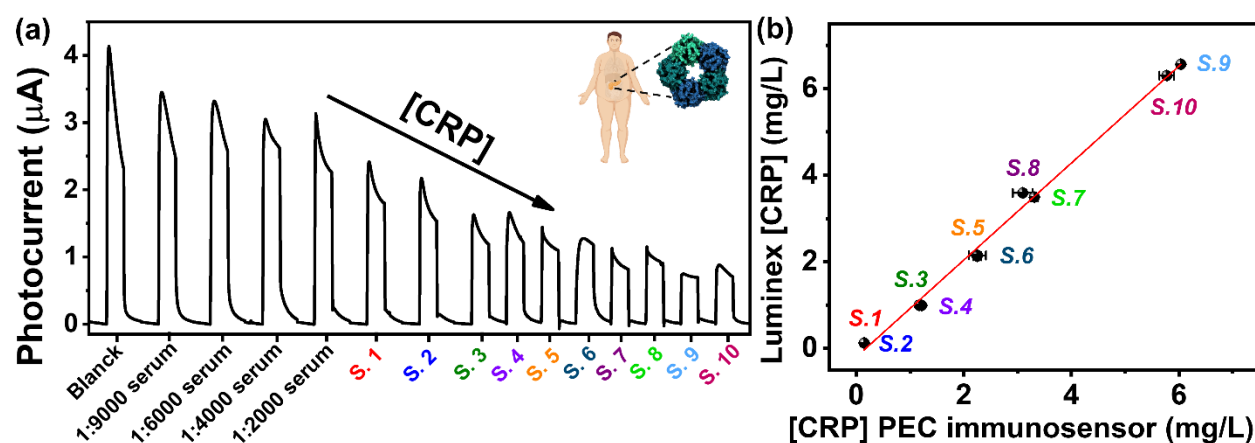


Figure 11. (a) PEC response of the nano-immunosensor in a 1X PBS (pH 7.4) solution containing 0.01 M AA as the electron donor across various serum samples from patients with different levels of inflammation. (b) Comparison between the results obtained from the PEC nano-immunosensor and standard Human Luminex[®] Discovery Assay for CRP detection in serum samples from patients with different levels of inflammation. Error bars represent three times the standard deviation ($n = 3$).

4. Conclusions

A plasmonic-based PEC nano-immunosensor was developed on a disposable miniaturized electrochemical cell for sensitively detecting CRP, a relevant biomarker for inflammatory disorders. Unlike conventional PEC nanobiosensors, this device benefited from the plasmonic effect of in situ-generated graphene plane edges on SPCE and the LSPR of custom-designed AuNSs for activation under red-light irradiation. These features improved electron-hole pair separation and enhanced the PEC response. Integrating PEC nano-immunosensing methodologies efficiently converted biochemical affinity interactions into charge responses with low-background noise and tailored to low-energy wavelengths suitable for noninvasive point-of-care monitoring. As a result, the PEC nano-immunosensor exhibited high sensitivity and stability over time for detecting CRP from patients with different levels of inflammatory response. This approach would favor a precise diagnosis and personalized treatment planning. Furthermore, the designed red-light PEC detection device offers a fast readout, automated, and selective detection approach for inflammatory disorders and other diseases.

5. Acknowledgments

The authors acknowledge MinCiencias for funding the project Validation of a Nanobiosensor to detect SARS-CoV-2 rapidly (Cod. 111593092980). Dr. Katalina Muñoz Durango and Dr Jelver Sierra from Vidarium, Nutrition, Health, and Wellness Research Center from Medellín, Colombia, kindly donated serum samples and data on inflammation. The authors acknowledge Centro de Investigación, Innovación y Desarrollo de Materiales – CIDEMAT (UdeA) for the AFM measurements. J.O. acknowledges financial support from the Minciencias, the University of Antioquia, and the Max Planck Society through the Cooperation Agreement 566-1, 2014. We thank The Ruta N complex and EPM for hosting the Max Planck Tandem Groups.

CHAPTER IV: Conclusions and Perspectives

Conclusions

The development of red light-based PEC biosensors from this work offers a significant advance in clinical diagnostics, providing highly sensitive and specific biomarker detection through enhanced photoelectric conversion efficiency using the LSPR effect of AuNSs with in-situ generated graphene. Utilizing 765 nm red light minimizes photodamage and biological interference, making these biosensors ideal for noninvasive, real-time diagnostics. Their scalability, portability, and adaptability for detecting various biomarkers make them suitable for POC diagnostics and personalized medicine, enabling rapid, accurate, and low-cost detection, thus improving patient outcomes and reducing healthcare costs.

Developing a PEC nano-immunosensor based on the heterojunction of AuNSs and graphene demonstrated the ability to harness red light (765 nm) efficiently, achieving high photoelectrical conversion effectiveness. This design reduced photodamage and interference from biological samples, providing a non-invasive, scalable, and highly sensitive platform for biomarker detection, especially in clinical diagnostics of inflammatory disorders. The proposed PEC platform enables effective charge separation and signal amplification by combining nanostructured plasmonic materials and graphene, resulting in robust and consistent performance across multiple real clinical samples. This capability proved essential for monitoring biomarkers such as CRP in various conditions, particularly inflammation-related diseases, offering a precise, selective, and automated tool for healthcare applications.

The analytical performance of the PEC platform for CRP detection was characterized by a linear detection range of 25–800 pg/mL and a LOD of 13.3 pg/mL. The optimization of the nanostructured photoactive transduction system demonstrated high sensitivity and specificity in real clinical samples, making it a promising tool for early detection, monitoring, and management of inflammatory conditions. This strategy showed the potential of PEC biosensors as a reliable alternative to conventional methods, offering rapid response, low background noise, and high reproducibility in biomarker analysis.

The miniaturization of PEC biosensors, such as those based on disposable SPCEs modified with AuNSs, represents a significant advancement in POC diagnostic tools. These platforms hold great

potential for multi-analyte detection, crucial for patient-specific diagnostics and personalized medicine. By integrating these biosensors with emerging technologies like AI, machine learning, and the IoT, PEC platforms could revolutionize disease diagnosis and monitoring, offering real-time, automated, and precise solutions in healthcare.

Perspectives

Integrating red- and NIR-light into PEC plasmonic nanomaterial-based sensing systems represents a significant leap in noninvasive POC diagnostics. By activating PEC systems with red and NIR light, the sensitivity and background signal of biomarker detection are significantly improved, offering promising solutions for clinical diagnostics. The lower energy of NIR radiation compared to UV light minimizes the photodamage often suffered by biomolecules, such as antibodies, proteins, and enzymes, preserving their structural integrity and extending the stability of the biosensing platform. This feature, combined with the high surface area and plasmonic activity of Au and graphene nanomaterials, ensures efficient charge separation and signal amplification, crucial for detecting low-concentration biomarkers like CRP.

As POC diagnostic tools, these biosensors can provide rapid, accurate results close to the patient or in remote locations, reducing the reliance on centralized laboratories and the delays associated with data analysis. Decentralized diagnostic technologies align with the growing demand for personalized medicine, where timely detection and monitoring of disease biomarkers enable tailored treatment strategies, improving patient outcomes and reducing healthcare costs. By integrating these biosensors with emerging technologies like AI, machine learning, and the IoT, nanobiosensors can gain advanced analytical capabilities, real-time data processing, and predictive diagnostics, enhancing their impact on modern healthcare.

Additionally, integrating these PEC biosensors into pocket potentiostats offers a practical pathway to create compact systems capable of transmitting results through portable electronic and communication devices, such as smartphones and tablets, during POC measurements. This portability enables the deployment of biosensors in resource-limited settings, making them

accessible for large-scale public health applications and supporting early disease detection for conditions such as infectious diseases, cancer, and metabolic disorders.

Future research efforts should focus on refining the biointerfaces of these PEC systems, enhancing the selectivity and specificity for various biomarkers, and conducting clinical validation through large-scale studies. The continued development of these technologies, coupled with advancements in materials engineering, nanoengineering, and portable electronic integration, will pave the way for more robust and reliable POC diagnostic devices that can address the challenges of modern healthcare systems.

REFERENCES

- [1] A. Childs, B. Mayol, J. A. Lasalde-Ramírez, Y. Song, J. R. Sempionatto, and W. Gao, “Diving into Sweat: Advances, Challenges, and Future Directions in Wearable Sweat Sensing,” *ACS Nano*, 2024, doi: 10.1021/acsnano.4c10344.
- [2] X. Zhang, Y. Guo, M. Liu, and S. Zhang, “Photoelectrochemically active species and photoelectrochemical biosensors,” 2013. doi: 10.1039/c2ra22238h.
- [3] Y. Monsalve, A. F. Cruz-Pacheco, and P. Jahir, “Red and near - infrared light - activated photoelectrochemical nanobiosensors for biomedical target detection,” *Microchimica Acta*, 2024, doi: 10.1007/s00604-024-06592-x.
- [4] R. Li, R. Yan, J. Bao, W. Tu, and Z. Dai, “A localized surface plasmon resonance-enhanced photoelectrochemical biosensing strategy for highly sensitive and scatheless cell assay under red light excitation,” *Chemical Communications*, vol. 52, no. 79, pp. 11799–11802, 2016, doi: 10.1039/c6cc05964c.
- [5] W. Ansar and S. Ghosh, “Inflammation and Inflammatory Diseases, Markers, and Mediators: Role of CRP in Some Inflammatory Diseases BT - Biology of C Reactive Protein in Health and Disease,” W. Ansar and S. Ghosh, Eds., New Delhi: Springer India, 2016, pp. 67–107. doi: 10.1007/978-81-322-2680-2_4.
- [6] J. Quinchia, D. Echeverri, A. F. Cruz-Pacheco, M. E. Maldonado, and J. A. Orozco, “Electrochemical biosensors for determination of colorectal tumor biomarkers,” *Micromachines (Basel)*, vol. 11, no. 4, pp. 1–46, 2020, doi: 10.3390/MII1040411.
- [7] V. Vásquez and J. Orozco, “Detection of COVID-19-related biomarkers by electrochemical biosensors and potential for diagnosis, prognosis, and prediction of the course of the disease in the context of personalized medicine,” *Anal Bioanal Chem*, vol. 415, no. 6, pp. 1003–1031, 2023, doi: 10.1007/s00216-022-04237-7.
- [8] S. Cajigas and J. Orozco, “Nanobioconjugates for signal amplification in electrochemical biosensing,” *Molecules*, vol. 25, no. 15, pp. 11–16, 2020, doi: 10.3390/molecules25153542.
- [9] S. Patel, R. Nanda, S. Sahoo, and E. Mohapatra, “Biosensors in Health Care: The Milestones Achieved in Their Development towards Lab-on-Chip-Analysis,” *Biochem Res Int*, vol. 2016, pp. 1–12, Mar. 2016, doi: 10.1155/2016/3130469.

- [10] F. Bettazzi and I. Palchetti, "Photoelectrochemical genosensors for the determination of nucleic acid cancer biomarkers," *Curr Opin Electrochem*, vol. 12, pp. 51–59, 2018, doi: 10.1016/j.coelec.2018.07.001.
- [11] J. Shu and D. Tang, "Recent Advances in Photoelectrochemical Sensing: From Engineered Photoactive Materials to Sensing Devices and Detection Modes," *Anal Chem*, vol. 92, no. 1, pp. 363–377, 2020, doi: 10.1021/acs.analchem.9b04199.
- [12] Y. Zang, J. Fan, Y. Ju, H. Xue, and H. Pang, "Current Advances in Semiconductor Nanomaterial-Based Photoelectrochemical Biosensing," *Chemistry - A European Journal*, pp. 14010–14027, 2018, doi: 10.1002/chem.201801358.
- [13] E. Costa-Rama and M. Teresa Fernández-Abedul, "Paper-Based Screen-Printed Electrodes: A New Generation of Low-Cost Electroanalytical Platforms †," *Biosensors (Basel)*, vol. 11, pp. 11–43, 2021, doi: 10.3390/bios11020051.
- [14] C. Zhu, G. Yang, H. Li, D. Du, and Y. Lin, "Electrochemical sensors and biosensors based on nanomaterials and nanostructures," *Anal Chem*, vol. 87, no. 1, pp. 230–249, 2015, doi: 10.1021/ac5039863.
- [15] Y. Zhang, E. Villarreal, G. G. Li, W. Wang, and H. Wang, "Plasmonic Nanozymes: Engineered Gold Nanoparticles Exhibit Tunable Plasmon-Enhanced Peroxidase-Mimicking Activity," *Journal of Physical Chemistry Letters*, vol. 11, no. 21, pp. 9321–9328, 2020, doi: 10.1021/acs.jpcclett.0c02640.
- [16] E. Ruggiero, S. Alonso-De Castro, A. Habtemariam, and L. Salassa, "Upconverting nanoparticles for the near infrared photoactivation of transition metal complexes: New opportunities and challenges in medicinal inorganic photochemistry," *Dalton Transactions*, vol. 45, no. 33, pp. 13012–13020, 2016, doi: 10.1039/c6dt01428c.
- [17] P. Miao *et al.*, "Near-infrared light-induced photoelectrochemical biosensor based on plasmon-enhanced upconversion nanocomposites for microRNA-155 detection with cascade amplifications," *Biosens Bioelectron*, vol. 226, 2023, doi: 10.1016/j.bios.2023.115145.
- [18] L. Nan *et al.*, "Investigating Plasmonic Catalysis Kinetics on Hot-Spot Engineered Nanoantennae," *Nano Lett*, 2023, doi: 10.1021/acs.nanolett.3c00219.
- [19] A. Pathak and A. Agrawal, "Evolution of C-reactive protein," *Front Immunol*, vol. 10, no. APR, 2019, doi: 10.3389/fimmu.2019.00943.

- [20] L. M. L. Maria Soler, Olalla Calvo-Lozano, M.-Carmen Estevez, “Nanophotonic Biosensors,” *Opt Photonics News*, vol. 31, no. April, pp. 24–31, 2020.
- [21] N. M. Ngo, H. V. Tran, and T. R. Lee, “Plasmonic Nanostars: Systematic Review of their Synthesis and Applications,” *ACS Appl Nano Mater*, vol. 5, no. 10, pp. 14051–14091, 2022, doi: 10.1021/acsnm.2c02533.
- [22] A. Gill, Z. Nate, R. Chauhan, M. Faya, R. Karpoormath, and C. A. Omolo, *Nanobioengineering: A promising approach for early detection of COVID-19*, First Edit. Elsevier Ltd., 2022. doi: 10.1016/B978-0-323-90280-9.00004-3.
- [23] W. Tu, Z. Wang, and Z. Dai, *Selective photoelectrochemical architectures for biosensing: Design, mechanism and responsibility*, vol. 105. TrAC - Trends in Analytical Chemistry, 2018. doi: 10.1016/j.trac.2018.06.007.
- [24] X. Huang, Y. Zhu, and E. Kianfar, “Nano Biosensors: Properties, applications and electrochemical techniques,” *Journal of Materials Research and Technology*, vol. 12, pp. 1649–1672, 2021, doi: 10.1016/j.jmrt.2021.03.048.
- [25] P. Malik, V. Katyal, V. Malik, A. Asatkar, G. Inwati, and T. K. Mukherjee, “Nanobiosensors: Concepts and Variations,” *Int Sch Res Notices*, vol. 2013, 2013, doi: 10.1155/2013/327435.
- [26] J. Orozco, C. Jiménez-Jorquera, and C. Fernández-Sánchez, “Gold nanoparticle-modified ultramicroelectrode arrays for biosensing: A comparative assessment,” *Bioelectrochemistry*, vol. 75, no. 2, pp. 176–181, 2009, doi: 10.1016/j.bioelechem.2009.03.013.
- [27] D. Alzate, S. Cajigas, S. Robledo, C. Muskus, and J. Orozco, “Genosensors for differential detection of Zika virus,” *Talanta*, vol. 210, no. October 2019, p. 120648, 2020, doi: 10.1016/j.talanta.2019.120648.
- [28] G. Vásquez, A. Rey, C. Rivera, C. Iregui, and J. Orozco, “Amperometric biosensor based on a single antibody of dual function for rapid detection of *Streptococcus agalactiae*,” *Biosens Bioelectron*, vol. 87, pp. 453–458, 2017, doi: 10.1016/j.bios.2016.08.082.
- [29] S. Saha, A. Victorious, R. Pandey, A. Clifford, I. Zhitomirsky, and L. Soleymani, “Differential photoelectrochemical biosensing using DNA nanospacers to modulate electron transfer between metal and semiconductor nanoparticles,” *ACS Appl Mater Interfaces*, vol. 12, no. 33, pp. 36895–36905, 2020, doi: 10.1021/acsaami.0c09443.

- [30] J. Orozco, "Nanoscience, nanotechnology, and disruptive technologies in the context of precision medicine," *Rev Acad Colomb Cienc Exactas Fis Nat*, vol. 47, no. 183, pp. 221–241, 2023, doi: 10.18257/raccefyn.1895.
- [31] D. Echeverri, E. Calucho, J. Marrugo-Ramírez, R. Álvarez-Diduk, J. Orozco, and A. Merkoçi, "Capacitive immunosensing at gold nanoparticle-decorated reduced graphene oxide electrodes fabricated by one-step laser nanostructuring," *Biosens Bioelectron*, vol. 252, no. February, 2024, doi: 10.1016/j.bios.2024.116142.
- [32] A. F. Cruz-Pacheco, D. Echeverri, and J. Orozco, "Role of electrochemical nanobiosensors in colorectal cancer precision medicine," *TrAC - Trends in Analytical Chemistry*, vol. 170, no. September 2023, 2024, doi: 10.1016/j.trac.2023.117467.
- [33] W. W. Zhao, J. J. Xu, and H. Y. Chen, "Photoelectrochemical bioanalysis: The state of the art," *Chem Soc Rev*, vol. 44, no. 3, pp. 729–741, 2015, doi: 10.1039/c4cs00228h.
- [34] S. Liu, C. Li, J. Cheng, and Y. Zhou, "Selective photoelectrochemical detection of DNA with high-affinity metallointercalator and tin oxide nanoparticle electrode," *Anal Chem*, vol. 78, no. 13, pp. 4722–4726, 2006, doi: 10.1021/ac052022f.
- [35] D. Dong *et al.*, "Quantitative Photoelectrochemical Detection of Biological Affinity Reaction: Biotin-Avidin Interaction," *Anal Chem*, vol. 76, no. 2, pp. 499–501, 2004, doi: 10.1021/ac035184p.
- [36] X. Zhang, Y. Zhao, S. Li, and S. Zhang, "Photoelectrochemical biosensor for detection of adenosine triphosphate in the extracts of cancer cells," *Chemical Communications*, vol. 46, no. 48, pp. 9173–9175, 2010, doi: 10.1039/c0cc03595e.
- [37] Y. Tan, Y. Wang, M. Li, X. Ye, T. Wu, and C. Li, "Enhanced photoelectrochemical immunosensing of cardiac troponin I based on energy transfer between N-acetyl-L-cysteine capped CdAgTe quantum dots and dodecahedral Au nanoparticles," *Biosens Bioelectron*, vol. 91, no. January, pp. 741–746, 2017, doi: 10.1016/j.bios.2017.01.040.
- [38] Y. T. Long, C. Kong, D. W. Li, Y. Li, S. Chowdhury, and H. Tian, "Ultrasensitive determination of cysteine based on the photocurrent of nafion-functionalized CdS-MV quantum dots on an ITO electrode," *Small*, vol. 7, no. 12, pp. 1624–1628, 2011, doi: 10.1002/sml.201100427.
- [39] H. Wang *et al.*, "A sensitive photoelectrochemical immunoassay of N6-methyladenosine based on dual-signal amplification strategy: Ru doped in SiO₂ nanosphere and carboxylated

- g-C₃N₄,” *Biosens Bioelectron*, vol. 99, no. July 2017, pp. 281–288, 2018, doi: 10.1016/j.bios.2017.07.042.
- [40] C. Li, H. Wang, J. Shen, and B. Tang, “Cyclometalated iridium complex-based label-free photoelectrochemical biosensor for dna detection by hybridization chain reaction amplification,” *Anal Chem*, vol. 87, no. 8, pp. 4283–4291, 2015, doi: 10.1021/ac5047032.
- [41] Z. Qiu and D. Tang, “Nanostructure-based photoelectrochemical sensing platforms for biomedical applications,” *J Mater Chem B*, vol. 8, no. 13, pp. 2541–2561, 2020, doi: 10.1039/c9tb02844g.
- [42] K. Zhang, S. Lv, Z. Lin, M. Li, and D. Tang, “Bio-bar-code-based photoelectrochemical immunoassay for sensitive detection of prostate-specific antigen using rolling circle amplification and enzymatic biocatalytic precipitation,” *Biosens Bioelectron*, vol. 101, no. September 2017, pp. 159–166, 2018, doi: 10.1016/j.bios.2017.10.031.
- [43] P. Roy, S. Berger, and P. Schmuki, “TiO₂ nanotubes: Synthesis and applications,” *Angewandte Chemie - International Edition*, vol. 50, no. 13, pp. 2904–2939, 2011, doi: 10.1002/anie.201001374.
- [44] Y. Lin, G. Yuan, R. Liu, S. Zhou, S. W. Sheehan, and D. Wang, “Semiconductor nanostructure-based photoelectrochemical water splitting: A brief review,” *Chem Phys Lett*, vol. 507, no. 4–6, pp. 209–215, 2011, doi: 10.1016/j.cplett.2011.03.074.
- [45] J. Low, J. Yu, M. Jaroniec, S. Wageh, and A. A. Al-Ghamdi, “Heterojunction Photocatalysts,” *Advanced Materials*, vol. 29, no. 20, 2017, doi: 10.1002/adma.201601694.
- [46] W. Wang, J. Xiao, Y. Feng, Q. Guo, and L. Wang, “Characteristics of an air source heat pump with novel photoelectric sensors during periodic frost-defrost cycles,” *Appl Therm Eng*, vol. 50, no. 1, pp. 177–186, 2013, doi: 10.1016/j.applthermaleng.2012.06.019.
- [47] P. C. Chen, A. P. Periasamy, S. G. Harroun, W. P. Wu, and H. T. Chang, “Photoluminescence sensing systems based on copper, gold and silver nanomaterials,” *Coord Chem Rev*, vol. 320–321, pp. 129–138, 2016, doi: 10.1016/j.ccr.2015.12.002.
- [48] Y. Wang, H. L. Wang, H. Y. Li, X. Y. Wei, Z. L. Wang, and G. Zhu, “Enhanced High-Resolution Triboelectrification-Induced Electroluminescence for Self-Powered Visualized Interactive Sensing,” *ACS Appl Mater Interfaces*, vol. 11, no. 14, pp. 13796–13802, 2019, doi: 10.1021/acsami.9b02313.

- [49] B. Babamiri, D. Bahari, and A. Salimi, "Highly sensitive bioaffinity electrochemiluminescence sensors: Recent advances and future directions," *Biosens Bioelectron*, vol. 142, no. June, p. 111530, 2019, doi: 10.1016/j.bios.2019.111530.
- [50] D. Xu, Y. Wang, B. Xiong, and T. Li, "MEMS-based thermoelectric infrared sensors: A review," *Frontiers of Mechanical Engineering*, vol. 12, no. 4, pp. 557–566, 2017, doi: 10.1007/s11465-017-0441-2.
- [51] Z. Wang *et al.*, "Highly sensitive photoelectrochemical biosensor for kinase activity detection and inhibition based on the surface defect recognition and multiple signal amplification of metal-organic frameworks," *Biosens Bioelectron*, vol. 97, no. February, pp. 107–114, 2017, doi: 10.1016/j.bios.2017.05.011.
- [52] E. Al-Hetlani, M. O. Amin, and M. Madkour, "Detachable photocatalysts of anatase TiO₂ nanoparticles: Annulling surface charge for immediate photocatalyst separation," *Appl Surf Sci*, vol. 411, pp. 355–362, 2017, doi: 10.1016/j.apsusc.2017.03.151.
- [53] R. Tang *et al.*, "Layered MoS₂ coupled MOFs-derived dual-phase TiO₂ for enhanced photoelectrochemical performance," *J Mater Chem A Mater*, vol. 5, no. 10, pp. 4962–4971, 2017, doi: 10.1039/c6ta10511d.
- [54] S. Yu *et al.*, "Bismuth-containing semiconductors for photoelectrochemical sensing and biosensing," *Coord Chem Rev*, vol. 393, pp. 9–20, 2019, doi: 10.1016/j.ccr.2019.05.008.
- [55] Y. Zhou, H. Yin, W. Zhao, S. Ai, M. Science, and F. S. Analysis, "Electrochemical , electrochemiluminescent and photoelectrochemical bioanalysis of epigenetic modifiers : A comprehensive review," *Coord Chem Rev*, 2020, doi: 10.1016/j.ccr.2020.213519.
- [56] W. W. Zhao, J. J. Xu, and H. Y. Chen, "Photoelectrochemical DNA biosensors," *Chem Rev*, vol. 114, no. 15, pp. 7421–7441, 2014, doi: 10.1021/cr500100j.
- [57] V. Svitková, K. Konderíková, and K. Nemčková, "Photoelectrochemical aptasensors for detection of viruses," *Monatsh Chem*, vol. 153, no. 11, pp. 963–970, 2022, doi: 10.1007/s00706-022-02913-z.
- [58] Y. T. Xu *et al.*, "Cathodic photoelectrochemical bioanalysis," *TrAC - Trends in Analytical Chemistry*, vol. 114, pp. 81–88, 2019, doi: 10.1016/j.trac.2019.03.002.
- [59] B. Wang, J. T. Cao, and Y. M. Liu, "Recent progress of heterostructure-based photoelectrodes in photoelectrochemical biosensing: A mini review," *Analyst*, vol. 145, no. 4, pp. 1121–1128, 2020, doi: 10.1039/c9an02448d.

- [60] K. Sivula and R. Van De Krol, "Semiconducting materials for photoelectrochemical energy conversion," *Nat Rev Mater*, vol. 1, no. 2, 2016, doi: 10.1038/natrevmats.2015.10.
- [61] J. Wang and Z. Liu, "Recent advances in two-dimensional layered materials for photoelectrochemical sensing," *TrAC - Trends in Analytical Chemistry*, vol. 133, p. 116089, 2020, doi: 10.1016/j.trac.2020.116089.
- [62] T. Hu, Y. N. Zheng, M. J. Li, W. Bin Liang, Y. Q. Chai, and R. Yuan, "A Highly Sensitive Photoelectrochemical Assay with Donor-Acceptor-Type Material as Photoactive Material and Polyaniline as Signal Enhancer," *Anal Chem*, vol. 90, no. 10, pp. 6096–6101, 2018, doi: 10.1021/acs.analchem.8b00093.
- [63] Y. N. Zheng, W. Bin Liang, C. Y. Xiong, Y. L. Yuan, Y. Q. Chai, and R. Yuan, "Self-Enhanced Ultrasensitive Photoelectrochemical Biosensor Based on Nanocapsule Packaging Both Donor-Acceptor-Type Photoactive Material and Its Sensitizer," *Anal Chem*, vol. 88, no. 17, pp. 8698–8705, 2016, doi: 10.1021/acs.analchem.6b01984.
- [64] H. Wu *et al.*, "Photocatalytic and Photoelectrochemical Systems: Similarities and Differences," *Advanced Materials*, vol. 32, no. 18, pp. 1–21, 2020, doi: 10.1002/adma.201904717.
- [65] G. Divyapriya, S. Singh, C. A. Martínez-Huitle, J. Scaria, A. V. Karim, and P. V. Nidheesh, "Treatment of real wastewater by photoelectrochemical methods: An overview," *Chemosphere*, vol. 276, p. 130188, 2021, doi: 10.1016/j.chemosphere.2021.130188.
- [66] A. V. Emeline, V. N. Kuznetsov, V. K. Ryabchuk, and N. Serpone, "On the way to the creation of next generation photoactive materials," *Environmental Science and Pollution Research*, vol. 19, no. 9, pp. 3666–3675, 2012, doi: 10.1007/s11356-011-0665-3.
- [67] J. Li, X. Lin, Z. Zhang, W. Tu, and Z. Dai, "Red light-driven photoelectrochemical biosensing for ultrasensitive and scatheless assay of tumor cells based on hypotoxic AgInS₂ nanoparticles," *Biosensors and Bioelectronic*, vol. 126, no. July 2018, pp. 332–338, 2019, doi: 10.1016/j.bios.2018.09.096.
- [68] M. Q. Mesquita, C. J. Dias, M. G. P. M. S. Neves, A. Almeida, and M. A. F. Faustino, "Revisiting current photoactive materials for antimicrobial photodynamic therapy," *Molecules*, vol. 23, no. 10, 2018, doi: 10.3390/molecules23102424.

- [69] Y. Zhou, H. Yin, and S. Ai, "Applications of two-dimensional layered nanomaterials in photoelectrochemical sensors: A comprehensive review," *Coord Chem Rev*, vol. 447, p. 214156, 2021, doi: 10.1016/j.ccr.2021.214156.
- [70] C. Rodríguez-Seco, Y. S. Wang, K. Zaghbi, and D. Ma, *Photoactive nanomaterials enabled integrated photo-rechargeable batteries*, vol. 11, no. 8. 2022. doi: 10.1515/nanoph-2021-0782.
- [71] R. Jain, S. Mohanty, I. Sarode, S. Biswas, G. Singhvi, and S. K. Dubey, "Multifunctional Photoactive Nanomaterials for Photodynamic Therapy against Tumor: Recent Advancements and Perspectives," *Pharmaceutics*, vol. 15, no. 1, pp. 1–22, 2023, doi: 10.3390/pharmaceutics15010109.
- [72] S. Liang, D. T. Pierce, C. Amiot, and X. Zhao, "Photoactive nanomaterials for sensing trace analytes in biological samples," *Synthesis and Reactivity in Inorganic, Metal-Organic and Nano-Metal Chemistry*, vol. 35, no. 9, pp. 661–668, 2005, doi: 10.1080/15533170500299859.
- [73] S. K. Choi, "Mechanistic basis of light induced cytotoxicity of photoactive nanomaterials," *NanoImpact*, vol. 3–4, pp. 81–89, 2016, doi: 10.1016/j.impact.2016.09.001.
- [74] S. M. Louie, R. D. Tilton, and G. V. Lowry, "Critical review: Impacts of macromolecular coatings on critical physicochemical processes controlling environmental fate of nanomaterials," *Environ Sci Nano*, vol. 3, no. 2, pp. 283–310, 2016, doi: 10.1039/c5en00104h.
- [75] J. Li and J. Z. Zhang, "Optical properties and applications of hybrid semiconductor nanomaterials," *Coord Chem Rev*, vol. 253, no. 23–24, pp. 3015–3041, 2009, doi: 10.1016/j.ccr.2009.07.017.
- [76] B. Yao, J. Zhang, X. Fan, J. He, and Y. Li, "Surface Engineering of Nanomaterials for Photo-Electrochemical Water Splitting," *Small*, vol. 15, no. 1, pp. 1–20, 2019, doi: 10.1002/smll.201803746.
- [77] N. S. Mishra and P. Saravanan, "A Review on the Synergistic Features of Hexagonal Boron Nitride (White Graphene) as Adsorbent-Photo Active Nanomaterial," *ChemistrySelect*, vol. 3, no. 28, pp. 8023–8034, 2018, doi: 10.1002/slct.201801524.

- [78] Z. Lei, X. Ling, Q. Mei, S. Fu, J. Zhang, and Y. Zhang, “An Excitation Navigating Energy Migration of Lanthanide Ions in Upconversion Nanoparticles,” *Advanced Materials*, vol. 32, no. 9, pp. 1–7, 2020, doi: 10.1002/adma.201906225.
- [79] J. Juay, J. C. E. Yang, H. Bai, and D. D. Sun, “Novel ultralong and photoactive Bi₂Ti₄O₁₁/TiO₂ heterojunction nanofibers toward efficient textile wastewater treatment,” *RSC Adv*, vol. 12, no. 39, pp. 25449–25456, 2022, doi: 10.1039/d2ra02181a.
- [80] T. Edvinsson, “Optical quantum confinement and photocatalytic properties in two-, one- and zero-dimensional nanostructures,” *R Soc Open Sci*, vol. 5, no. 9, 2018, doi: 10.1098/rsos.180387.
- [81] X. Ma *et al.*, “Recent advances in metal/covalent organic framework-based materials for photoelectrochemical sensing applications,” *TrAC - Trends in Analytical Chemistry*, vol. 157, p. 116793, 2022, doi: 10.1016/j.trac.2022.116793.
- [82] W. W. Zhao, J. J. Xu, and H. Y. Chen, “Photoelectrochemical enzymatic biosensors,” *Biosens Bioelectron*, vol. 92, no. September 2016, pp. 294–304, 2017, doi: 10.1016/j.bios.2016.11.009.
- [83] W. Zhao, J. Xu, and H. Chen, “Biosensors and Bioelectronics Photoelectrochemical enzymatic biosensors,” *Biosensors and Bioelectronic*, vol. 92, no. October 2016, pp. 294–304, 2017, doi: 10.1016/j.bios.2016.11.009.
- [84] L. Lyu *et al.*, “Near-infrared light-mediated rare-earth nanocrystals: recent advances in improving photon conversion and alleviating the thermal effect,” *NPG Asia Mater*, vol. 10, no. 8, pp. 685–702, 2018, doi: 10.1038/s41427-018-0065-y.
- [85] G. Vitiello and G. Luciani, “Photocatalysis: Activity of nanomaterials,” *Catalysts*, vol. 11, no. 5, pp. 10–12, 2021, doi: 10.3390/catal11050611.
- [86] D. Monllor-Satoca, M. I. Díez-García, T. Lana-Villarreal, and R. Gómez, “Photoelectrocatalytic production of solar fuels with semiconductor oxides: Materials, activity and modeling,” *Chemical Communications*, vol. 56, no. 82, pp. 12272–12289, 2020, doi: 10.1039/d0cc04387g.
- [87] T. Du *et al.*, “Influence of light wavelength on the photoactivity, physicochemical transformation, and fate of graphene oxide in aqueous media,” *Environ Sci Nano*, vol. 5, no. 11, pp. 2590–2603, 2018, doi: 10.1039/C8EN00593A.

- [88] J. S. Chang and M. N. Chong, "Photoactive Nanomaterials: Applications in Wastewater Treatment and Their Environmental Fate," *Heterogeneous Photocatalysis*, pp. 331–349, 2021, doi: 10.1002/9783527815296.ch14.
- [89] S. Bilge, "Trends in Analytical Chemistry Current trends and strategies in the development of green MXene- based photoelectrochemical sensing application," *Trends in Analytical Chemistry*, vol. 163, 2023, doi: 10.1016/j.trac.2023.117059.
- [90] W. Zhao, J. Xu, and H. Chen, "Photoelectrochemical aptasensing," *Trends in Analytical Chemistry*, 2016, doi: 10.1016/j.trac.2016.06.020.
- [91] L. Ge, Q. Liu, and W. Kun, "Recent developments of photoelectrochemical biosensors for food analysis," *J Mater Chem B*, pp. 7283–7300, 2019, doi: 10.1039/c9tb01644a.
- [92] Z. Kang *et al.*, "Enhanced photoelectrochemical property of ZnO nanorods array synthesized on reduced graphene oxide for self-powered biosensing application," *Biosens Bioelectron*, vol. 64, pp. 499–504, 2015, doi: 10.1016/j.bios.2014.09.055.
- [93] H. Wang *et al.*, "Photoelectrochemical Immunosensor for Detection of Carcinoembryonic Antigen Based on 2D TiO₂ Nanosheets and Carboxylated Graphitic Carbon Nitride," *Nature Publishing Group*, no. May, pp. 1–7, 2016, doi: 10.1038/srep27385.
- [94] Y. Li, X. Zhang, X. Liu, and W. Pan, "Chemical Science immunomodulators for cancer immunotherapy," *Royal Society of Chemistry*, pp. 3130–3145, 2021, doi: 10.1039/d0sc06557a.
- [95] X. Zhang, S. Li, X. Jin, and X. Li, "Biosensors and Bioelectronics Aptamer based photoelectrochemical cytosensor with layer-by-layer assembly of CdSe semiconductor nanoparticles as photoelectrochemically active species," *Biosens Bioelectron*, vol. 26, no. 8, pp. 3674–3678, 2011, doi: 10.1016/j.bios.2011.01.030.
- [96] F. Liu, Y. Zhang, J. Yu, S. Wang, S. Ge, and X. Song, "Biosensors and Bioelectronics Application of ZnO/ graphene and S6 aptamers for sensitive photoelectrochemical detection of SK-BR-3 breast cancer cells based on a disposable indium tin oxide device," *Biosensors and Bioelectronic*, vol. 51, pp. 413–420, 2014, doi: 10.1016/j.bios.2013.07.066.
- [97] X. Zhang, M. Liu, H. Liu, and S. Zhang, "Biosensors and Bioelectronics Low-toxic Ag₂S quantum dots for photoelectrochemical detection glucose and cancer cells," *Biosensors and Bioelectronic*, vol. 56, pp. 307–312, 2014, doi: 10.1016/j.bios.2014.01.033.

- [98] Y. Ruan, F. Xu, W. Zhao, J. Xu, and H. Chen, "Protein Binding Bends the Gold Nanoparticle Capped DNA Sequence: Towards Novel Energy-transfer based Photoelectrochemical Protein Detection," *Anal Chem*, 2016, doi: 10.1021/acs.analchem.6b00012.
- [99] H. X. and H. P. Xiao Xiao, Shasha Zheng, Xinran Li, Guangxun Zhang, Xiaotian Guo, "Facile Synthesis of Ultrathin Ni-MOF Nanobelts for High-Efficiency Determination of Glucose in Human Serum," *Materials Chemistry B*, 2017, doi: 10.1039/C7TB00180K.
- [100] K.-J. H. Hong-Lei Shuai, Xu Wu, "Molybdenum Disulfide Spheres-based Electrochemical Aptasensor for Proteins Detection," *Materials Chemistry B*, 2017, doi: 10.1039/C7TB01276D.
- [101] Y. Yang, J. Liang, W. Jin, Y. Li, and M. Xuan, "The design and growth of peanut-like CuS/BiVO₄ composites for photoelectrochemical sensing," *RSC Adv*, pp. 14670–14678, 2020, doi: 10.1039/d0ra01307b.
- [102] Y. Pang *et al.*, "Synthesis of α -Bi₂Mo₃O₁₂ / TiO₂ Nanotube Arrays for Photoelectrochemical COD Detection Application Synthesis of α -Bi₂Mo₃O₁₂ / TiO₂ Nanotube Arrays for Photoelectrochemical COD," *Langmuir*, 2017, doi: 10.1021/acs.langmuir.7b01826.
- [103] Y. Zang, J. Fan, Y. Ju, H. Xue, and H. Pang, "Current Advances in Semiconductor Nanomaterial-Based Photoelectrochemical Biosensing," *Chemistry - A European Journal*, vol. 24, no. 53, pp. 14010–14027, 2018, doi: 10.1002/chem.201801358.
- [104] Z. Wang *et al.*, "Nucleic acid-based ratiometric electrochemiluminescent, electrochemical and photoelectrochemical biosensors: a review," *Springer Nature*, 2019.
- [105] H. Dai, S. Zhang, Z. Hong, and Y. Lin, "A Potentiometric Addressable Photoelectrochemical Biosensor for Sensitive Detection of Two Biomarkers," *Anal Chem*, vol. 88, no. 19, pp. 9532–9538, 2016, doi: 10.1021/acs.analchem.6b02101.
- [106] L. Yang, S. Zhang, and X. Liu, "Detection signal amplification strategies at nanomaterial-based photoelectrochemical biosensors," *J Mater Chem B*, 2020, doi: 10.1039/d0tb01191f.
- [107] F. Mo, J. Wu, M. Chen, H. Meng, Q. Han, and Y. Fu, "Enzyme-free 'on-off-on' photoelectrochemical biosensor based on cascaded quadratic amplification strategy for miRNA 141 detection," *Sens Actuators B Chem*, vol. 289, no. March, pp. 269–276, 2019, doi: 10.1016/j.snb.2019.03.044.

- [108] M. Xue, “Applications of Nanomaterials-Based Photoelectrochemical Biosensors for Highly Sensitive Detection,” *2021 3rd International Academic Exchange Conference on Science and Technology Innovation, IAECST 2021*, pp. 1037–1041, 2021, doi: 10.1109/IAECST54258.2021.9695631.
- [109] E. Heydari-Bafrooei and A. A. Ensafi, “Nanomaterials-based biosensing strategies for biomarkers diagnosis, a review,” *Biosens Bioelectron X*, vol. 13, no. August 2022, p. 100245, 2023, doi: 10.1016/j.biosx.2022.100245.
- [110] F. X. Xiao and B. Liu, “Plasmon-Dictated Photo-Electrochemical Water Splitting for Solar-to-Chemical Energy Conversion: Current Status and Future Perspectives,” *Adv Mater Interfaces*, vol. 5, no. 6, pp. 1–21, 2018, doi: 10.1002/admi.201701098.
- [111] C. Xia, H. Wang, J. K. Kim, and J. Wang, “Rational Design of Metal Oxide-Based Heterostructure for Efficient Photocatalytic and Photoelectrochemical Systems,” *Adv Funct Mater*, vol. 31, no. 12, pp. 1–31, 2021, doi: 10.1002/adfm.202008247.
- [112] L. Wang *et al.*, “Graphitic carbon nitride (g-C₃N₄)-based nanosized heteroarrays: Promising materials for photoelectrochemical water splitting,” *Carbon Energy*, vol. 2, no. 2, pp. 223–250, 2020, doi: 10.1002/cey2.48.
- [113] H. Zhou, J. Liu, and S. Zhang, “Quantum dot-based photoelectric conversion for biosensing applications,” *TrAC - Trends in Analytical Chemistry*, vol. 67, pp. 56–73, 2015, doi: 10.1016/j.trac.2014.12.007.
- [114] C. K. Sumesh and S. C. Peter, “Two-dimensional semiconductor transition metal based chalcogenide based heterostructures for water splitting applications,” *Dalton Transactions*, vol. 48, no. 34, pp. 12772–12802, 2019, doi: 10.1039/c9dt01581g.
- [115] Z. Kang *et al.*, “Self-powered photoelectrochemical biosensing platform based on Au NPs@ZnO nanorods array,” *Nano Res*, vol. 9, no. 2, pp. 344–352, 2016, doi: 10.1007/s12274-015-0913-9.
- [116] Q. Huang, Y. Wang, L. Lei, Z. Xu, and W. Zhang, “Photoelectrochemical biosensor for acetylcholinesterase activity study based on metal oxide semiconductor nanocomposites,” *Journal of Electroanalytical Chemistry*, vol. 781, pp. 377–382, 2016, doi: 10.1016/j.jelechem.2016.07.007.

- [117] J. Shu, Z. Qiu, S. Lv, K. Zhang, and D. Tang, "Plasmonic Enhancement Coupling with Defect-Engineered TiO_{2-x}: A Mode for Sensitive Photoelectrochemical Biosensing," *Anal Chem*, vol. 90, no. 4, pp. 2425–2429, 2018, doi: 10.1021/acs.analchem.7b05296.
- [118] O. K. Okoth, K. Yan, J. Feng, and J. Zhang, "Label-free photoelectrochemical aptasensing of diclofenac based on gold nanoparticles and graphene-doped CdS," *Sens Actuators B Chem*, vol. 256, pp. 334–341, 2018, doi: 10.1016/j.snb.2017.10.089.
- [119] S. Bellani *et al.*, "Hybrid Organic/Inorganic Nanostructures for Highly Sensitive Photoelectrochemical Detection of Dissolved Oxygen in Aqueous Media," *Adv Funct Mater*, vol. 25, no. 28, pp. 4531–4538, 2015, doi: 10.1002/adfm.201500701.
- [120] Y. Chen *et al.*, "Co₃O₄ nanoparticles/graphitic carbon nitride heterojunction for photoelectrochemical aptasensor of oxytetracycline," *Anal Chim Acta*, vol. 1125, pp. 299–307, 2020, doi: 10.1016/j.aca.2020.05.038.
- [121] L. Tang *et al.*, "Highly sensitive detection of microcystin-LR under visible light using a self-powered photoelectrochemical aptasensor based on a CoO/Au/g-C₃N₄ Z-scheme heterojunction," *Nanoscale*, vol. 11, no. 25, pp. 12198–12209, 2019, doi: 10.1039/c9nr03004b.
- [122] Y. Li, Y. Bu, F. Jiang, X. Dai, and J. P. Ao, "Fabrication of ultra-sensitive photoelectrochemical aptamer biosensor: Based on semiconductor/DNA interfacial multifunctional reconciliation via 2D-C₃N₄," *Biosens Bioelectron*, vol. 150, no. October 2019, p. 111903, 2020, doi: 10.1016/j.bios.2019.111903.
- [123] H. Qi, B. Sun, J. Dong, L. Cui, T. Feng, and S. Ai, "Facile synthesis of two-dimensional tailored graphitic carbon nitride with enhanced photoelectrochemical properties through a three-step polycondensation method for photocatalysis and photoelectrochemical immunosensor," *Sens Actuators B Chem*, vol. 285, no. October 2018, pp. 42–48, 2019, doi: 10.1016/j.snb.2019.01.028.
- [124] X. Li, L. Zhu, Y. Zhou, H. Yin, and S. Ai, "Enhanced Photoelectrochemical Method for Sensitive Detection of Protein Kinase A Activity Using TiO₂/g-C₃N₄, PAMAM Dendrimer, and Alkaline Phosphatase," *Anal Chem*, vol. 89, no. 4, pp. 2369–2376, 2017, doi: 10.1021/acs.analchem.6b04184.
- [125] Y. X. Dong, J. T. Cao, B. Wang, S. H. Ma, and Y. M. Liu, "Spatial-Resolved Photoelectrochemical Biosensing Array Based on a CdS@g-C₃N₄ Heterojunction: A

- Universal Immunosensing Platform for Accurate Detection,” *ACS Appl Mater Interfaces*, vol. 10, no. 4, pp. 3723–3731, 2018, doi: 10.1021/acsami.7b13557.
- [126] Y. X. Dong, J. T. Cao, B. Wang, S. H. Ma, and Y. M. Liu, “Exciton-Plasmon Interactions between CdS@g-C3N4 Heterojunction and Au@Ag Nanoparticles Coupled with DNAase-Triggered Signal Amplification: Toward Highly Sensitive Photoelectrochemical Bioanalysis of MicroRNA,” *ACS Sustain Chem Eng*, vol. 5, no. 11, pp. 10840–10848, 2017, doi: 10.1021/acssuschemeng.7b02774.
- [127] M. Sun, R. Li, J. Zhang, K. Yan, and M. Liu, “One-pot synthesis of a CdS-reduced graphene oxide-carbon nitride composite for self-powered photoelectrochemical aptasensing of PCB72,” *Nanoscale*, vol. 11, no. 13, pp. 5982–5988, 2019, doi: 10.1039/C9NR00966C.
- [128] F. Wang *et al.*, “Photoelectrochemical biosensor based on CdS quantum dots anchored h-BN nanosheets and tripodal DNA walker for sensitive detection of miRNA-141,” *Anal Chim Acta*, vol. 1226, no. August, p. 340265, 2022, doi: 10.1016/j.aca.2022.340265.
- [129] Y. Zang, J. Fan, H. Zhang, Q. Xu, J. Jiang, and H. Xue, “Dual-functional β -CD@CdS nanorod/WS2 nanosheet heterostructures coupled with strand displacement reaction-mediated photocurrent quenching for an ultrasensitive MicroRNA-21 assay,” *Electrochim Acta*, vol. 334, p. 135581, 2020, doi: 10.1016/j.electacta.2019.135581.
- [130] X. Hun, S. Wang, S. Wang, J. Zhao, and X. Luo, “A photoelectrochemical sensor for ultrasensitive dopamine detection based on single-layer NanoMoS₂ modified gold electrode,” *Sens Actuators B Chem*, vol. 249, pp. 83–89, 2017, doi: 10.1016/j.snb.2017.04.065.
- [131] Y. Zheng *et al.*, “Antibody-free photoelectrochemical biosensor for DNA carboxylation detection based on SnS₂@Ti₃C₂ heterojunction,” *Anal Chim Acta*, vol. 1251, p. 341011, Apr. 2023, doi: 10.1016/J.ACA.2023.341011.
- [132] D. Jiang, X. Du, L. Zhou, H. Li, and K. Wang, “New Insights towards Efficient Charge Separation Mechanism for High-Performances Photoelectrochemical Aptasensing: Enhanced Charge Carriers Lifetime via Coupling Ultrathin MoS₂ Nanoplates with Nitrogen Doped Graphene Quantum Dots New Insights towards Eff,” 2017, doi: 10.1021/acs.analchem.6b04949.
- [133] F. Li *et al.*, “Photoelectrochemical Biosensor for DNA Formylation Detection in Genomic DNA of Maize Seedlings Based on Black TiO₂-Enhanced Photoactivity of MoS₂/WS₂

- Heterojunction,” *ACS Sens*, vol. 5, no. 4, pp. 1092–1101, 2020, doi: 10.1021/acssensors.0c00036.
- [134] L. Huang *et al.*, “A light-driven photoelectrochemical sensor for highly selective detection of hydroquinone based on type-II heterojunction formed by carbon nanotubes immobilized in 3D honeycomb CdS/SnS₂,” *J Colloid Interface Sci*, vol. 643, pp. 585–599, 2023, doi: 10.1016/j.jcis.2023.03.141.
- [135] Y. Zhang, W. Guo, Y. Zhang, and W. D. Wei, “Plasmonic Photoelectrochemistry : In View of Hot Carriers,” vol. 2006654, pp. 1–16, 2021, doi: 10.1002/adma.202006654.
- [136] J. Duchene, G. Tagliabue, A. J. Welch, W. Cheng, and H. A. Atwater, “Reduction with Plasmonic Au / p-GaN Photocathodes Hot Hole Collection and Photoelectrochemical CO₂ Reduction with Plasmonic Au / p-GaN Photocathodes,” 2018, doi: 10.1021/acs.nanolett.8b00241.
- [137] K. K. Rani *et al.*, “Electrochemistry Plasmonic photoelectrochemical reactions on noble metal electrodes of nanostructures,” *Curr Opin Electrochem*, vol. 34, p. 100985, 2022, doi: 10.1016/j.coelec.2022.100985.
- [138] P. Zhang, T. Wang, and J. Gong, “Mechanistic Understanding of the Plasmonic Enhancement for Solar Water Splitting,” *Advanced Materials*, pp. 5328–5342, 2015, doi: 10.1002/adma.201500888.
- [139] J.-J. X. and H.-Y. C. Wei-Wei Zhao, Chun-Yuan Tian, “The coupling of localized surface plasmon resonance-based photoelectrochemistry and nanoparticle size effect : towards novel plasmonic photoelectrochemical biosensing w,” *ChemComm*, vol. 1, pp. 895–897, 2012, doi: 10.1039/c1cc16775h.
- [140] N. Zhang *et al.*, “Near-field dielectric scattering promotes optical absorption by platinum nanoparticles,” *Nat Photonics*, vol. 10, no. July, 2016, doi: 10.1038/nphoton.2016.76.
- [141] J. Tang, P. Xiong, Y. Cheng, Y. Chen, S. Peng, and Z. Zhu, “Biosensors and Bioelectronics Enzymatic oxydate-triggered AgNPs etching : A novel signal-on photoelectrochemical immunosensing platform based on Ag @ AgCl nanocubes loaded RGO plasmonic heterostructure,” *Biosensors and Bioelectronic*, vol. 130, no. August 2018, pp. 125–131, 2019, doi: 10.1016/j.bios.2019.01.014.

- [142] Y. H. J. and D. H. K. Saji Thomas Kochuveedu, “A study on the mechanism for the interaction of light with noble metal-metal oxide semiconductor nanostructures for various photophysical applications,” *Chem Soc Rev*, 2013, doi: 10.1039/c3cs60043b.
- [143] A. Gongming Wang, a,# Yi Yang, a,# Yichuan Ling, a Hanyu Wang, a Xihong Lu, b Ying-Chih Pu, a Jin Z. Zhang, a Yexiang Tongb and Yat Li* and A, “An Electrochemical Method to Enhance the Performance of Metal Oxides for Photoelectrochemical Water Oxidation,” *Materials Chemistry A*, 2016, doi: 10.1039/C5TA10477G.
- [144] J. E. Katz, T. R. Gingrich, E. A. Santori, and N. S. Lewis, “Combinatorial synthesis and high-throughput photopotential and photocurrent screening of mixed-metal oxides for photoelectrochemical water splitting,” *Energy Environ Sci*, pp. 103–112, 2009, doi: 10.1039/b812177j.
- [145] Y. Yang, S. Niu, D. Han, T. Liu, G. Wang, and Y. Li, “Progress in Developing Metal Oxide Nanomaterials for Photoelectrochemical Water Splitting,” *Adv Energy Mater*, vol. 1700555, pp. 1–26, 2017, doi: 10.1002/aenm.201700555.
- [146] D. A. Links, “Oxygen-deficient metal oxide nanostructures for photoelectrochemical water oxidation and other applications,” *Nanoscale*, pp. 6682–6691, 2012, doi: 10.1039/c2nr32222f.
- [147] b J. R. M. Carles Ros, a,* Teresa Andreu, a, “Photoelectrochemical water splitting: a road from stable metal oxides to protected thin film solar cells,” *Materials Chemistry A*, 2020, doi: 10.1039/D0TA02755C.
- [148] C. Venkata, K. Raghava, N. P. Shetti, J. Shim, T. M. Aminabhavi, and D. D. Dionysiou, “ScienceDirect Hetero-nanostructured metal oxide-based hybrid photocatalysts for enhanced photoelectrochemical water splitting e A review,” *Int J Hydrogen Energy*, vol. 45, no. 36, pp. 18331–18347, 2019, doi: 10.1016/j.ijhydene.2019.02.109.
- [149] S. Nadzirah *et al.*, “State-of-the-Art on Functional Titanium Dioxide-Integrated Nano-Hybrids in Electrical Biosensors,” *Crit Rev Anal Chem*, vol. 52, no. 3, pp. 637–648, 2022, doi: 10.1080/10408347.2020.1816447.
- [150] N. Wu, “Plasmonic Metal-Semiconductor Photocatalysts and Photoelectrochemical Cells: A Review,” *Nanoscale*, 2018, doi: 10.1039/C7NR08487K.

- [151] A. Rajabpour, S. Bazrafshan, and S. Volz, "Carbon-nitride 2D nanostructures: Thermal conductivity and interfacial thermal conductance with the silica substrate," *Physical Chemistry Chemical Physics*, vol. 21, no. 5, pp. 2507–2512, 2019, doi: 10.1039/c8cp06992a.
- [152] W. J. Ong, L. L. Tan, S. P. Chai, S. T. Yong, and A. R. Mohamed, "Surface charge modification via protonation of graphitic carbon nitride (g-C₃N₄) for electrostatic self-assembly construction of 2D/2D reduced graphene oxide (rGO)/g-C₃N₄ nanostructures toward enhanced photocatalytic reduction of carbon dioxide to methane," *Nano Energy*, vol. 13, pp. 757–770, 2015, doi: 10.1016/j.nanoen.2015.03.014.
- [153] H. Zeng *et al.*, "Construction of a Z-scheme g-C₃N₄/Ag/AgI heterojunction for highly selective photoelectrochemical detection of hydrogen sulfide," *Chemical Communications*, vol. 55, no. 79, pp. 11940–11943, 2019, doi: 10.1039/c9cc05356e.
- [154] M. Inagaki, T. Tsumura, T. Kinumoto, and M. Toyoda, "Graphitic carbon nitrides (g-C₃N₄) with comparative discussion to carbon materials," *Carbon N Y*, vol. 141, pp. 580–607, 2019, doi: 10.1016/j.carbon.2018.09.082.
- [155] W. Li *et al.*, "Graphitic carbon nitride/ α -Fe₂O₃ heterostructures for sensitive photoelectrochemical non-enzymatic glucose sensor," *Inorg Chem Commun*, vol. 106, no. June, pp. 211–216, 2019, doi: 10.1016/j.inoche.2019.06.015.
- [156] S. S. Low, Z. Chen, Y. Li, Y. Lu, and Q. Liu, "Trends in Analytical Chemistry Design principle in biosensing: Critical analysis based on graphitic carbon nitride (g-C₃N₄) photoelectrochemical biosensor," *Trends in Analytical Chemistry*, vol. 145, p. 116454, 2021, doi: 10.1016/j.trac.2021.116454.
- [157] J. Liang, D. Chen, X. Yao, K. Zhang, F. Qu, and L. Qin, "Recent Progress and Development in Inorganic Halide Perovskite Quantum Dots for Photoelectrochemical Applications," *Nano-Micro Small*, vol. 1903398, pp. 1–20, 2019, doi: 10.1002/sml.201903398.
- [158] J. Shu and D. Tang, "Current Advances in Quantum-Dots-Based Photoelectrochemical Immunoassays," *Chem Asian J*, pp. 2780–2789, 2017, doi: 10.1002/asia.201701229.
- [159] Z. Yue *et al.*, "Quantum-Dot-Based Photoelectrochemical Sensors for Chemical and Biological Detection," *Applied Materials and Interfaces*, 2013, doi: 10.1021/am3028662.
- [160] N. Zhang, L. Zhang, Y. Ruan, W. Zhao, J. Xu, and H. Chen, "Biosensors and Bioelectronics Quantum-dots-based photoelectrochemical bioanalysis highlighted with recent examples,"

- Biosensors and Bioelectronic*, vol. 94, no. March, pp. 207–218, 2017, doi: 10.1016/j.bios.2017.03.011.
- [161] L. Jin, H. Zhao, Z. M. Wang, and F. Rosei, “Quantum Dots-Based Photoelectrochemical Hydrogen Evolution from Water Splitting,” *Adv Energy Mater*, vol. 2003233, pp. 1–28, 2021, doi: 10.1002/aenm.202003233.
- [162] M. Van Erdewyk, D. B. Lorenz, and J. B. Sambur, “Answering old questions with new techniques : Understanding performance-limiting factors in transition metal dichalcogenide photoelectrochemical solar cells,” *Curr Opin Electrochem*, vol. 37, no. 1, p. 101173, 2022, doi: 10.1016/j.coelec.2022.101173.
- [163] D. Bulters, R. Sukanya, C. Daniele, S. Alves, and C. B. Breslin, “Review — Recent Developments in the Applications of 2D Transition Metal Dichalcogenides as Electrocatalysts in the Generation of Hydrogen for Renewable Energy Conversion Review — Recent Developments in the Applications of 2D Transition Metal Dichalcogenid,” *The Electrochemical Society*, 2022, doi: 10.1149/1945-7111/ac7172.
- [164] V. Nguyen, T. P. Nguyen, T. Le, and D. N. Vo, “Recent advances in two-dimensional transition metal dichalcogenides as photoelectrocatalyst for hydrogen evolution reaction,” *Society of Chemical Industry I*, no. October 2019, 2020, doi: 10.1002/jctb.6335.
- [165] J. Wang and Z. Liu, “Trends in Analytical Chemistry Recent advances in two-dimensional layered materials for photoelectrochemical sensing,” *Trends in Analytical Chemistry*, vol. 133, p. 116089, 2020, doi: 10.1016/j.trac.2020.116089.
- [166] M. Pumera and A. H. Loo, “Layered transition-metal dichalcogenides (MoS₂ and WS₂) for sensing and biosensing,” *Trends in Analytical Chemistry*, vol. 61, pp. 49–53, 2014, doi: 10.1016/j.trac.2014.05.009.
- [167] D. Jiang, X. Du, Q. Liu, N. Hao, and K. Wang, “MoS₂ / nitrogen doped graphene hydrogels p-n heterojunction : Efficient charge transfer property for highly sensitive and selective photoelectrochemical analysis of chloramphenicol,” *Biosensors and Bioelectronic*, vol. 126, no. November 2018, pp. 463–469, 2019, doi: 10.1016/j.bios.2018.11.018.
- [168] L. Ge, Q. Hong, H. Li, C. Liu, and F. Li, “Direct-Laser-Writing of Metal Sulfide-Graphene Nanocomposite Photoelectrode toward Sensitive Photoelectrochemical Sensing,” *Adv Funct Mater*, vol. 1904000, pp. 1–10, 2019, doi: 10.1002/adfm.201904000.

- [169] L. Zheng, F. Teng, X. Ye, H. Zheng, and X. Fang, "Photo / Electrochemical Applications of Metal Sulfide / TiO₂ Heterostructures," *Adv Funct Mater*, vol. 1902355, pp. 1–32, 2019, doi: 10.1002/aenm.201902355.
- [170] I. Ibrahim, H. N. Lim, O. K. Abou-zied, N. M. Huang, and P. Estrela, "Cadmium Sulfide Nanoparticles Decorated with Au Quantum Dots as Ultrasensitive Photoelectrochemical Sensor for Selective Detection of Copper (II) Ions," *J Phys Chem*, no. 12, 2016, doi: 10.1021/acs.jpcc.6b06929.
- [171] L. Shi, Y. Yin, L. Zhang, S. Wang, M. Sillanpää, and H. Sun, "Design and engineering heterojunctions for the photoelectrochemical monitoring of environmental pollutants : A review," *Appl Catal B*, vol. 248, no. October 2018, pp. 405–422, 2019, doi: 10.1016/j.apcatb.2019.02.044.
- [172] D. Fan *et al.*, "An ultrasensitive photoelectrochemical immunosensor for insulin detection based on BiOBr/Ag₂S composite by in-situ growth method with high visible-light activity," *Biosens Bioelectron*, vol. 97, no. March, pp. 253–259, 2017, doi: 10.1016/j.bios.2017.05.044.
- [173] W. Zhao, J. Xu, and H. Chen, "Chem Soc Rev Photoelectrochemical bioanalysis : the state of the art," *Chem Soc Rev*, 2014, doi: 10.1039/C4CS00228H.
- [174] P. Yang *et al.*, "Recent Trends in Self-Powered Photoelectrochemical Sensors: From the Perspective of Signal Output," *ACS Sens*, vol. 9, pp. 577–588, 2024, doi: 10.1021/acssensors.3c02198.
- [175] Y. Zang, J. Fan, Y. Ju, H. Xue, and H. Pang, "Current Advances in Semiconductor Nanomaterial-Based Photoelectrochemical Biosensing," *Chemistry - A European Journal*, vol. 24, no. 53, pp. 14010–14027, 2018, doi: 10.1002/chem.201801358.
- [176] and D. T. Zhenli Qiu, "Nanostructures-based photoelectrochemical sensing platforms for biomedical applications," *J Mater Chem B*, 2020, doi: 10.1039/C9TB02844G.
- [177] T. Li *et al.*, "Near-infrared Responsive Photoelectrochemical Biosensors," *Electroanalysis*, vol. 34, no. 6, pp. 956–965, 2022, doi: 10.1002/elan.202100355.
- [178] Z. Qiu, J. Shu, and D. Tang, "NaYF₄:Yb,Er Upconversion Nanotransducer with in Situ Fabrication of Ag₂S for Near-Infrared Light Responsive Photoelectrochemical Biosensor," *Anal Chem*, vol. 90, no. 20, pp. 12214–12220, 2018, doi: 10.1021/acs.analchem.8b03446.

- [179] Y. Zhai *et al.*, “Near-infrared-light-triggered photoelectrochemical biosensor for detection of alpha-fetoprotein based on upconversion nanophosphors,” *Sens Actuators B Chem*, vol. 286, no. January, pp. 468–475, 2019, doi: 10.1016/j.snb.2019.01.080.
- [180] Q. Han, X. Zhao, N. Na, and J. Ouyang, “Integrating Near-Infrared Visual Fluorescence with a Photoelectrochemical Sensing System for Dual Readout Detection of Biomolecules,” *Anal Chem*, vol. 93, no. 7, pp. 3486–3492, 2021, doi: 10.1021/acs.analchem.0c04802.
- [181] S. K. Sun, H. F. Wang, and X. P. Yan, “Engineering Persistent Luminescence Nanoparticles for Biological Applications: From Biosensing/Bioimaging to Theranostics,” *Acc Chem Res*, vol. 51, no. 5, pp. 1131–1143, 2018, doi: 10.1021/acs.accounts.7b00619.
- [182] Z. Lei *et al.*, “Stable, Wavelength-Tunable Fluorescent Dyes in the NIR-II Region for In Vivo High-Contrast Bioimaging and Multiplexed Biosensing,” *Angewandte Chemie*, vol. 131, no. 24, pp. 8250–8255, 2019, doi: 10.1002/ange.201904182.
- [183] Y. Cai, Z. Wei, C. Song, C. Tang, W. Han, and X. Dong, “Optical nano-agents in the second near-infrared window for biomedical applications,” *Chem Soc Rev*, vol. 48, no. 1, pp. 22–37, 2019, doi: 10.1039/c8cs00494c.
- [184] and L. N. Likun Huang, Zhishan Liang, Fang Zhang, Hui Luo, Ruilian Liang, Fangjie Han, Zhifang Wu, Dongxue Han*, Jun Shen*, “Upconversion NaYF₄:Yb/Er–TiO₂–Ti₃C₂ Heterostructure-Based Near-Infrared Light-Driven Photoelectrochemical Biosensor for Highly Sensitive and Selective d-Serine Detection,” *Anal Chem*, 2022, doi: 10.1021/acs.analchem.2c04101.
- [185] Y. Tian *et al.*, “Alloyed AuPt nanoframes loaded on h-BN nanosheets as an ingenious ultrasensitive near-infrared photoelectrochemical biosensor for accurate monitoring glucose in human tears,” *Biosens Bioelectron*, vol. 192, no. July, p. 113490, 2021, doi: 10.1016/j.bios.2021.113490.
- [186] W. T. and Z. D. Ruyan Li, Rong Yan, Jianchun Bao, “A localized surface plasmon resonance-enhanced photoelectrochemical biosensing strategy for highly sensitive and scatheless cell assay under red light excitation,” *Chemical Communications*, 2016, doi: 10.1039/C6CC05964C.
- [187] R. Li, W. Tu, H. Wang, and Z. Dai, “Near-Infrared Light Excited and Localized Surface Plasmon Resonance-Enhanced Photoelectrochemical Biosensing Platform for Cell

- Analysis,” *Anal Chem*, vol. 90, no. 15, pp. 9403–9409, 2018, doi: 10.1021/acs.analchem.8b02047.
- [188] Z. Qiu, J. Shu, and D. Tang, “Near-Infrared-to-Ultraviolet Light-Mediated Photoelectrochemical Aptasensing Platform for Cancer Biomarker Based on Core-Shell NaYF₄:Yb,Tm@TiO₂ Upconversion Microrods,” *Anal Chem*, vol. 90, no. 1, pp. 1021–1028, 2018, doi: 10.1021/acs.analchem.7b04479.
- [189] S. S. Wang, W. C. Hu, F. F. Liu, Q. Y. Xu, and C. Wang, “Insights into direct plasmon-activated electrocatalysis on gold nanostar via efficient photothermal effect and reduced activation energy,” *Electrochim Acta*, vol. 301, pp. 359–365, 2019, doi: 10.1016/j.electacta.2019.01.172.
- [190] X. Xu *et al.*, “A near-infrared photoelectrochemical aptasensing system based on Bi₂O₃ S nanoflowers and gold nanoparticles for high-performance determination of,” *Anal Chim Acta*, vol. 1251, no. December 2022, p. 340982, 2023, doi: 10.1016/j.aca.2023.340982.
- [191] Y. Zhai *et al.*, “Near-infrared-light-triggered photoelectrochemical biosensor for detection of alpha-fetoprotein based on upconversion nanophosphors,” *Sens Actuators B Chem*, vol. 286, no. September 2018, pp. 468–475, 2019, doi: 10.1016/j.snb.2019.01.080.
- [192] X. Zhou *et al.*, “NIR-driven photoelectrochemical-fluorescent dual-mode biosensor based on bipedal DNA walker for ultrasensitive detection of microRNA,” *Biosens Bioelectron*, vol. 247, no. December 2023, p. 115916, 2024, doi: 10.1016/j.bios.2023.115916.
- [193] C. Zheng *et al.*, “A novel near-infrared light-responsive photoelectrochemical platform for detecting microcystin-LR in fish based on Ag₂S cubes and plasmonic Au nanoparticles,” *Talanta*, vol. 221, no. May 2020, p. 121447, 2021, doi: 10.1016/j.talanta.2020.121447.
- [194] J. Li, X. Lin, Z. Zhang, W. Tu, and Z. Dai, “Red light-driven photoelectrochemical biosensing for ultrasensitive and scatheless assay of tumor cells based on hypotoxic AgInS₂ nanoparticles,” *Biosens Bioelectron*, vol. 126, no. October 2018, pp. 332–338, 2019, doi: 10.1016/j.bios.2018.09.096.
- [195] S. Lv, K. Zhang, L. Zhu, and D. Tang, “ZIF-8-Assisted NaYF₄:Yb,Tm@ZnO Converter with Exonuclease III- Powered DNA Walker for Near-Infrared Light Responsive Biosensor,” *Anal Chem*, 2020, doi: 10.1021/acs.analchem.9b04710.
- [196] B. Fu, W. Wu, L. Gan, and Z. Zhang, “Bulk/Surface Defects Engineered TiO₂ Nanotube Photonic Crystals Coupled with Plasmonic Gold Nanoparticles for Effective in Vivo Near-

- Infrared Light Photoelectrochemical Detection,” *Anal Chem*, 2019, doi: 10.1021/acs.analchem.9b03733.
- [197] J. Ji, Y. Shen, K. Wu, H. Yang, Y. Lv, and S. Liu, “Exfoliation and Sensitization of 2D Carbon Nitride for Photoelectrochemical Biosensing under Red Light,” *Chemistry - A European Journal*, 2019, doi: 10.1002/chem.201904076.
- [198] X. Chen *et al.*, “A novel upconversion luminescence derived photoelectrochemical immunoassay: ultrasensitive detection to alpha-fetoprotein,” *Nanoscale*, pp. 16357–16364, 2017, doi: 10.1039/c7nr05577c.
- [199] Z. Qiu, J. Shu, J. Liu, and D. Tang, “Dual-Channel Photoelectrochemical Ratiometric Aptasensor with up-Converting Nanocrystals Using Spatial-Resolved Technique on Homemade 3D Printed Device,” *Anal Chem*, 2019, doi: 10.1021/acs.analchem.8b05455.
- [200] Z. Luo, L. Zhang, R. Zeng, L. Su, and D. Tang, “Near-Infrared Light-Excited Core-Core-Shell UCNP @ Au @ CdS Upconversion Nanospheres for Ultrasensitive Photoelectrochemical Enzyme Immunoassay Near-Infrared Light-Excited Core-Core-Shell UCNP @ Au @ CdS Upconversion Nanospheres for Ultrasensitive Photoel,” *Anal Chem*, 2018, doi: 10.1021/acs.analchem.8b02421.
- [201] R. M. Califf, “Biomarker definitions and their applications,” *Exp Biol Med*, vol. 243, no. 3, pp. 213–221, 2018, doi: 10.1177/1535370217750088.
- [202] R. A. Alharbi, “Proteomics approach and techniques in identification of reliable biomarkers for diseases,” *Saudi J Biol Sci*, vol. 27, no. 3, pp. 968–974, 2020, doi: 10.1016/j.sjbs.2020.01.020.
- [203] Y. Jiao, Y. Li, S. Liu, Q. Chen, and Y. Liu, “ITGA3 serves as a diagnostic and prognostic biomarker for pancreatic cancer,” *Oncotargets Ther*, vol. 12, pp. 4141–4152, 2019, doi: 10.2147/OTT.S201675.
- [204] H. Wang, T. Wu, M. Li, and Y. Tao, “Recent advances in nanomaterials for colorimetric cancer detection,” *J Mater Chem B*, vol. 9, no. 4, pp. 921–938, 2021, doi: 10.1039/d0tb02163f.
- [205] T. Sharma and M. Shah, “A comprehensive review of machine learning techniques on diabetes detection,” *Vis Comput Ind Biomed Art*, vol. 4, no. 1, 2021, doi: 10.1186/s42492-021-00097-7.

- [206] J. Rodríguez-Granger *et al.*, “Update on the Diagnosis of Sexually Transmitted Infections,” *Actas Dermosifiliogr*, vol. 111, no. 9, pp. 711–724, 2020, doi: 10.1016/j.ad.2019.05.008.
- [207] J. H. Park, D. Dehaini, J. Zhou, M. Holay, R. H. Fang, and L. Zhang, “Biomimetic nanoparticle technology for cardiovascular disease detection and treatment,” *Nanoscale Horiz*, vol. 5, no. 1, pp. 25–42, 2020, doi: 10.1039/c9nh00291j.
- [208] A. Kumar *et al.*, “Nanotheranostic Applications for Detection and Targeting Neurodegenerative Diseases,” *Front Neurosci*, vol. 14, no. April, pp. 1–11, 2020, doi: 10.3389/fnins.2020.00305.
- [209] T. M. H. Lee, “Over-the-counter biosensors: Past, present, and future,” *Sensors*, vol. 8, no. 9, pp. 5535–5559, 2008, doi: 10.3390/s8095535.
- [210] J. H. Kim *et al.*, “Technological advances in electrochemical biosensors for the detection of disease biomarkers,” *Biomed Eng Lett*, vol. 11, no. 4, pp. 309–334, 2021, doi: 10.1007/s13534-021-00204-w.
- [211] T. Bryan, X. Luo, P. R. Bueno, and J. J. Davis, “An optimised electrochemical biosensor for the label-free detection of C-reactive protein in blood,” *Biosens Bioelectron*, vol. 39, no. 1, pp. 94–98, 2013, doi: 10.1016/j.bios.2012.06.051.
- [212] J. H. Lee, K. H. Yoon, K. S. Hwang, J. Park, S. Ahn, and T. S. Kim, “Label free novel electrical detection using micromachined PZT monolithic thin film cantilever for the detection of C-reactive protein,” *Biosens Bioelectron*, vol. 20, no. 2, pp. 269–275, 2004, doi: 10.1016/j.bios.2004.01.024.
- [213] W. Bin Lee, Y. H. Chen, H. I. Lin, S. C. Shiesh, and G. Bin Lee, “An integrated microfluidic system for fast, automatic detection of C-reactive protein,” *Sens Actuators B Chem*, vol. 157, no. 2, pp. 710–721, 2011, doi: 10.1016/j.snb.2011.04.087.
- [214] H. Sohrabi *et al.*, “Recent advances of electrochemical and optical biosensors for detection of C-reactive protein as a major inflammatory biomarker,” *Microchemical Journal*, vol. 158, no. July, p. 105287, 2020, doi: 10.1016/j.microc.2020.105287.
- [215] V. Vermeeren *et al.*, “Impedimetric, diamond-based immunosensor for the detection of C-reactive protein,” *Sens Actuators B Chem*, vol. 157, no. 1, pp. 130–138, 2011, doi: 10.1016/j.snb.2011.03.037.

- [216] A. K. Yagati, J. C. Pyun, J. Min, and S. Cho, "Label-free and direct detection of C-reactive protein using reduced graphene oxide-nanoparticle hybrid impedimetric sensor," *Bioelectrochemistry*, vol. 107, pp. 37–44, 2016, doi: 10.1016/j.bioelechem.2015.10.002.
- [217] W. Wang *et al.*, "A label-free fiber optic SPR biosensor for specific detection of C-reactive protein," *Sci Rep*, vol. 7, no. 1, pp. 1–8, 2017, doi: 10.1038/s41598-017-17276-3.
- [218] M. Jarczewska, J. Rębiś, Ł. Górski, and E. Malinowska, "Development of DNA aptamer-based sensor for electrochemical detection of C-reactive protein," *Talanta*, vol. 189, no. June, pp. 45–54, 2018, doi: 10.1016/j.talanta.2018.06.035.
- [219] E. Macchia *et al.*, "Selective single-molecule analytical detection of C-reactive protein in saliva with an organic transistor," *Anal Bioanal Chem*, vol. 411, no. 19, pp. 4899–4908, 2019, doi: 10.1007/s00216-019-01778-2.
- [220] M. Algarra, D. Gomes, and J. C. G. Esteves da Silva, "Current analytical strategies for C-reactive protein quantification in blood," *Clinica Chimica Acta*, vol. 415, pp. 1–9, 2013, doi: 10.1016/j.cca.2012.09.007.
- [221] S. Balayan, N. Chauhan, W. Rosario, and U. Jain, "Biosensor development for C-reactive protein detection: A review," *Applied Surface Science Advances*, vol. 12, no. November, p. 100343, 2022, doi: 10.1016/j.apsadv.2022.100343.
- [222] X. Zhang *et al.*, "2D-porphyrinic covalent organic framework-based aptasensor with enhanced photoelectrochemical response for the detection of C-reactive protein," *Biosens Bioelectron*, vol. 129, no. January, pp. 64–71, 2019, doi: 10.1016/j.bios.2019.01.009.
- [223] M. J. Li, H. J. Wang, R. Yuan, and Y. Q. Chai, "A zirconium-based metal-organic framework sensitized by thioflavin-T for sensitive photoelectrochemical detection of C-reactive protein," *Chemical Communications*, vol. 55, no. 72, pp. 10772–10775, 2019, doi: 10.1039/c9cc05086h.
- [224] M. J. Li, H. J. Wang, R. Yuan, and Y. Q. Chai, "A sensitive label-free photoelectrochemical aptasensor based on a novel PTB7-Th/H₂O₂ system with unexpected photoelectric performance for C-reactive protein analysis," *Biosens Bioelectron*, vol. 181, no. December 2020, pp. 4–9, 2021, doi: 10.1016/j.bios.2021.113162.
- [225] M. Li, Y. Wu, J. Wang, F. Zhang, and L. Xia, "Photoelectrochemical aptasensor based on PTCDA/TiO₂ efficient sensitization effect for sensitive protein analysis," *Microchemical Journal*, vol. 193, no. April, p. 109006, 2023, doi: 10.1016/j.microc.2023.109006.

- [226] M.-J. Lu *et al.*, “Regulating Light-Sensitive Gate of Organic Photoelectrochemical Transistor toward Sensitive Biodetection at Zero Gate Bias,” *Small Struct*, vol. 2, no. 11, pp. 1–7, 2021, doi: 10.1002/sstr.202100087.
- [227] N. Zhang, Z. Y. Ma, Y. F. Ruan, W. W. Zhao, J. J. Xu, and H. Y. Chen, “Simultaneous Photoelectrochemical Immunoassay of Dual Cardiac Markers Using Specific Enzyme Tags: A Proof of Principle for Multiplexed Bioanalysis,” *Anal Chem*, vol. 88, no. 4, pp. 1990–1994, Feb. 2016, doi: 10.1021/acs.analchem.5b04579.
- [228] A. Kowalczyk, J. P. Sęk, A. Kasprzak, M. Poplawska, I. P. Grudzinski, and A. M. Nowicka, “Occlusion phenomenon of redox probe by protein as a way of voltammetric detection of non-electroactive C-reactive protein,” *Biosens Bioelectron*, vol. 117, pp. 232–239, Oct. 2018, doi: 10.1016/j.bios.2018.06.019.
- [229] M. Jarczewska, J. Rębiś, Ł. Górski, and E. Malinowska, “Development of DNA aptamer-based sensor for electrochemical detection of C-reactive protein,” *Talanta*, vol. 189, pp. 45–54, Nov. 2018, doi: 10.1016/j.talanta.2018.06.035.
- [230] H. J. Yang, M. W. Kim, C. V. Raju, C. H. Cho, T. J. Park, and J. P. Park, “Highly sensitive and label-free electrochemical detection of C-reactive protein on a peptide receptor–gold nanoparticle–black phosphorous nanocomposite modified electrode,” *Biosens Bioelectron*, vol. 234, Aug. 2023, doi: 10.1016/j.bios.2023.115382.
- [231] V. Mazzaracchio *et al.*, “Carbon-black combined with TiO₂ and KuQ as sustainable photosystem for a reliable self-powered photoelectrochemical biosensor,” *Electrochim Acta*, vol. 426, no. June, p. 140766, 2022, doi: 10.1016/j.electacta.2022.140766.
- [232] Y. Liu, S. Ai, R. Yuan, and H. Liu, “Defective Se-doped In₂S₃ nanomaterial-based photoelectrochemical biosensor for the ultrasensitive detection of chloramphenicol,” *Sens Actuators B Chem*, vol. 373, no. July, p. 132705, 2022, doi: 10.1016/j.snb.2022.132705.
- [233] H. Du, Y. Xue, C. Wang, and G. Jie, “ZnIn₂S₄ QDs@TiO₂ nanosphere-BiOI double heterojunction combined with unique tripod DNA walker amplification for photoelectrochemical biosensing of microRNA-21,” *Sens Actuators B Chem*, vol. 373, no. August, p. 132704, 2022, doi: 10.1016/j.snb.2022.132704.
- [234] Y. Zheng, Y. Zhou, X. Cui, H. Yin, and S. Ai, “Enhanced photoactivity of CdS nanorods by MXene and ZnSnO₃: Application in photoelectrochemical biosensor for the effect of

- environmental pollutants on DNA hydroxymethylation in wheat tissues,” *Mater Today Chem*, vol. 24, p. 100878, 2022, doi: 10.1016/j.mtchem.2022.100878.
- [235] S. Liu, H. Dong, F. Jiang, Y. Li, and Q. Wei, “Self-powered photoelectrochemical biosensor with inherent potential for charge carriers drive,” *Biosens Bioelectron*, vol. 211, no. April, p. 114361, 2022, doi: 10.1016/j.bios.2022.114361.
- [236] S. A. Shabbir, A. Imran, M. G. B. Ashiq, H. Latif, K. Javed, and M. Munam, “Photoelectrochemical response of non-enzymatic glucose biosensing for graphene, carbon nanotubes and BiVO₄ nanocomposites,” *Journal of Materials Science: Materials in Electronics*, vol. 32, no. 13, pp. 17741–17751, 2021, doi: 10.1007/s10854-021-06310-w.
- [237] W. Yang *et al.*, “Photoelectrochemical Glucose Biosensor Based on the Heterogeneous Facets of Nanocrystalline TiO₂/Au/Glucose Oxidase Films,” *ACS Appl Nano Mater*, vol. 3, no. 3, pp. 2723–2732, 2020, doi: 10.1021/acsanm.0c00086.
- [238] A. Scott, S. Sakib, S. Saha, I. Zhitomirsky, and L. Soleymani, “A portable and smartphone-operated photoelectrochemical reader for point-of-care biosensing,” *Electrochim Acta*, vol. 419, no. April, p. 140347, 2022, doi: 10.1016/j.electacta.2022.140347.
- [239] N. Barnawi, S. Allehyani, and R. Seoudi, “Biosynthesis and characterization of gold nanoparticles and its application in eliminating nickel from water,” *Journal of Materials Research and Technology*, vol. 17, pp. 537–545, 2022, doi: 10.1016/j.jmrt.2021.12.013.
- [240] Z. H. Jabbar *et al.*, “A review study summarizes the main characterization techniques of nano-composite photocatalysts and their applications in photodegradation of organic pollutants,” *Environ Nanotechnol Monit Manag*, vol. 19, no. November 2022, p. 100765, 2023, doi: 10.1016/j.enmm.2022.100765.
- [241] L. Ruzik, “Microalgae with active biological metal-nanoparticles as a novel food. Biosynthesis, characterization and bioavailability investigation – Review,” *Trends Food Sci Technol*, vol. 139, no. August, p. 104127, 2023, doi: 10.1016/j.tifs.2023.104127.
- [242] Y. L. Liu, Y. C. Zhu, L. B. Qu, R. Yang, X. D. Yu, and W. W. Zhao, “Unique Redox Reaction between CuO Photocathode and Cysteine: Insight into the Mechanism for Cathodic Photoelectrochemical Bioanalysis,” *ACS Appl Bio Mater*, vol. 2, no. 7, pp. 2703–2707, 2019, doi: 10.1021/acsabm.9b00428.
- [243] H. H. Wang, M. J. Li, H. J. Wang, Y. Q. Chai, and R. Yuan, “P-n-sensitized heterostructure Co₃O₄/Fullerene with highly efficient photoelectrochemical performance for ultrasensitive

- DNA detection,” *ACS Appl Mater Interfaces*, vol. 11, no. 26, pp. 23765–23772, 2019, doi: 10.1021/acsami.9b05923.
- [244] F. Cao *et al.*, “Enhanced Photoelectrochemical Performance from Rationally Designed Anatase/Rutile TiO₂ Heterostructures,” *ACS Appl Mater Interfaces*, vol. 8, no. 19, pp. 12239–12245, 2016, doi: 10.1021/acsami.6b03842.
- [245] Q. Y. Wei *et al.*, “Surface State Passivation Ignited Photoelectrochemical Sensing of Thallium(I) with Ultrathin In₂S₃ Nanosheets,” *ACS Appl Electron Mater*, vol. 3, no. 6, pp. 2490–2496, 2021, doi: 10.1021/acsaelm.1c00338.
- [246] Z. Zhang, C. Zhang, H. Zheng, and H. Xu, “Plasmon-Driven Catalysis on Molecules and Nanomaterials,” *Acc Chem Res*, vol. 52, no. 9, pp. 2506–2515, 2019, doi: 10.1021/acs.accounts.9b00224.
- [247] A. Agrawal, S. H. Cho, O. Zandi, S. Ghosh, R. W. Johns, and D. J. Milliron, “Localized Surface Plasmon Resonance in Semiconductor Nanocrystals,” *Chem Rev*, vol. 118, no. 6, pp. 3121–3207, 2018, doi: 10.1021/acs.chemrev.7b00613.
- [248] K. M. Mayer and J. H. Hafner, “Localized surface plasmon resonance sensors,” *Chem Rev*, vol. 111, no. 6, pp. 3828–3857, 2011, doi: 10.1021/cr100313v.
- [249] V. Saraswat, R. M. Jacobberger, and M. S. Arnold, “Materials Science Challenges to Graphene Nanoribbon Electronics,” *ACS Nano*, vol. 15, no. 3, pp. 3674–3708, 2021, doi: 10.1021/acsnano.0c07835.
- [250] S. Fiechter and N. Chopra, “Energy conversion and storage,” *Nanomaterials and Energy*, vol. 1, no. 2, pp. 63–64, 2012, doi: 10.1680/nme.12.00005.
- [251] M. Li, T. Chen, J. J. Gooding, and J. Liu, “Review of carbon and graphene quantum dots for sensing,” *ACS Sens*, vol. 4, no. 7, pp. 1732–1748, 2019, doi: 10.1021/acssensors.9b00514.
- [252] M. Jablan, M. Soljačić, and H. Buljan, “Plasmons in graphene: Fundamental properties and potential applications,” *Proceedings of the IEEE*, vol. 101, no. 7, pp. 1689–1704, 2013, doi: 10.1109/JPROC.2013.2260115.
- [253] M. S. Ukhtary and R. Saito, “Surface plasmon in graphene and carbon nanotubes,” *Carbon N Y*, vol. 167, pp. 455–474, 2020, doi: 10.1016/j.carbon.2020.05.019.
- [254] A. N. Grigorenko, M. Polini, and K. S. Novoselov, “Graphene plasmonics,” *Nat Photonics*, vol. 6, no. 11, pp. 749–758, 2012, doi: 10.1038/nphoton.2012.262.

- [255] I. B. Becerril-Castro *et al.*, “Gold Nanostars: Synthesis, Optical and SERS Analytical Properties,” *Analysis and Sensing*, vol. 2, no. 3, 2022, doi: 10.1002/anse.202200005.
- [256] L. Shao, A. S. Susa, L. S. Cheung, T. K. Sau, A. L. Rogach, and J. Wang, “Plasmonic properties of single multispiked gold nanostars: Correlating modeling with experiments,” *Langmuir*, vol. 28, no. 24, pp. 8979–8984, 2012, doi: 10.1021/la2048097.
- [257] Y. Liu *et al.*, “Plasmonic gold nanostars for synergistic photoimmunotherapy to treat cancer,” *Nanophotonics*, vol. 10, no. 12, pp. 3295–3302, 2021, doi: 10.1515/nanoph-2021-0237.
- [258] M. Serhan *et al.*, “Green synthesis, photocatalytic and photoelectrochemical performance of Au-graphene nanocomposite,” in *AICHE Annual Meeting, Conference Proceedings*, American Institute of Chemical Engineers, 2019. doi: 10.1039/x0xx00000x.
- [259] Y. Hu, Z. Xue, H. He, R. Ai, X. Liu, and X. Lu, “Photoelectrochemical sensing for hydroquinone based on porphyrin-functionalized Au nanoparticles on graphene,” *Biosens Bioelectron*, vol. 47, pp. 45–49, Sep. 2013, doi: 10.1016/j.bios.2013.02.034.
- [260] C. Ehrling, S. D. Wolf, and J. G. Bode, “Acute-phase protein synthesis: A key feature of innate immune functions of the liver,” *Biol Chem*, vol. 402, no. 9, pp. 1129–1145, 2021, doi: 10.1515/hsz-2021-0209.
- [261] P. C. N. A. Calder, B. Brouns, FredBuetler, TimoClement, KarineCunningham, KarenEsposito, KatherineJönsson, Lena S.Kolb, HubertLansink, MirianMarcos, AscensionMargioris, AndrewMatusheski, NathanNordmann, HerveO’Brien, JohnPugliese, GiuseppeRizkalla, SalwaSchalkwijk, CasperTuomi, and B. M. Winklhofer-Roob, “Dietary factors and low-grade inflammation in relation to overweight and obesity revisited,” *British Journal of Nutrition*, vol. 127, no. 10, pp. 1455–1457, 2022, doi: 10.1017/S0007114522000782.
- [262] D. Khanna, S. Khanna, P. Khanna, P. Kahar, and B. M. Patel, “Obesity: A Chronic Low-Grade Inflammation and Its Markers,” *Cureus*, vol. 14, no. 2, 2022, doi: 10.7759/cureus.22711.
- [263] E. C. Vreeland *et al.*, “Enhanced Nanoparticle Size Control by Extending LaMer’s Mechanism,” *Chemistry of Materials*, vol. 27, pp. 6059–6066, 2015, doi: 10.1021/acs.chemmater.5b02510.

- [264] Y. J. Hwang *et al.*, “Morphology Control of Au–Ni Hybrid Nanoparticles: Exploring Heterostructures and Optical Tuning,” *Inorg Chem*, 2024, doi: 10.1021/acs.inorgchem.4c01089.
- [265] B. V. Enüstün and J. Turkevich, “Coagulation of Colloidal Gold,” *J Am Chem Soc*, vol. 85, no. 21, pp. 3317–3328, 1963, doi: 10.1021/ja00904a001.
- [266] A. F. Cruz-Pacheco, Y. Monsalve, Y. Serrano-Rivero, J. Salazar-Uribe, E. Moreno, and J. Orozco, “Engineered synthetic nanobody-based biosensors for electrochemical detection of epidermal growth factor receptor,” *Chemical Engineering Journal*, vol. 465, no. March, 2023, doi: 10.1016/j.cej.2023.142941.
- [267] H. Yuan, C. G. Khoury, H. Hwang, C. M. Wilson, G. A. Grant, and T. Vo-Dinh, “Gold nanostars: Surfactant-free synthesis, 3D modelling, and two-photon photoluminescence imaging,” *Nanotechnology*, vol. 23, no. 7, Feb. 2012, doi: 10.1088/0957-4484/23/7/075102.
- [268] L. Osinkina, T. Lohmüller, F. Jäckel, and J. Feldmann, “Synthesis of gold nanostar arrays as reliable, large-scale, homogeneous substrates for surface-enhanced Raman scattering imaging and spectroscopy,” *Journal of Physical Chemistry C*, vol. 117, no. 43, pp. 22198–22202, 2013, doi: 10.1021/jp312149d.
- [269] Y. Pu, Y. Zhao, P. Zheng, and M. Li, “Elucidating the Growth Mechanism of Plasmonic Gold Nanostars with Tunable Optical and Photothermal Properties,” *Inorg Chem*, vol. 57, no. 14, pp. 8599–8607, 2018, doi: 10.1021/acs.inorgchem.8b01354.
- [270] S. Barbosa *et al.*, “Targeted Combinatorial Therapy Using Gold Nanostars as Theranostic Platforms,” *Journal of Physical Chemistry C*, vol. 118, no. 45, pp. 26313–26323, 2014, doi: 10.1021/jp505979e.
- [271] S. He *et al.*, “Quantitative and Label-Free Detection of Protein Kinase A Activity Based on Surface-Enhanced Raman Spectroscopy with Gold Nanostars,” *Anal Chem*, vol. 90, no. 10, pp. 6071–6080, May 2018, doi: 10.1021/acs.analchem.7b05417.
- [272] S. Barbosa *et al.*, “Tuning size and sensing properties in colloidal gold nanostars,” *Langmuir*, vol. 26, no. 18, pp. 14943–14950, 2010, doi: 10.1021/la102559e.
- [273] S. Gražulis, A. Merkys, and A. Vaitkus, “Crystallography Open Database (COD),” *Handbook of Materials Modeling*, pp. 1863–1881, 2020, doi: 10.1007/978-3-319-44677-6_66.

- [274] H. L. Wu, C. H. Chen, and M. H. Huang, "Seed-mediated synthesis of branched gold nanocrystals derived from the side growth of pentagonal bipyramids and the formation of gold nanostars," *Chemistry of Materials*, vol. 21, no. 1, pp. 110–114, 2009, doi: 10.1021/cm802257e.
- [275] P. Senthil Kumar, I. Pastoriza-Santos, B. Rodríguez-González, F. Javier García De Abajo, and L. M. Liz-Marzán, "High-yield synthesis and optical response of gold nanostars," *Nanotechnology*, vol. 19, no. 1, pp. 1–7, 2008, doi: 10.1088/0957-4484/19/01/015606.
- [276] L. Rodríguez-Lorenzo, J. M. Romo-Herrera, J. Pérez-Juste, R. A. Alvarez-Puebla, and L. M. Liz-Marzán, "Reshaping and LSPR tuning of Au nanostars in the presence of CTAB," *J Mater Chem*, vol. 21, no. 31, pp. 11544–11549, 2011, doi: 10.1039/c1jm10603a.
- [277] Y. Zhang *et al.*, "Plasmon-driven photocatalytic properties based on the surface of gold nanostar particles," *Spectrochim Acta A Mol Biomol Spectrosc*, vol. 264, p. 120240, 2022, doi: 10.1016/j.saa.2021.120240.
- [278] R. T. Kachoosangi and R. G. Compton, "A simple electroanalytical methodology for the simultaneous determination of dopamine, serotonin and ascorbic acid using an unmodified edge plane pyrolytic graphite electrode," *Anal Bioanal Chem*, vol. 387, no. 8, pp. 2793–2800, 2007, doi: 10.1007/s00216-007-1129-y.
- [279] M. Velický, P. S. Toth, C. R. Woods, K. S. Novoselov, and R. A. W. Dryfe, "Electrochemistry of the Basal Plane versus Edge Plane of Graphite Revisited," *Journal of Physical Chemistry C*, vol. 123, no. 18, pp. 11677–11685, 2019, doi: 10.1021/acs.jpcc.9b01010.
- [280] Q. Guo, C. Li, B. Deng, S. Yuan, F. Guinea, and F. Xia, "Infrared Nanophotonics Based on Graphene Plasmonics," Dec. 20, 2017, *American Chemical Society*. doi: 10.1021/acsp Photonics.7b00547.
- [281] X. Ji, C. E. Banks, W. Xi, S. J. Wilkins, and R. G. Compton, "Edge plane sites on highly ordered pyrolytic graphite as templates for making palladium nanowires via electrochemical decoration," *Journal of Physical Chemistry B*, vol. 110, no. 45, pp. 22306–22309, 2006, doi: 10.1021/jp065776m.
- [282] M. Lakshmanakumar *et al.*, "Fabrication of GQD-Electrodeposited Screen-Printed Carbon Electrodes for the Detection of the CRP Biomarker," *ACS Omega*, vol. 6, pp. 32528–32536, 2021, doi: 10.1021/acsomega.1c04043.

- [283] S. J. Goldie, S. Bush, J. A. Cumming, and K. S. Coleman, “A Statistical Approach to Raman Analysis of Graphene-Related Materials: Implications for Quality Control,” *ACS Appl Nano Mater*, vol. 3, no. 11, pp. 11229–11239, 2020, doi: 10.1021/acsanm.0c02361.
- [284] J. Wang, F. Ma, W. Liang, R. Wang, and M. Sun, “Optical, photonic and optoelectronic properties of graphene, h-NB and their hybrid materials,” *Nanophotonics*, vol. 6, no. 5, pp. 943–976, 2017, doi: 10.1515/nanoph-2017-0015.
- [285] X. Luo, T. Qiu, W. Lu, and Z. Ni, “Plasmons in graphene: Recent progress and applications,” *Materials Science and Engineering R: Reports*, vol. 74, no. 11, pp. 351–376, 2013, doi: 10.1016/j.mser.2013.09.001.
- [286] A. Adán-Más and D. Wei, “Photoelectrochemical properties of graphene and its derivatives,” *Nanomaterials*, vol. 3, no. 3, pp. 325–356, 2013, doi: 10.3390/nano3030325.
- [287] H. Wang, Y. Pu, B. Shan, and M. Li, “Combining Experiments and Theoretical Modeling to Interrogate the Anisotropic Growth and Structure-Plasmonic Property Relationships of Gold Nanostars,” *Inorg Chem*, vol. 58, no. 18, pp. 12457–12466, 2019, doi: 10.1021/acs.inorgchem.9b02187.
- [288] D. Echeverri and J. Orozco, “ β -1,4-Galactosyltransferase-V colorectal cancer biomarker immunosensor with label-free electrochemical detection,” *Talanta*, vol. 243, no. December 2021, p. 123337, 2022, doi: 10.1016/j.talanta.2022.123337.
- [289] A. F. Cruz-Pacheco, J. Quinchia, and J. Orozco, “Cerium oxide-doped PEDOT nanocomposite for label-free electrochemical immunosensing of anti-p53 autoantibodies,” *Microchimica Acta*, vol. 189, no. 6, 2022, doi: 10.1007/s00604-022-05322-5.
- [290] A. F. Cruz-Pacheco, J. Quinchia, and J. Orozco, “Nanostructured poly(thiophene acetic acid)/Au/poly(methylene blue) interface for electrochemical immunosensing of p53 protein,” *Microchimica Acta*, vol. 190, no. 4, 2023, doi: 10.1007/s00604-023-05683-5.
- [291] E. Nagao and J. A. Dvorak, “Phase imaging by atomic force microscopy: Analysis of living homoiothermic vertebrate cells,” *Biophys J*, vol. 76, no. 6, pp. 3289–3297, 1999, doi: 10.1016/S0006-3495(99)77481-3.
- [292] D. S. Jakob, H. Wang, and X. G. Xu, “Pulsed Force Kelvin Probe Force Microscopy,” *ACS Nano*, vol. 14, no. 4, pp. 4839–4848, 2020, doi: 10.1021/acsnano.0c00767.
- [293] A. Zahmatkeshsaredorahi, D. S. Jakob, and X. G. Xu, “Pulsed Force Kelvin Probe Force Microscopy—A New Type of Kelvin Probe Force Microscopy under Ambient Conditions,”

- Journal of Physical Chemistry C*, vol. 128, no. 24, pp. 9813–9827, 2024, doi: 10.1021/acs.jpcc.4c01461.
- [294] A. Liscio, V. Palermo, and P. Samorì, “Nanoscale Quantitative Measurement of the Potential of Charged Nanostructures by Electrostatic and Kelvin Probe Force Microscopy: Unraveling Electronic Processes in Complex Materials,” *Acc Chem Res*, vol. 43, no. 4, pp. 541–550, Apr. 2010, doi: 10.1021/ar900247p.
- [295] S. Hormeño, M. Penedo, C. V. Manzano, and M. Luna, “Gold nanoparticle coated silicon tips for Kelvin probe force microscopy in air,” *Nanotechnology*, vol. 24, no. 39, Oct. 2013, doi: 10.1088/0957-4484/24/39/395701.
- [296] P. Bertoncello, I. Ciani, L. Fei, and P. R. Unwin, “Measurement of apparent diffusion coefficients within ultrathin nation langmuir-schaefer films: Comparison of a novel scanning electrochemical microscopy approach with cyclic voltammetry,” *Langmuir*, vol. 22, no. 25, pp. 10380–10388, Dec. 2006, doi: 10.1021/la061214i.
- [297] D. R. Baker, R. F. Simmerman, J. J. Sumner, B. D. Bruce, and C. A. Lundgren, “Photoelectrochemistry of photosystem I bound in Nafion,” *Langmuir*, vol. 30, no. 45, pp. 13650–13655, Nov. 2014, doi: 10.1021/la503132h.
- [298] D. Soto, M. Alzate, J. Gallego, and J. Orozco, “Electroanalysis of an Iron@Graphene-Carbon Nanotube Hybrid Material,” *Electroanalysis*, vol. 30, no. 7, pp. 1521–1528, 2018, doi: 10.1002/elan.201800115.
- [299] J. Quinchia *et al.*, “Disposable electrochemical immunoplatfrom to shed light on the role of the multifunctional glycoprotein TIM-1 in cancer cells invasion,” *Talanta*, vol. 267, no. August 2023, pp. 125–152, 2024, doi: 10.1016/j.talanta.2023.125155.
- [300] X. M. T. Nguyen, J. Lane, B. R. Smith, and N. T. Nguyen, “Changes in inflammatory biomarkers across weight classes in a representative US population: A link between obesity and inflammation,” *Journal of Gastrointestinal Surgery*, vol. 13, no. 7, pp. 1205–1212, 2009, doi: 10.1007/s11605-009-0904-9.
- [301] J. Choi, L. Joseph, and L. Pilote, “Obesity and C-reactive protein in various populations: A systematic review and meta-analysis,” *Obesity Reviews*, vol. 14, no. 3, pp. 232–244, 2013, doi: 10.1111/obr.12003.

- [302] M. A. Mansournia, R. Waters, M. Nazemipour, M. Bland, and D. G. Altman, "Bland-Altman methods for comparing methods of measurement and response to criticisms," *Glob Epidemiol*, vol. 3, Nov. 2021, doi: 10.1016/j.gloepi.2020.100045.
- [303] M. Hussein *et al.*, "Comparison of Adiposomal Lipids between Obese and Non-Obese Individuals," *Metabolites*, vol. 14, no. 8, Aug. 2024, doi: 10.3390/metabo14080464.

ANNEX 1

SUPPLEMENTARY INFORMATION CHAPTER III

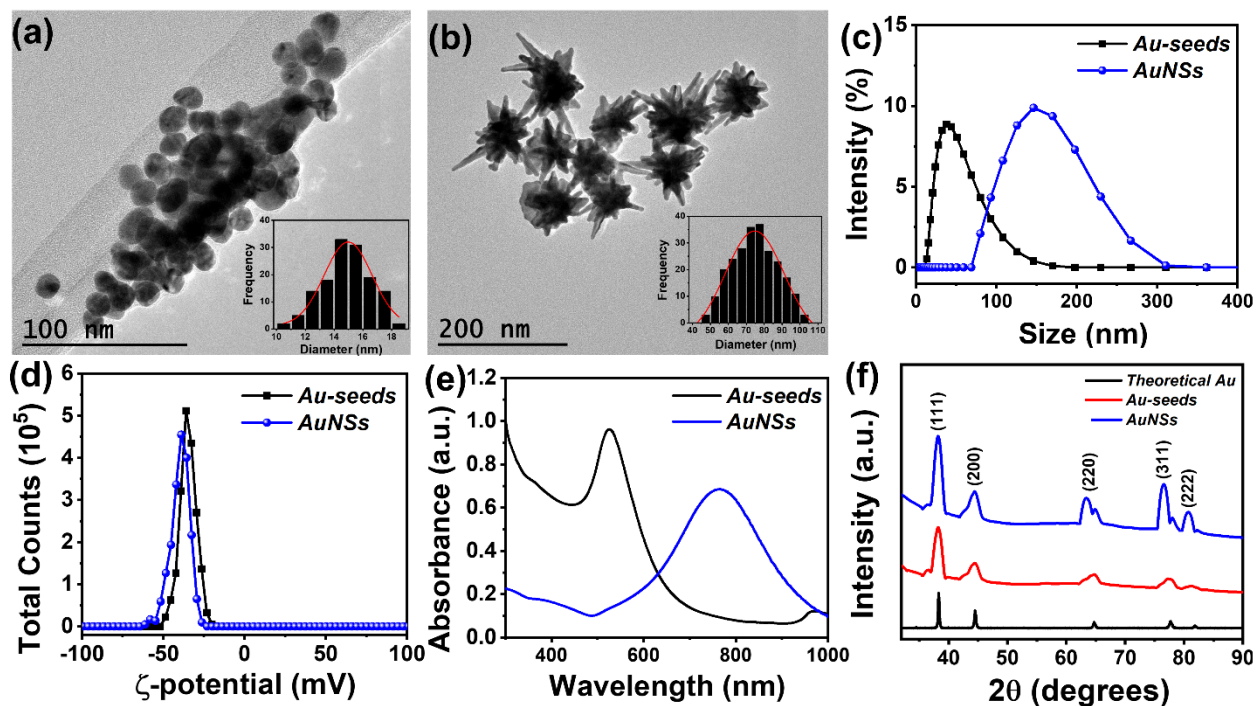


Figure S1. (a) Au-seeds, and (b) AuNSs TEM images. (c) DLS, (d) ELS, (e) UV-vis absorption, and (f) XRD pattern with a theoretical gold insert of Au-seeds and AuNSs, respectively.

Table S1. Theoretical data of the crystalline properties in gold nanomaterials.

Plane	2θ	d-spacing (Å)
(111)	38.28	2.36
(200)	44.48	2.04
(220)	64.63	1.44
(311)	77.76	1.23
(222)	81.93	1.17

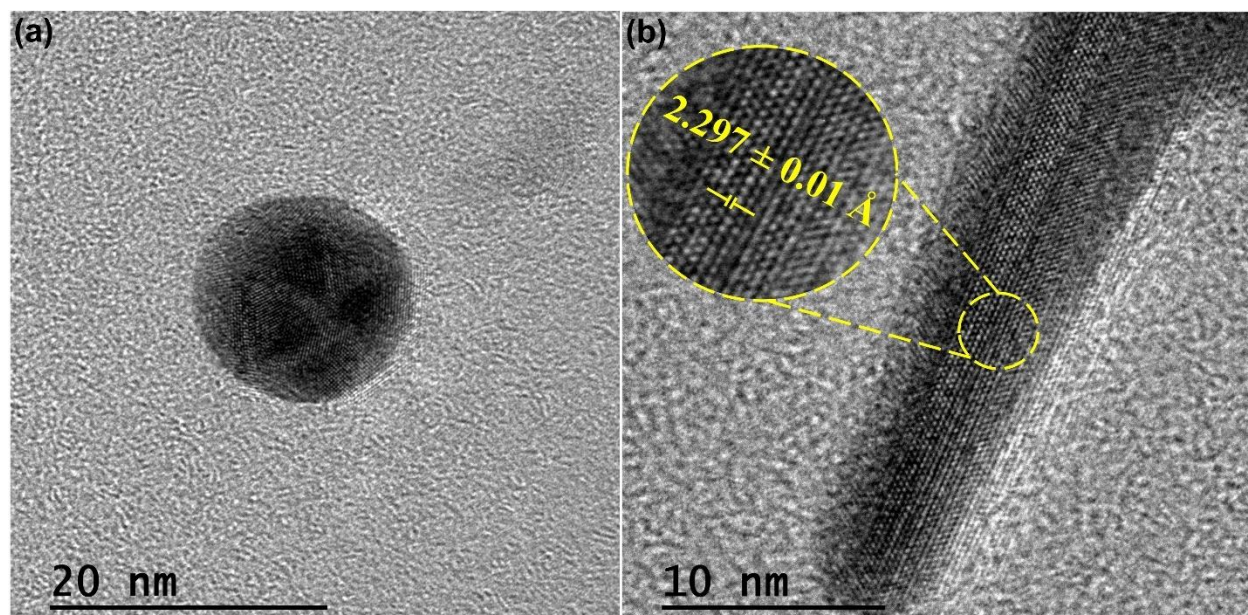


Figure S2. HRTEM images of (a) Au-seeds and (b) one tip in the AuNSs where the *d*-spacing was measured.

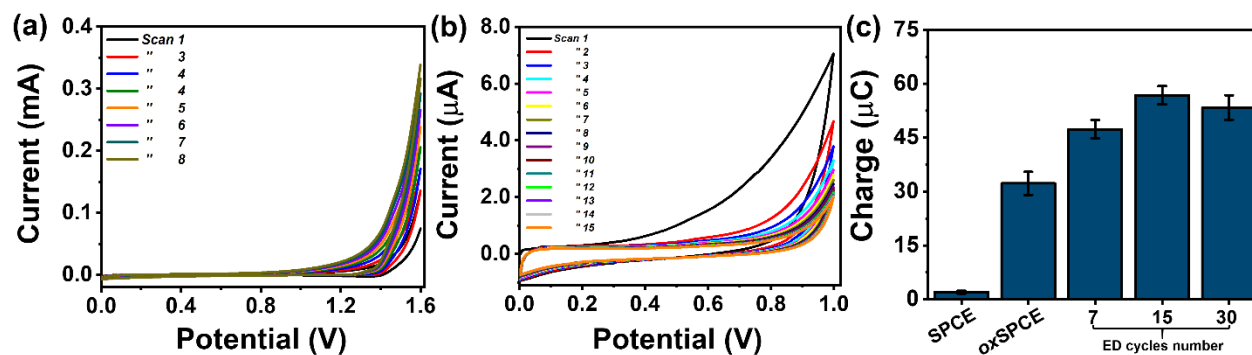


Figure S3. (a) Electrochemical pretreatment of the SPCE surface in 0.1 M H₂SO₄ by CV at + 1.6 – 0.0 V and scan rate of 0.1 V/s. (b) Electrochemical deposition (ED) of synthesized AuNSs by CV at 0.0 to 1.0 V, a scan rate of 0.05 V/s, during 15 cycles. (c) Optimization of the AuNSs ED process based on the number of cycles and the charge achieved during the PEC process in a 1X PBS (pH 7.4) solution containing 0.01 M AA as an electron donor.

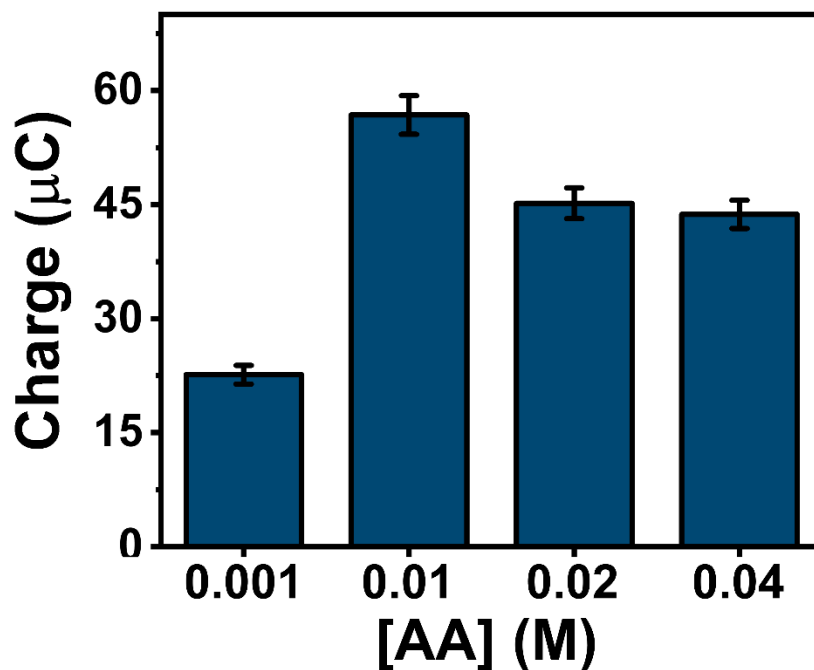


Figure S4. Optimization of AA concentration in AuNSs/oxSPCE nanocomposite in PEC process in a 1X PBS (pH 7.4) solution containing 0.01M AA as an electron donor.

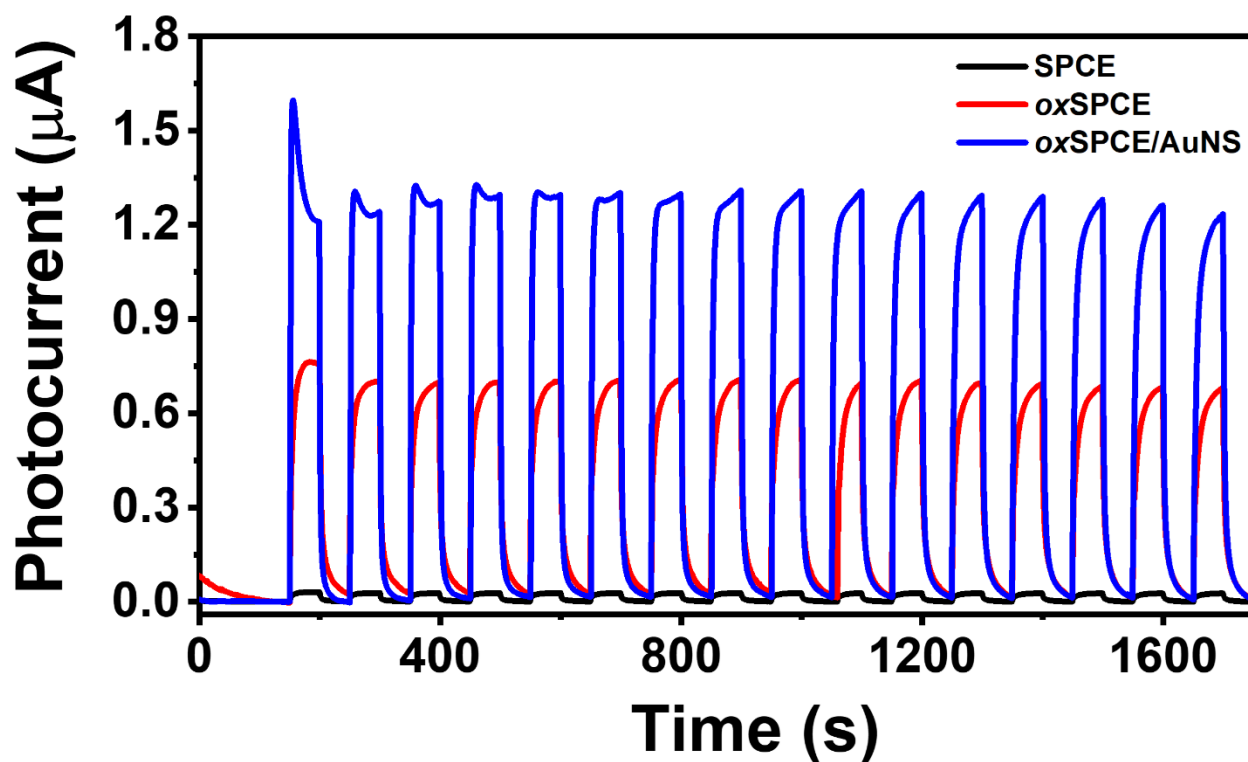


Figure S5. PEC performance of each AuNSs/oxSPCE nanocomposite step over 15 repetitions of on/off light in a 1X PBS (pH 7.4) solution containing 0.01M AA.

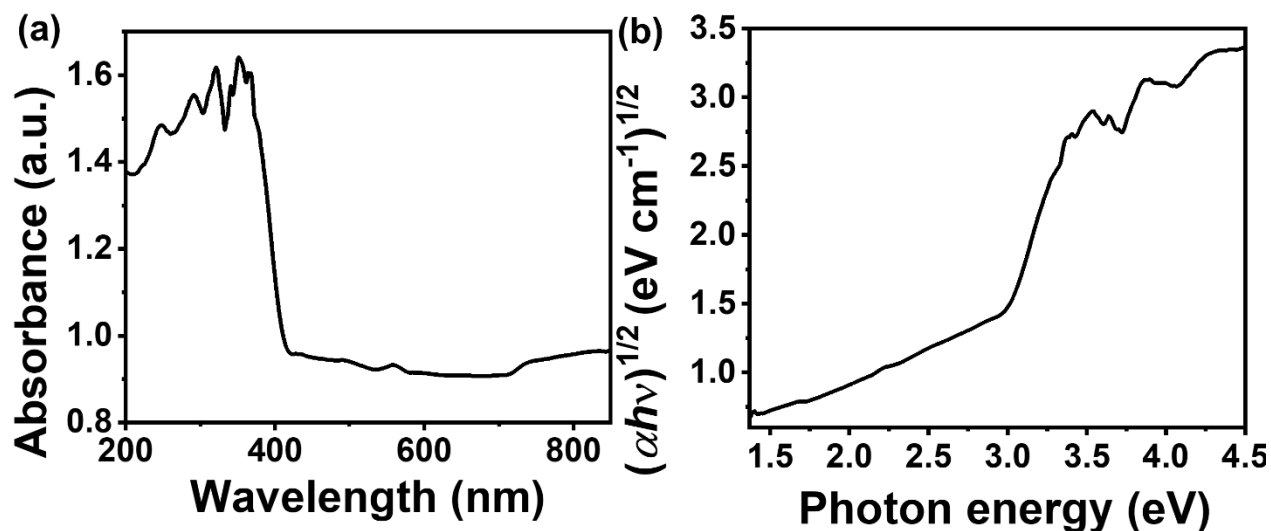


Figure S6. (a) UV-vis-DRS and (b) Tauc plot of the oxSPCE electrochemical pretreated surface.

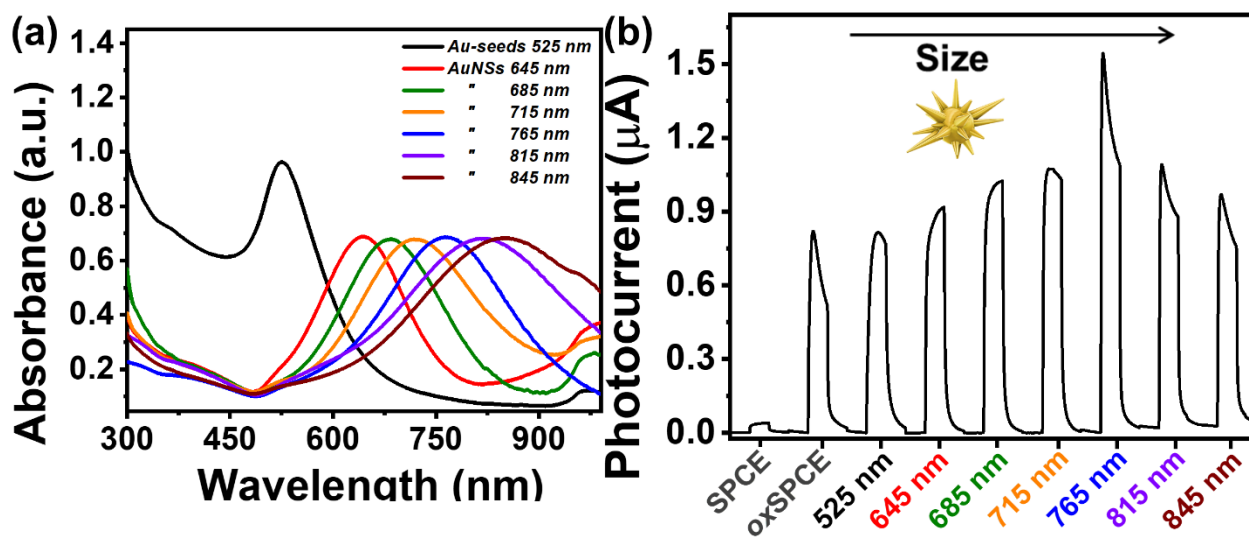


Figure S7. (a) UV-vis absorption spectrum of Au-seeds, several synthesis batches of AuNSs, and (b) the respective PEC performance of AuNSs/oxSPCE nanocomposites.

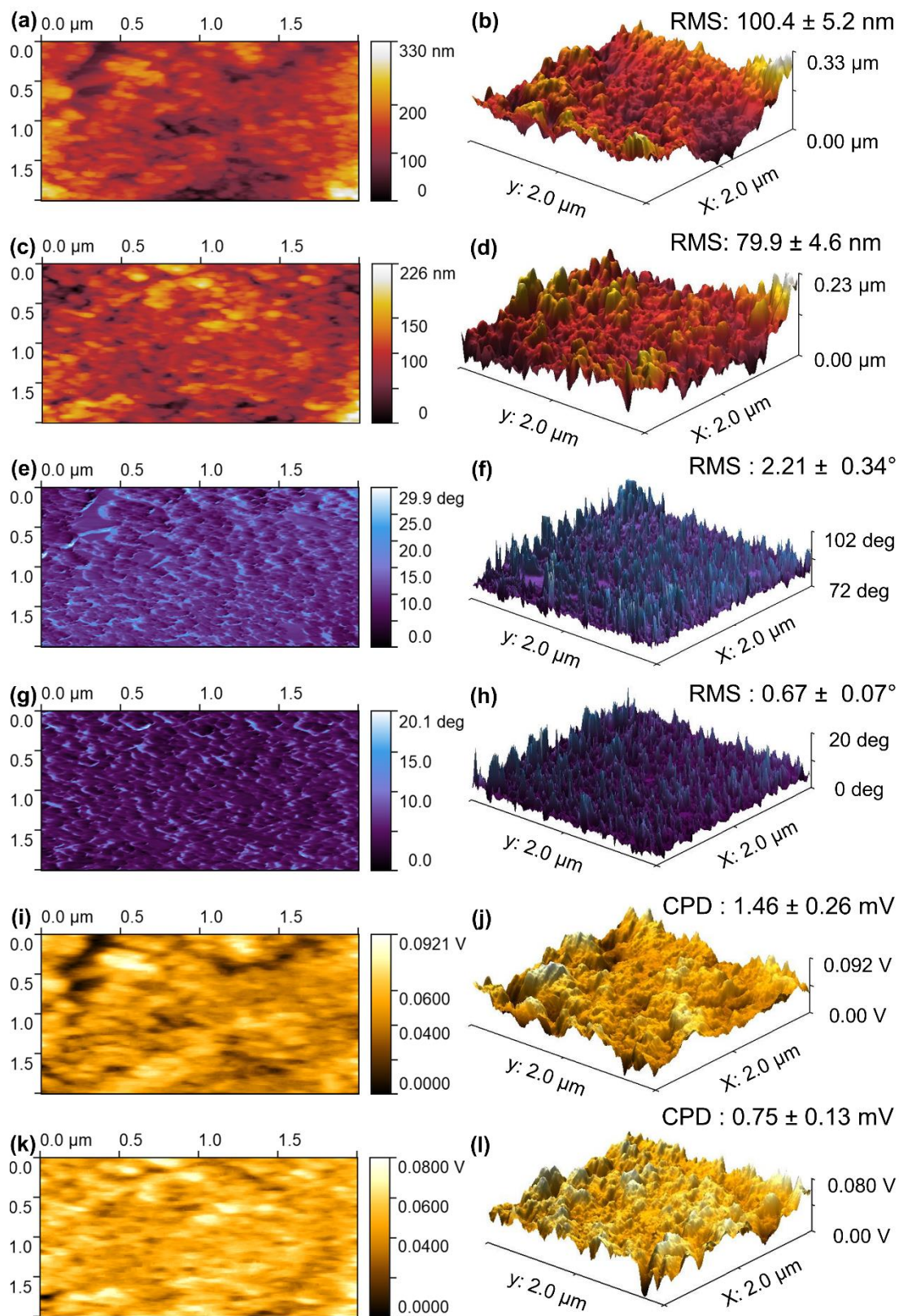


Figure S8. AFM of the (a-b, e-f, i-j) oxSPCE and (c-d, g-h, k-l) AuNSs/oxSPCE nanocomposite in (a-d) height, (e-h) phase, and (i-l) potential mode.

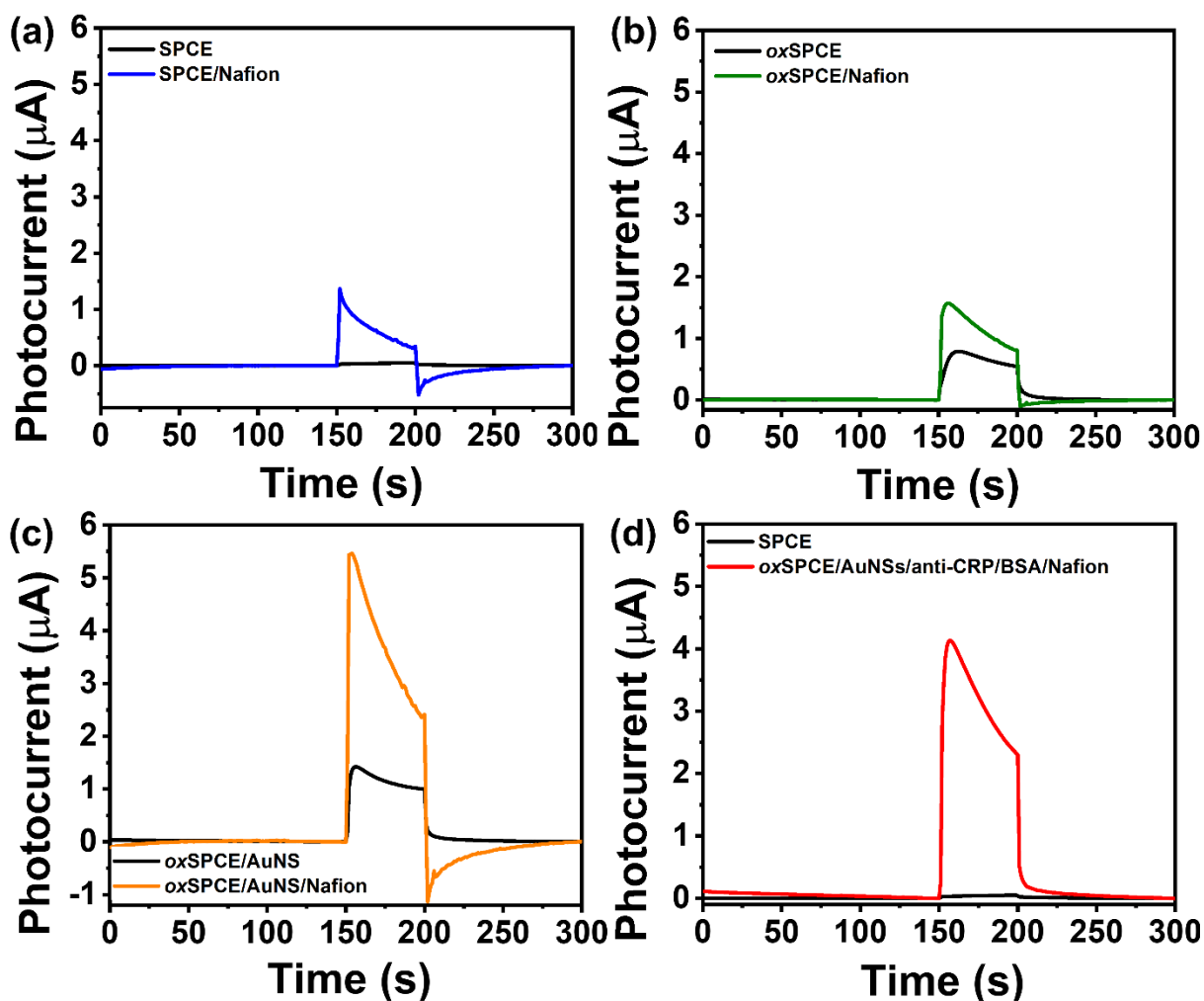


Figure S9. PEC behavior of the Nafion membrane in the (a) bare SPCE, the (b) bare oxSPCE surface, the (c) bare AuNSs/oxSPCE surface, and (d) the nano-immunosensor assembly.

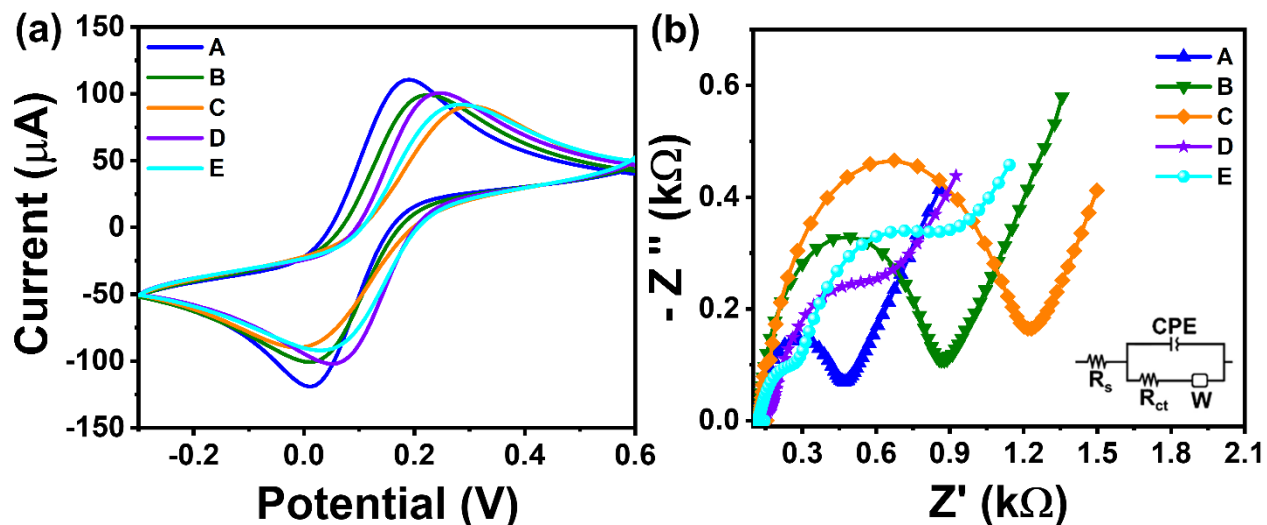


Figure S10. (a) CV at 0.05 V/s, and (b) EIS from 50000 to 0.05 Hz, at the formal potential of 0.125 V, and amplitude 0.01 V of the nano-immunosensor assembly in a 1X PBS (pH 7.4) solution containing 5 mM $[Fe(CN)_6]^{4-/3-}$. A: AuNSs/oxSPCE, B: 50 μ g/mL of anti-CRP, C: 1% BSA, D: 1 % Nafion, and E: 0.8 ng/mL CRP.

Table S2. Data from the electrochemical characterization of the SPCEs with pretreatment oxSPCE, AuNSs/oxSPCE, anti-CRP/AuNSs/oxSPCE, BSA/anti-CRP/AuNSs/oxSPCE, Nafion/BSA/anti-CRP/AuNSs/oxSPCE, and CRP/Nafion/BSA/anti-CRP/AuNSs/oxSPCE interfaces by CV and EIS ($n = 5$). Electroactive surface area at the different steps of the modification of the SPCE, calculated from the CV scans performed in 5 mM $[Fe(CN)_6]^{4-/3-}$ equimolar redox probe in 1X PBS solution at a scan rate of 50 mV/s: anodic electroactive area (A_a), cathodic electroactive area (A_c), average electroactive area (A_e) and anodic and cathodic peak separation (ΔE_p). Data from EIS experiments: Charge-transfer resistance (R_{ct}), electrolytic solution resistance (R_s), the Warburg impedance (Z_w), constant phase element (CPE) with pre-exponential factor (P), and exponent (n).

	A_a (mm^2)	A_c (mm^2)	A_e (mm^2)	ΔE_p (mV)	R_{ct} (Ω)	R_s (Ω)	Z_w (Ω)	CPE	
								P ($\mu F S^{n-1}$)	n
SPCE	14.4 \pm 0.2	14.6 \pm 0.2	14.5	220	562.7 \pm 33.9	128.4 \pm 2.6	237.2	1.1	0.9
oxSPCE	11.6 \pm 0.2	11.6 \pm 0.3	11.6	232	753.5 \pm 2.9	127.3 \pm 3.0	227.9	8.6	0.9
oxSPCE/ AuNSs	15.6 \pm 0.1	16.2 \pm 0.2	15.9	173	299.3 \pm 19.1	125.8 \pm 2.6	234.9	10.7	0.9
Anti-CRP	13.4 \pm 0.1	13.4 \pm 0.3	13.4	196	723.9 \pm 24.3	100.4 \pm 0.5	236.5	1.7	0.9
BSA	11.2 \pm 0.2	11.0 \pm 0.1	11.1	280	1039.3 \pm 25.2	131.3 \pm 1.4	235.9	10.2	0.9
Nafion	13.5 \pm 0.3	13.6 \pm 0.2	13.6	173	48.6 \pm 7.3 417.6 \pm 12.2	128.8 \pm 3.9	226.2	29.7 325.0	0.9 0.8
CRP	11.9 \pm 0.1	11.6 \pm 0.1	11.8	230	192.9 \pm 0.3 512.6 \pm 5.8	126.6 \pm 4.8	236.6	68.5 348.0	0.8 0.9

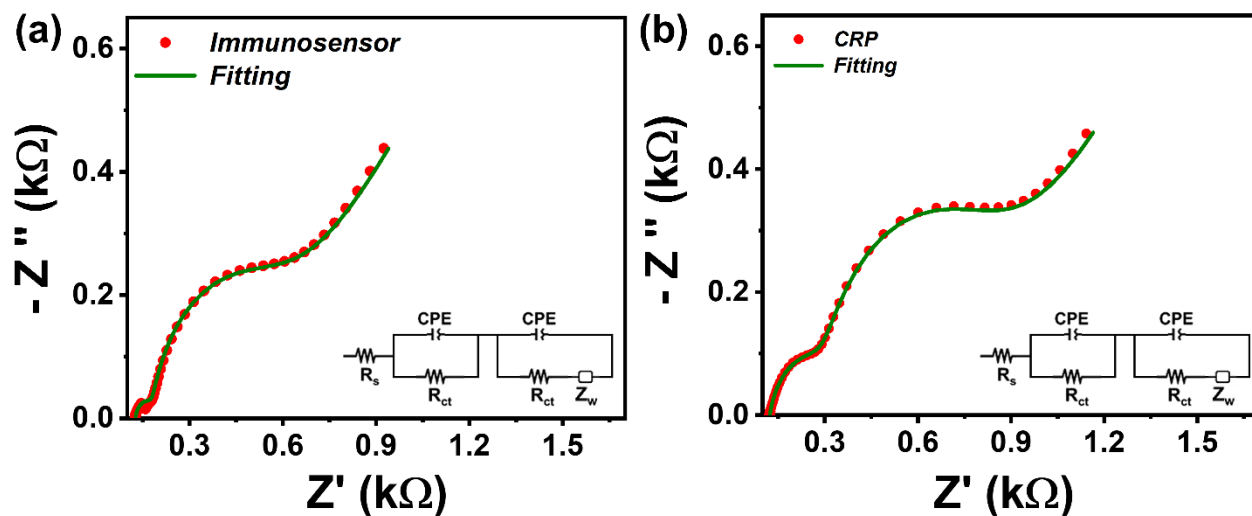


Figure S11. (a) *Nafion/BSA/Anti-CRP/AuNSs/oxSPCE nanobiocomposite* and (b) *the detection of CRP (0.8 ng/mL) using EIS fitting in the EISpectrum analyzer software in a 1X PBS (pH 7.4) solution containing 5 mM $K_3[Fe(CN)_6]/K_4[Fe(CN)_6]$.*

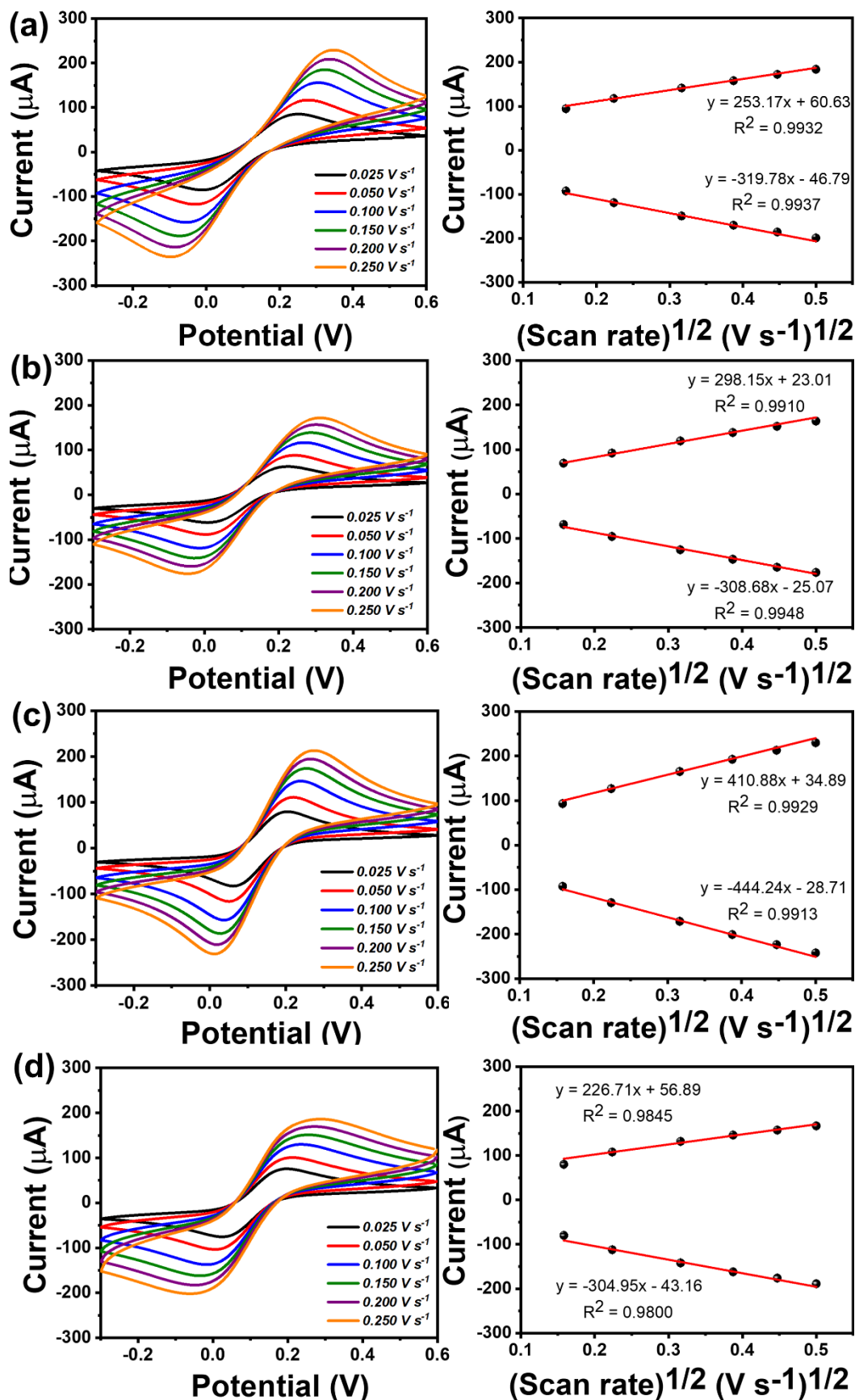


Figure S12. Cyclic voltammetry curves in a 1X PBS (pH 7.4) solution containing 5 mM $K_3[Fe(CN)_6]/K_4[Fe(CN)_6]$ measured at different scan rates (0.025-0.250 V/s) and peak currents vs square root of scan rates for bare (a) SPCE, (b) oxSPCE, (c) AuNSs/oxSPCE, and (d) Nafion/BSA/anti-CRP/AuNSs/oxSPCE nano-immunosensor.

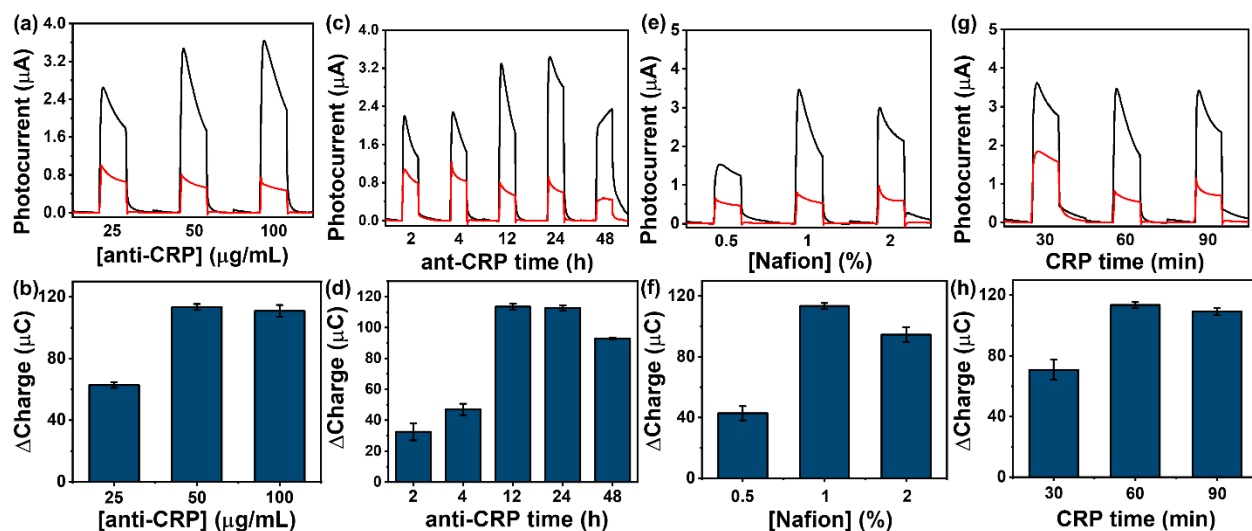


Figure S13. (a-b) The optimal concentration of anti-CRP antibodies on the AuNSs/oxSPCE interface with 0.8 ng/mL of CRP. (c-d) Comparison of the signal-time relationship across several interaction times on the AuNSs/oxSPCE incubated with 0.8 ng/mL of CRP. (e-f) Nafion resin concentration on the nano-immunosensor assembly. (g-h) Optimal nano-immunosensor and interaction time of 0.8 ng/mL of CRP on the nano-immunosensor for 30, 60, and 90 min. In graphs (a, c, e, and f), black is the nano-immunosensor, red is 0.8 ng/mL CRP, and in graphs (b, d, f, and h), $n=3$.

Table S3. (Photo)electrochemical biosensors for the detection of CRP.

Working electrode	Electrolyte / Redox probe	λ_{exc} (nm)	Technique	Detection time (min)	Linear range	LOD	Matrix	Ref
ITO/NiS/p-COF/Ag NPs	PBS 10X / H_2O_2	414	Chrono-amperometry	30	0.5 – 100 ng/mL	0.1 ng/mL	Human serum	[222]
GCE/PCN-777/DepAu	PBS 10X / H_2O_2	365	Chrono-amperometry	30	50 fM – 50 nM	16 fM	Synthetic serum	[223]
GCE/PTB7-Th/DepAu	PBS 10X / H_2O_2	365	Chrono-amperometry	30	1 pM – 1000 nM	0.33 pM	Human serum	[224]
GCE/TiO ₂ /PTCDA/depAu	PBS 10X / H_2O_2	365-370	Chrono-amperometry	120	10 pg/mL – 10 µg/mL	3.33 pg/mL	Synthetic serum	[225]
CMF/TiO ₂ /Au NCs/AuNPs	Tris-HCl / TEOA	425	Chrono-amperometry	60	1 pg/mL – 200 ng/mL	1 pg/mL	Human serum	[226]
CdS/TiO ₂ NTs	PBS 10X / AChE	410	Chrono-amperometry	60	50 ng/mL-50 µg/mL	50 ng/mL	Synthetic serum	[227]
GCE/PEI-Fc	PBS 1X / K_2SO_4	-	DPV	120	1 - 5·10 ⁴ ng/mL	0.5 ng/mL	Human blood	[228]

Au/MB	PBS 1X / [Ru(NH ₃) ₆] ³⁺	-	SWV	45	1-100 pM	1 pM	Human serum	[229]
AuNPs@BP@ PDA	PBS 1X / [Fe(CN) ₆] ^{3-/4-}	-	SWV	120	0-0.036 μg/mL	0.7 ng/mL	Human plasma	[230]
Luminex®	-	-	Fluorescence	240	0.3-100 μg/mL	0.05 μg/mL	-	[303]
oxSPCE/ AuNSs	PBS 1X / AA	765	Chrono- amperometry	60	0.025-0.8 ng/mL	13.3 pg/mL	Human serum	This work

AChE: acetylthiocholine, Ag: silver, ALP: alkaline phosphatase enzyme, BP: black phosphorus, CdS: cadmium sulfide, CMF: 3D carbon fiber matrix, DepAu: electrodeposited gold nanoparticles, DPV: differential pulse voltammetry, GCE: glassy carbon electrode, ITO: indium tin oxide, LOD: limit of detection, MB: methylene blue, NCs: nanocubes, NiS: nickel sulfide, NTs: nanotubes, p-COF: covalent organic frameworks, PCN-777: zirconium-based metal-organic framework, PDA: polydopamine, PEI-Fc: ferrocene-functionalized polyethylenimine, PTCDA: 3,4,9,10-perylene tetracarboxylic dianhydride, PTB7-Th: poly{4,8-bis[5-(2-ethylhexyl)thio-phen-2-yl]benzo[1,2-b:4,5-b']dithiophene-2,6-diyl-alt-3--fluoro-2-[(2-ethylhexyl)carbonyl] thieno[3,4-b]-thiophene-4,6-diyl}, Ru(NH₃)₆³⁺: ruthenium hexaamine, SWV: square-wave voltammetry, TEOA: triethanolamine, Th-T: thioflavin, TiO₂: titanium dioxide, and λ_{exc}: excitation wavelength.

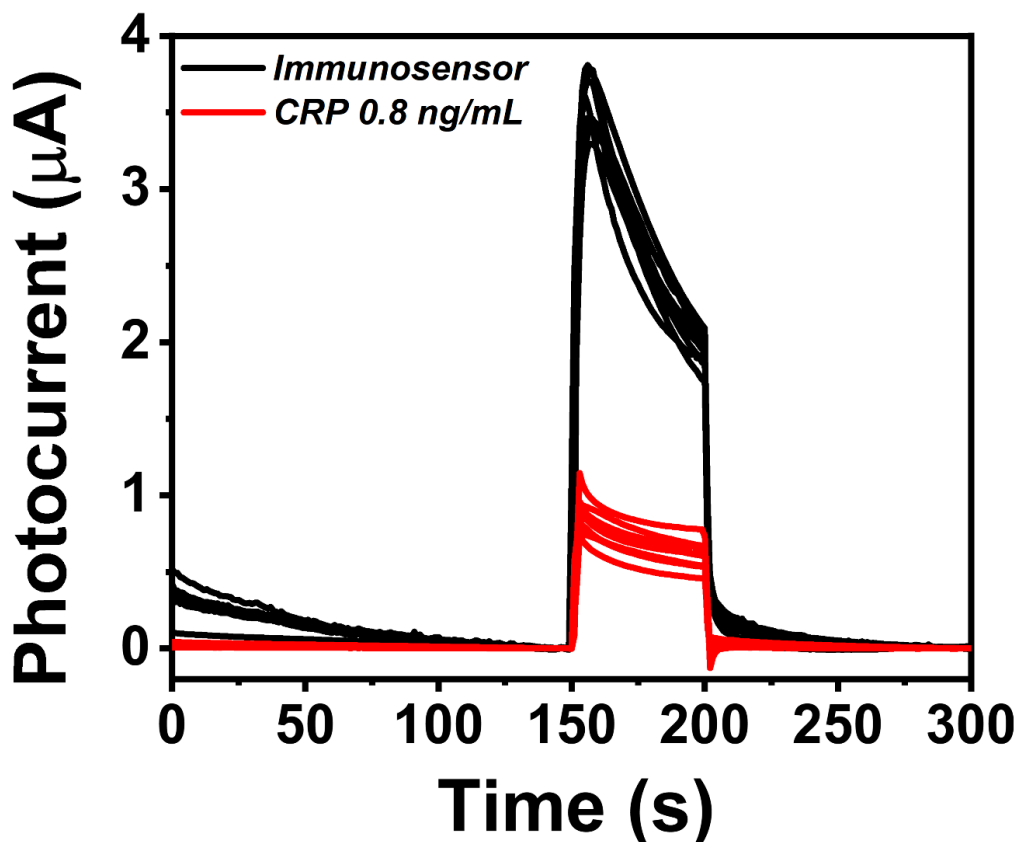


Figure S14. Detection reproducibility assay with ten different immunosensor assemblies.

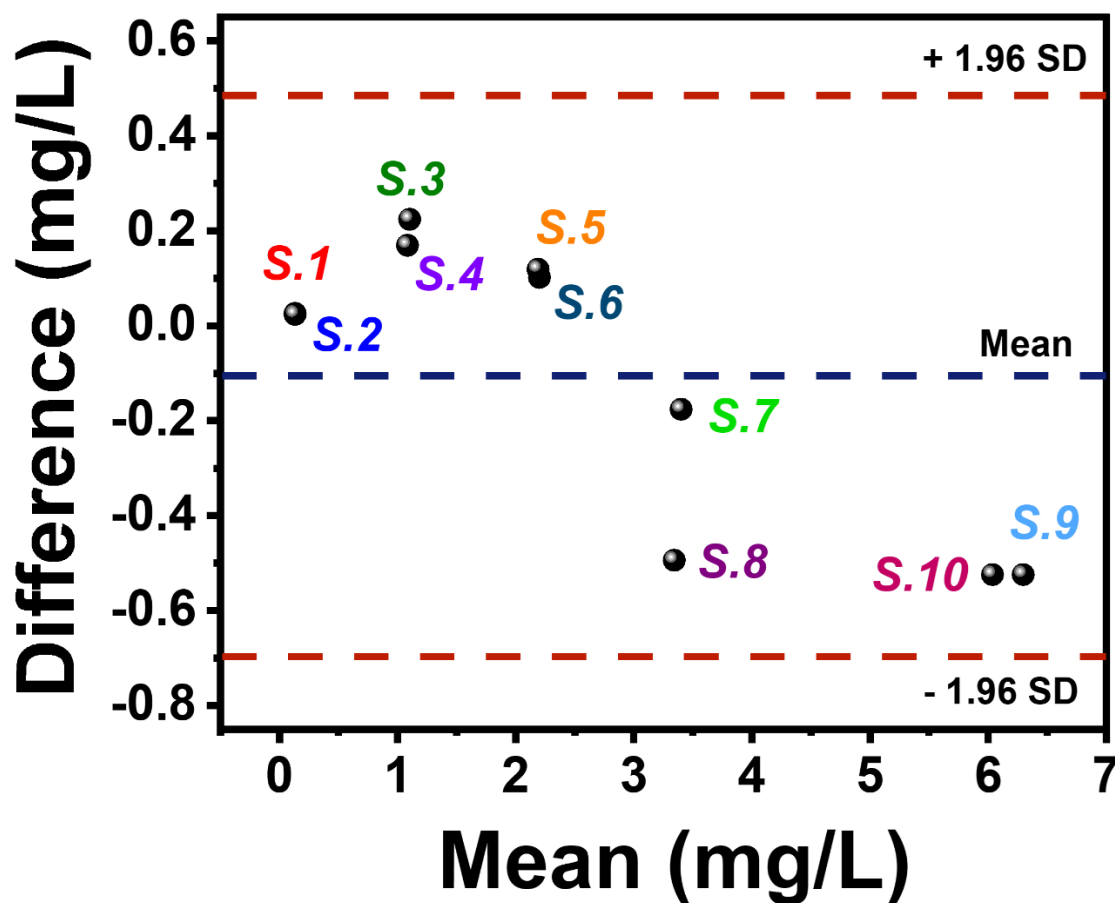


Figure S15. Bland-Altman plot between the results obtained from the PEC nano-immunosensor and standard Human Luminex® Discovery Assay for CRP detection in serum samples from patients with different levels of inflammation.

Table S4. Dilution factor used to detect CRP in the samples on the immunosensor and CRP quantification by the conventional Luminex method.

Sample	Dilution factor	Immunosensor (mg/L)	Luminex (mg/L)
S. 1	1:2000	0.15 ± 0.01	0.12
S. 2	1:2000	0.14 ± 0.03	0.12
S. 3	1:4000	1.21 ± 0.03	0.99
S. 4	1:4000	1.17 ± 0.01	1.00
S. 5	1:6000	2.25 ± 0.16	2.15
S. 6	1:6000	2.25 ± 0.07	2.13
S. 7	1:6000	3.31 ± 0.07	3.49

S. 8	1:6000	3.09 ± 0.18	3.59
S. 9	1:9000	6.04 ± 0.01	6.56
S. 10	1:9000	5.78 ± 0.14	6.3